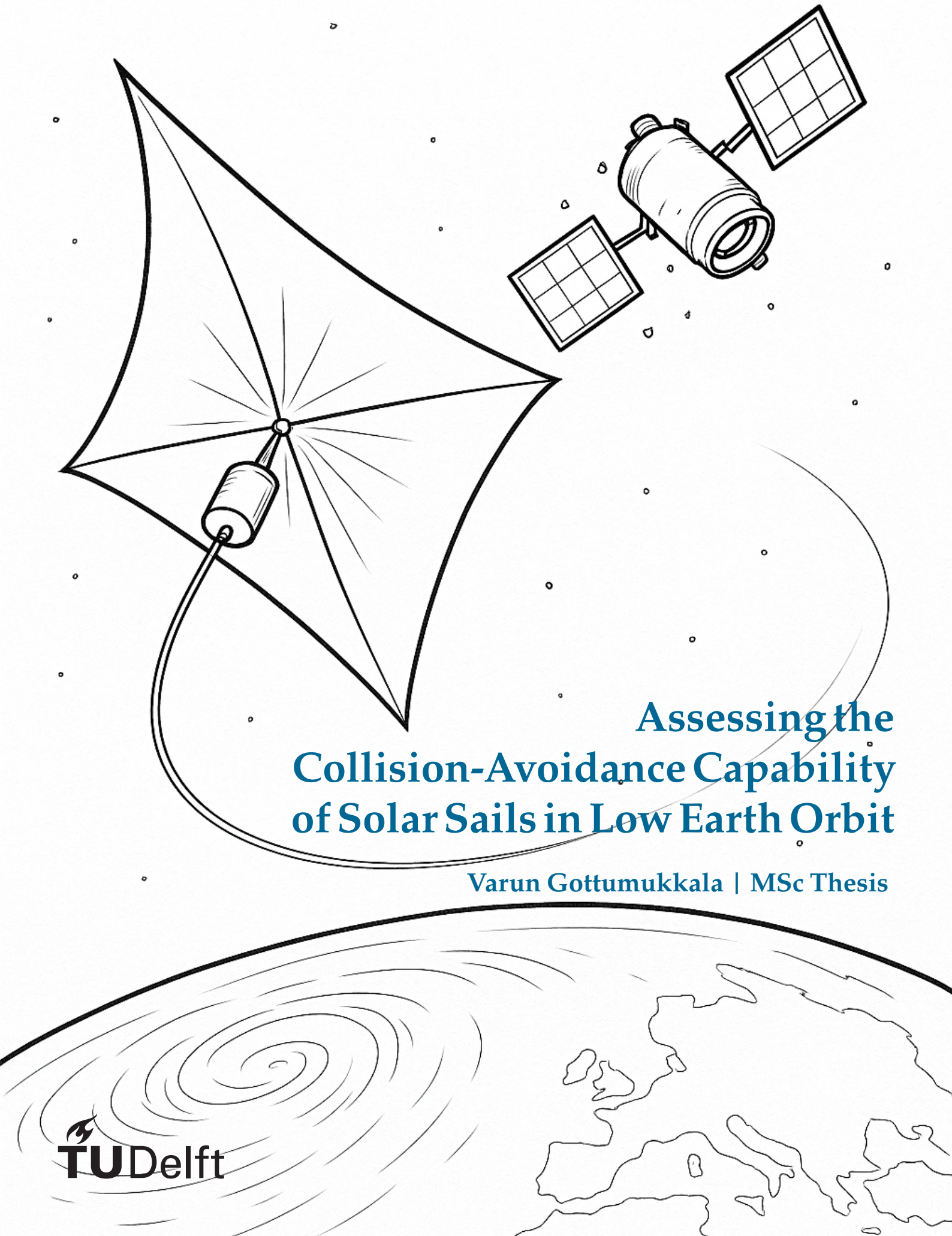

Assessing the Collision-Avoidance Capability of Solar Sails in Low Earth Orbit

Varun Gottumukkala | MSc Thesis

TUDelft

Assessing the Collision-Avoidance Capability of Solar Sails in Low Earth Orbit

by

Varun Gottumukkala

A thesis submitted to the Delft University of Technology in partial fulfilment of the requirements for the degree of Master of Science in Aerospace Engineering, to be defended publicly on October 17, 2025.

Student Number:	5263883	
Thesis Committee:	Dr. Ir. M.J. Heiligers	Responsible Supervisor
	Dr. S. Gehly	Supervisor
	Dr. Ir. E.J.O. Schrama	Chair
	Dr. S. Speretta	External Examiner
Thesis Duration:	February, 2025 - October, 2025	
Faculty:	Aerospace Engineering, TU Delft	

An electronic version of this thesis is available at http://repository.tudelft.nl/

Cover: OpenAI. (2025). *ChatGPT* (October 2025 version) [Large language model]
Style: TU Delft Report Style, with modifications by Daan Zwaneveld and Varun Gottumukkala

TU Delft

Preface

This thesis marks the culmination of five years of study in Delft, a journey that would not have been possible without the support of many people.

A special thanks to Jeannette and Steve for their guidance and always ensuring that I have thought things through. Your supervision has helped me approach problems in a more critical manner, and I am grateful for the freedom you gave me to explore and learn.

In my very first days in the Netherlands, I met people who are now some of my closest friends. To all the friends I have made along the way, you made the tough times bearable and the good times even better. And to the ones back home, you make every visit home worth it. Thank you all for the wonderful times and making the past five years fly by.

Finally, I would like to thank my sister and parents for their unwavering support — both financial and emotional — throughout this journey. Thank you for giving me the opportunity to move abroad at 18, for the freedom to live my own life, and for always reminding me that I had a home to return to. I feel extremely lucky to call the three of you my family.

Varun Gottumukkala
Delft, October 2025

Summary

Recent years have seen a rapid growth in the population of objects orbiting the Earth, leading to increasingly congested orbits. Over 36,500 objects larger than 10 cm are currently tracked, with estimates suggesting much larger numbers of untracked objects. This has led to a growing threat of collision between critical space assets and pieces of debris. The situation continues to worsen with mega-constellation deployments, evidenced by the European Space Agency's Space Debris Office issuing over 100,000 collision warnings in 2022 alone.

Conventional collision avoidance relies predominantly on propulsive maneuvers that consume finite propellant reserves, limiting the number of maneuvers possible throughout a mission lifetime. Recent advances in solar-sail technology have shown orbit-control capabilities around the Earth through Solar Radiation Pressure (SRP) alone, presenting a compelling propellant-free alternative. Proposed projects such as SWEEP (Space-waste Elimination around Earth by Photon Propulsion) aim to demonstrate the use of solar sails for active debris removal; for such missions, it is important to characterize the sail's collision-avoidance capability using only environmental forces. However, existing literature on novel collision-avoidance methods using SRP and atmospheric drag is limited to low area-to-mass ratio (LAMR) objects with maneuver durations on the order of days, and the most relevant work focused on higher orbits where SRP and the J_2 effect are the only considered perturbations, creating a knowledge gap in lower orbital regimes where atmospheric drag becomes dominant. Further, recent work has indicated the applicability of locally-optimal control laws for collision-avoidance of solar sails, which are analyzed in this work.

The research gap is addressed through the development of a simulation framework to assess the collision-avoidance capability of solar sails using locally optimal control laws driven by both SRP and atmospheric drag with a focus on altitudes between 400 and 800 km. The methodological approach involves developing a comprehensive dynamical model incorporating point-mass gravity, Earth's oblateness through the J_2 perturbation, SRP, and atmospheric drag using the high-fidelity NRLMSISE-00 empirical model. Locally optimal control laws are utilized to maximize the instantaneous rate of change of specific orbital elements. For SRP-dominant scenarios, known analytical control laws provide closed-form solutions, while for environments where drag is significant, a hierarchical grid-search optimization method is implemented that employs a two-phase approach with a coarse-grid evaluation followed by a fine-grid refinement.

Representative synthetic orbital state uncertainties are generated through a regression analysis of a dataset of Conjunction Data Messages. Collision risk assessment employs both the Foster method for collision probability calculation and the Mahalanobis distance metric to address dilution effects. The optimization problem is formulated to find minimum maneuver durations required to satisfy collision risk thresholds using a bisection optimization method.

The results reveal significant variability in optimal maneuver durations, ranging from as low as 5 minutes for high area-to-mass ratio sails at very low altitudes to over 6 hours for LAMR objects at high altitudes. The maneuver durations at very low altitudes are substantially lower than those found in previous work which focused on altitudes above 1000 km, primarily due to the exponential increase in atmospheric density at lower altitudes enabling the use of a_{min} (semi-major axis minimization) control laws that quickly lower the sail's altitude using face-on orientations relative to the velocity vector.

The parametric analysis reveals distinct trends across different parameters. Higher sail area-to-mass ratio values consistently lead to shorter maneuver durations and largely utilize a_{min} control at altitudes below approximately 525 km, switching to a_{max} (semi-major axis maximization) at higher altitudes when SRP becomes relatively significant. The aspect angle, which is the angle between the orbit's angular momentum vector and sunlight direction, shows a strong correlation with control law usage, with SMA (Semi-major Axis) control laws being utilized more frequently for large aspect angles and RAAN (Right Ascension of Ascending Node) control laws being more effective at small aspect angles. An interesting phenomenon is observed where maneuver durations exhibit discrete jumps corresponding to eclipse periods.

Conjunction separations at the time of closest approach (TCA) cause significant decreases in maneuver duration for separations directed along the normal direction for high aspect angles; such separations of 40 meters lead to decreases in maneuver durations of over an hour in comparison with the zero miss-distance case, with the Ω_{max} (RAAN-maximization) control law becoming most effective. At an aspect angle of zero degrees, for normal separations directed towards the Sun, Ω_{min} (RAAN-minimization) is ineffective due to the lack of coincidence between its optimal thrusting direction and the SRP acceleration envelope, leading to the usage of a_{max} and a_{min} control laws for positive and negative tangential separations, respectively.

The results indicate that while solar sails can perform effective collision avoidance maneuvers in specific orbital regimes with maneuver durations significantly shorter than previous estimates, careful consideration of environmental, physical, and orbital parameters is essential for practical implementation. The effect of atmospheric drag is significant and displays clear trends across different altitudes, aspect angles, and physical parameters, but practical viability is constrained to altitudes above 500 km during average solar weather conditions, with the sensitivity of performance necessitating consideration of solar cycle effects on maneuver duration.

Contents

List of Figures

List of Tables

Nomenclature

Acronyms

Acronym	Definition
ACS3	Advanced Composite Solar Sail System 3
ADCS	Attitude Determination and Control System
ADR	Active Debris Removal
AMR	Area-to-Mass Ratio
AU	Astronomical Unit
CAM	Collision Avoidance Maneuver
CCSDS	Consultative Committee for Space Data Systems
CDM	Conjunction Data Message
CRASS	Collision Risk Assessment Software
ECI	Earth-Centered Inertial
ESA	European Space Agency
GSOC	German Space Operations Center
HAMR	High Area-to-Mass Ratio
HBR	Hard-Body Radius
LAMR	Low Area-to-Mass Ratio
LEO	Low Earth Orbit
LOCL	Locally Optimal Control Law
NASA	National Aeronautics and Space Administration
NRLMSISE-00	Naval Research Laboratory Mass Spectrometer and Incoherent Scatter Radar Extended Model
RAAN	Right Ascension of Ascending Node
RMS(E)	Root Mean Square (Error)
RTN	Radial-Tangential-Normal
S/C	Spacecraft
SFU	Solar Flux Unit
SMA	Semi-Major Axis
SPICE	Spacecraft, Planet, Instrument, C-matrix, Events
SRP	Solar Radiation Pressure
SSO	Sun-Synchronous Orbit
SWEEP	Space-waste Elimination around Earth by Photon Propulsion
TCA	Time of Closest Approach

Roman Symbols

Symbol	Definition	Unit
a	Semi-major axis	km
$\boldsymbol{a}$	Acceleration	m/s^2
$a_{max/min}$	Semi-major axis maximization/minimization control law	-
a_C	Characteristic acceleration	mm/s^2
a_j	Uncertainty curve-fitting coefficient (constant term)	m
A	Area	m^2
A_p	Geomagnetic index	nT
AU	Astronomical Unit	m
b_j	Uncertainty curve-fitting coefficient (linear term)	m/s
c	Speed of light	m/s
c_j	Uncertainty curve-fitting coefficient (quadratic term)	m/s^2
$\boldsymbol{C}$	Covariance matrix	various
C_D	Drag coefficient	-
C_r	Reflectivity coefficient	-
d_M	Mahalanobis distance	-
e	Eccentricity	-
E	Eccentric anomaly	deg
F	Force	N
$F_{10.7}$	Solar flux index	SFU
$F_{10.7A}$	81-day average solar flux	SFU
$\boldsymbol{h}$	Specific angular momentum	m^2/s
h_{alt}	Altitude	km
h_p	Perigee altitude	km
H	Scale height	km
i	Inclination	deg
J_2	J_2 coefficient	-
m	Mass	kg
$\boldsymbol{n}$	Sail normal vector	-
N	Normal direction	-
N_α	Cone angle grid indices	-
N_δ	Clock angle grid indices	-
p	Semi-latus rectum	km
P_0	Solar flux constant	W/m^2
P_c	Collision probability	-
$\boldsymbol{q}$	Relative displacement vector	m

Symbol	Definition	Unit
$\boldsymbol{r}$	Position vector in ECI frame	km
$\boldsymbol{r}_c$	Position vector in the encounter plane	m
R	Radial direction	-
R_{combined}	Combined hard-body radius	m
R_{Earth}	Earth's equatorial radius	m
R_{force}	Relative force magnitude ratio	-
R_{Sun}	Sun's radius	m
s	Object size	m^2
t	Time	s
t_{man}	Maneuver duration	s
T	Tangential direction	-
u	Argument of latitude	deg
$\boldsymbol{v}$	Velocity	km/s
x, y, z	Cartesian coordinates	km

Greek Symbols

Symbol	Definition	Unit
α	Cone angle	rad
α_λ	Primer vector cone angle	rad
β	Aspect angle	deg
γ	Vernal equinox direction	-
δ	Clock angle	rad
$\boldsymbol{\delta}_c$	Miss vector in the encounter plane	-
δ_λ	Primer vector clock angle	rad
Δ	Change in quantity	various
ϵ	Tolerance	-
θ	True anomaly	deg
θ_{lat}	Geographic latitude	deg
θ_{lon}	Geographic longitude	deg
θ_s	Angle between incident light and sail normal	deg
θ_{sep}	Angular separation	deg
$\boldsymbol{\lambda}$	Primer vector	-
$\boldsymbol{\lambda}_{a_{max/min}}$	Primer vector for sami-major axis maximization/minimization control law	-
$\boldsymbol{\lambda}_{\Omega_{max/min}}$	Primer vector for Right Ascension of Ascending Node maximization/minimization control law	-
μ	Gravitational parameter	m^3/s^2
ν	Shadow factor	-

Symbol	Definition	Unit
ρ	Atmospheric density	kg/m^3
σ	Position uncertainty (1-sigma)	kg/m^2
σ_s	Sail loading parameter	m
ω	Argument of perigee	deg
Ω	Right Ascension of Ascending Node	deg
$\Omega_{max/min}$	Right Ascension of Ascending Node maximization/minimization control law	-

Superscripts and Subscripts

Notation	Definition
Superscripts	
*	Coarse optimal value
**	Refined optimal value
^{T}	Matrix transpose
^{thresh}	Threshold value
Subscripts	
$_{\text{Earth}}$	Earth related
$_{\text{Sun}}$	Sun related
$_{\text{SRP}}$	Solar Radiation Pressure related
$_{\text{drag}}$	Atmospheric drag related
$_{\text{gravity}}$	Gravitational force related
$_{J_2}$	J_2 perturbation related
$_{\text{max}}$	Maximization control law
$_{\text{min}}$	Minimization control law
$_{R,T,N}$	Radial, Tangential, Normal components
$_{x,y,z}$	Cartesian coordinate components

Physical Constants

Constant	Value
AU	$1.49597870700 \times 10^{11}$ m
c	2.99792458×10^{8} m/s
J_2	$1.08262668 \times 10^{-3}$
μ_{Earth}	$3.986004418 \times 10^{14}$ m^3/s^2
P_0	1361 W/m^2
R_{Earth}	6.378137×10^{6} m
R_{Sun}	6.957×10^{8} m

1 Introduction

Space activities over the last two decades have transformed Earth's orbital environment into an increasingly congested region. Over 36,500 tracked objects larger than 10 cm currently orbit the Earth, with estimates of more than 1 million debris objects larger than 1 cm, leading to increased risks of collision, particularly in Low Earth Orbit (LEO) (ESA, 2024). While satellites at low enough altitudes naturally decay due to atmospheric drag within a few years, satellites in higher orbits without propulsive capabilities at the end of their mission can remain in orbit for decades, effectively becoming uncontrolled pieces of metal hurtling around the Earth. Collision-avoidance capabilities help mitigate the risk of collisions but do not address the growing population of space debris. This has given rise to Active Debris Removal (ADR) solutions that aim to use satellites, typically with robotic arms, to maneuver towards a piece of debris and assist in de-orbiting it. However, ADR missions require significant amounts of propellant to rendezvous with debris objects and transfer a sufficient impulse for de-orbiting.

Recent years have seen an increase in solar-sail applications in LEO, with missions demonstrating deployment and orbit-raising capabilities through the sole utilization of Solar Radiation Pressure (SRP) (Ancona & Kezerashvili, 2024). Solar sails present a compelling solution for ADR, as they can use the continuous solar radiation from the Sun to maneuver towards debris. However, such a mission would also be subject to collision risks during its rendezvous in potentially highly congested regions, particularly given a sail's large surface area. It is therefore important to assess the capability of solar sails to avoid such collisions in LEO. While research in this domain is very limited, recent work suggests that appropriate control laws can be utilized by solar sails to achieve effective collision-avoidance maneuvers (Ambrosio, 2025). However, this application for solar sails has not yet been explored in LEO regimes where atmospheric drag has a considerable effect on the sail's trajectory. This research develops and evaluates a simulation framework for assessing the collision-avoidance capability of solar sails using locally optimal control laws driven by SRP and atmospheric drag.

Chapter 2 reviews literature on space debris, solar-sailing fundamentals and collision-avoidance methods, leading to the identification of a research gap and the formulation of research questions, which are presented in Chapter 3. The methodologies used to develop the capabilities to address the research questions are presented in Chapter 4, including the development of a dynamical model, implementation of locally optimal control laws, synthetic uncertainty generation, collision-avoidance scenario definition, and maneuver optimization. Chapter 5 discusses simulation results, examining the effectiveness of the utilized control laws and the optimal maneuver durations through a parametric analysis. Finally, Chapter 6 summarizes the findings in context of the research objective and suggests future research directions.

2 Literature Review

This section outlines the status quo of research on solar-sailing technology, collision-avoidance methods and nature-driven collision avoidance. First, Section 2.1 discusses the threat of collisions caused by a growing population of space debris in Earth's orbit. Section 2.2 introduces the theory of solar sailing and its practical applications, including past missions. Section 2.3 outlines conventional debris mitigation methods and their limitations, and then introduces the concept of nature-driven collision avoidance and its potential benefits for sustainable space operations.

2.1. The Space Debris Problem

This section introduces the growing threat posed by space debris and discusses the collision probability metric as a method of quantifying the threat.

A Growing Threat

For decades, the space industry was dominated by the "big sky theory" – the belief that Earth's orbital capacity was so vast that the risk of collision was negligible, which eliminated the perceived need for risk assessment and mitigation strategies (Newman et al., 2009). However, the rapid expansion of space activities in recent years has resulted in a complex and increasingly hazardous orbital environment, indicating a shift away from the "big sky theory". Currently, over 36,500 objects larger than 10 cm are tracked, with estimates suggesting more than 1 million debris objects larger than 1 cm and hundreds of millions of smaller, untracked particles (ESA, 2024). These objects pose significant threats due to their high relative velocities, which can exceed 15 km/s in LEO (Braun et al., 2016; Matney et al., 2004). The destructive potential of such impacts is exemplified by damage observed on returned spacecraft surfaces, including craters on Space Shuttle windows and penetrations in solar panels (Klinkrad et al., 2006).

The severity of this problem was shown by the 2009 collision between Cosmos 2251 and Iridium 33, which generated over 1,800 trackable fragments and countless smaller pieces (Shan et al., 2016). Such events, along with anti-satellite tests, can create thousands of trackable fragments, substantially exacerbating the already precarious debris environment (Klinkrad et al., 2006). These incidents emphasize the potential for a collisional cascade as predicted by Donald Kessler in 1978, commonly called the *Kessler Syndrome*, wherein debris generation through collisions outpaces natural removal mechanisms, potentially rendering certain orbital regions unusable (Colombo et al., 2023).

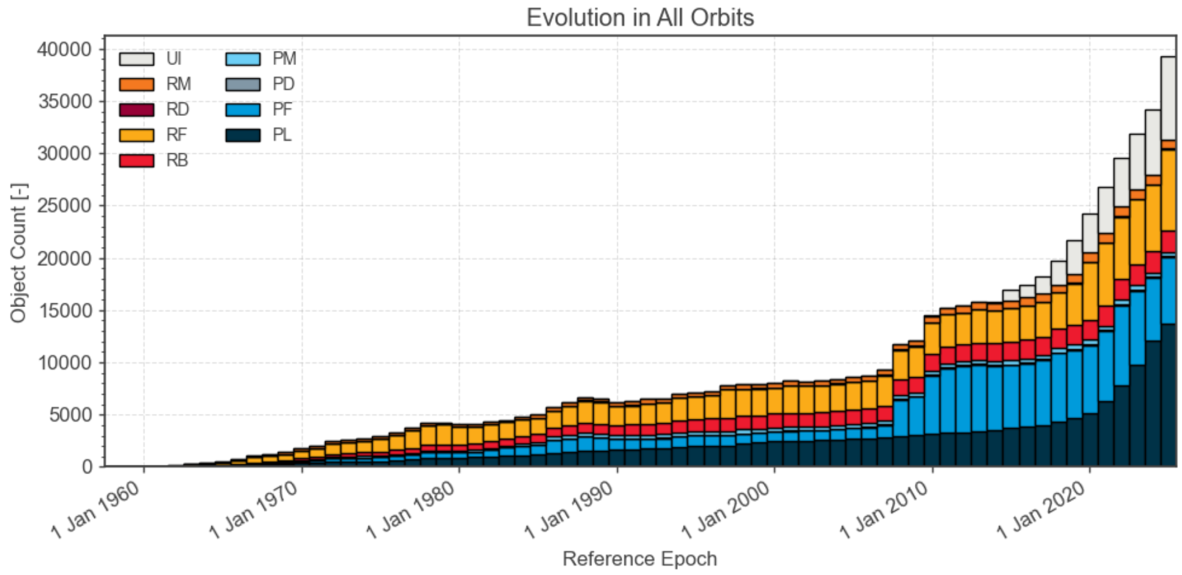

Figure 2.1: Growth in the number of objects in orbit over time (ESA, 2024).

The situation continues to worsen with the deployment of mega-constellations comprising thousands of satellites in LEO, with companies such as SpaceX and OneWeb planning global broadband internet constellations in the coming decades (Le May et al., 2018). These developments have dramatically increased conjunction rates and corresponding collision risks, as evidenced by the growing number of conjunction warnings issued to satellite operators. In 2022 alone, the European Space Agency's (ESA) Space Debris Office issued over 100,000 collision warnings for satellites, representing a significant increase from previous years (ESA, 2024). The rapid growth in orbital objects can be seen in Figure 2.1, which highlights the exponential growth across different object types, such as payloads (PL) and rocket fairings (RF). Figure 2.2 further highlights the distribution of these objects across different altitudes; the highest density of objects larger than 1 cm in size is concentrated between altitudes of approximately 500 and 1000 km, with active payloads mostly lying between altitudes of 400 and 600 km. This provides an indication towards the regions in LEO that are most at risk of collisions.

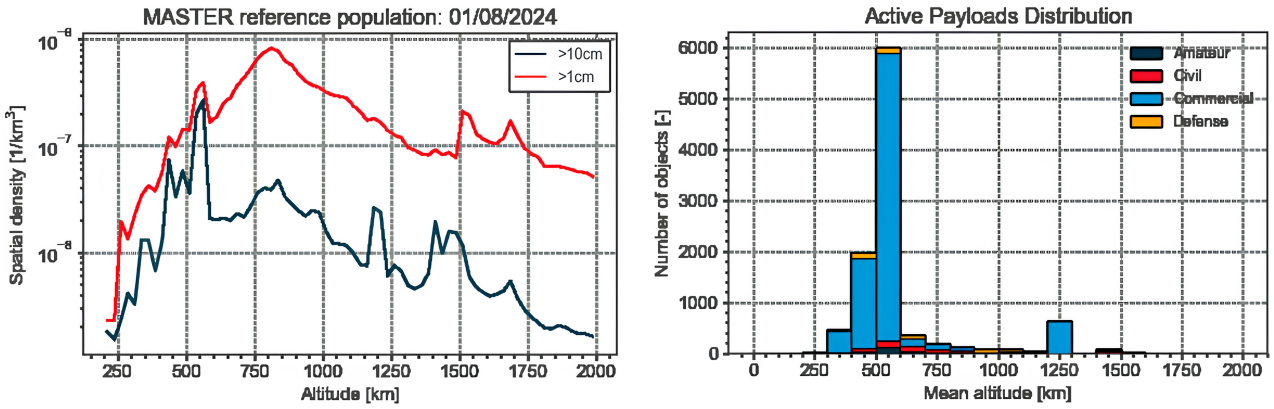

Figure 2.2: Distribution of debris flux and active payloads across altitudes (ESA, 2024).

To address these risks, space agencies have developed systems for predicting potential collisions and issuing conjunction warnings to satellite operators. ESA, for example, has developed the Collision Risk Assessment Software (CRASS), which processes conjunction data messages (CDMs), performs risk analyses, and provides decision support for collision-avoidance maneuvers (Braun et al., 2016). Such services rely on tracking data from organizations such as the U.S. Space Force's 18th Space Defense Squadron, which issues warnings to satellite operators worldwide through its network of ground-based radar and optical sensors (Merz et al., 2017).

Probability of Collision

The fundamental metric for evaluating collision risk is the probability of collision (P_c), which is traditionally calculated using analytical or numerical techniques that integrate the relative position probability density over the combined hard-body radius (HBR) of the objects involved. The foundational approach developed by Foster (2001) approximates the position uncertainty as a three-dimensional Gaussian distribution and reduces the three-dimensional problem to a two-dimensional integration in the encounter plane — a plane perpendicular to the relative velocity vector at the time of closest approach (TCA). This approach assumes that the relative motion is linear near the conjunction and that the encounter duration is short enough that the covariance does not change significantly. Such a linear conjunction scenario is illustrated in Figure 2.3. For cases where these assumptions are valid, the probability of collision can be calculated as:

$$P_c = \frac{1}{2\pi\sqrt{|\mathbf{C}|}} \int_{HBR} \exp\left(-\frac{1}{2}\mathbf{r}_c^T \mathbf{C}^{-1} \mathbf{r}_c\right) d\mathbf{r} \tag{2.1}$$

where $\mathbf{C}$ is the combined covariance matrix (explained in the following paragraph) in the encounter plane, $\mathbf{r}_c$ is the position vector in the encounter plane, and the integration is performed over a circle with radius equal to the combined HBR of the two objects (Alfriend et al., 1999; Patera & Peterson, 2003).

The covariance matrix is of critical importance in collision probability assessment, as it represents the uncertainty in the position estimates of both objects. This uncertainty stems from several sources, including tracking measurement errors, force model approximations, and prediction uncertainties that grow with time from the last observation (Alfano & Oltrogge, 2018). The size, shape, and orientation of this covariance ellipsoid directly influence the calculated collision probability, with smaller uncertainties generally leading to more deterministic collision probability values (Zollo et al., 2024). For more complex scenarios where linear assumptions break down, such as long-duration encounters or highly eccentric orbits, more sophisticated approaches are required. Recent research has explored Monte Carlo simulations, polynomial chaos expansions, and machine learning approaches for risk assessment in complex scenarios (Liu et al., 2023).

The collision probability density per unit area is characterized by the function $h(\mathbf{x})$ as shown in Figure 2.4, with its spatial distribution illustrated through constant contour lines. For analytical convenience and visualization purposes, all uncertainty in the relative position between the two objects is attributed to the first object, which is positioned nominally at the coordinate origin. This

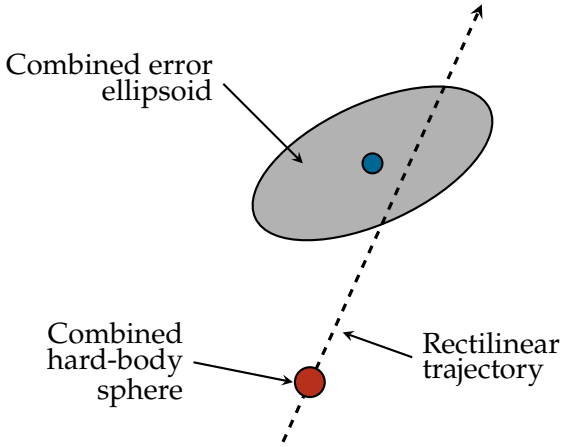

Figure 2.3: Linear short-term encounters, with the combined hard-body circle and combined error ellipsoid (adapted from Patera (2003)).

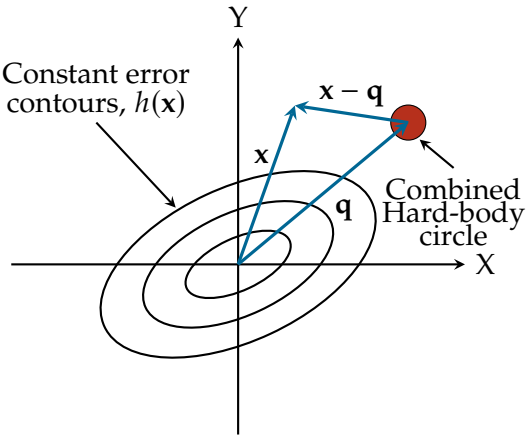

Figure 2.4: Collision probability density and relative position of the hard-body circle in the encounter plane (adapted from Patera (2000)).

approach simplifies the mathematical framework while maintaining computational accuracy for risk assessment applications.

The second object's position is determined by the relative displacement vector $\mathbf{q}$, which represents the transformed relative position vector at the TCA within the encounter reference frame. This transformation eliminates positional uncertainty in $\mathbf{q}$ since all relative position uncertainty has been systematically assigned to the first object. The hard-body circle, representing the combined physical extent of both objects, is centered on the second object at position $\mathbf{q}$.

For a collision event to occur, the actual position of the first object must fall within the boundaries of the hard-body circle. Consequently, the total collision probability is determined through integration of the probability density function over the hard-body circular region.

When the calculated collision probability exceeds a predetermined threshold (typically in the range of 10^{-4} to 10^{-5} for high-value assets), operators must decide whether to perform a collision-avoidance maneuver (Sánchez-Ortiz et al., 2006). These maneuvers typically involve propulsive burns designed to increase the miss distance at the TCA, with the optimal direction generally perpendicular to the relative velocity vector to maximize separation for minimal fuel expenditure (Patera & Peterson, 2003). However, each such maneuver consumes limited propellant resources, potentially reducing the operational lifetime of the spacecraft and imposing operational constraints such as service interruptions and attitude adjustments (Kim et al., 2012).

A study by Sánchez-Ortiz et al. (Sánchez-Ortiz et al., 2006) projected that a typical high-value LEO satellite might need to perform between one and five collision-avoidance maneuvers annually, a figure that has likely increased with the growing orbital population. For constellations comprising hundreds or thousands of satellites, this translates to a substantial operational burden and significant propellant consumption across the fleet (Le May et al., 2018). Furthermore, the growing number of warnings may lead to "warning fatigue," potentially causing high-risk conjunctions to be overlooked amid numerous lower-risk alerts (Alfano & Oltrogge, 2018).

2.2. Solar-Sailing Fundamentals and Technologies

This section introduces the fundamentals of solar sailing and outlines the status quo of solar-sail technologies, missions and applications, including a discussion of SRP-driven control methods.

Fundamentals of Solar Sailing

Solar sailing is a propellant-less propulsion method that harnesses SRP to generate thrust. This technology utilizes the momentum transfer from solar photons to a reflective surface, producing continuous force without propellant expenditure — a significant advantage compared to conventional propulsion systems (Gong & Macdonald, 2019; McInnes, 2004). The scientific foundations of solar sailing date back to the early 20th century, when SRP was first theoretically described based on Maxwell's electromagnetic theory and Einstein's photon hypothesis (McInnes, 2004). However, the first systematic studies of SRP effects on spacecraft orbits were conducted in the 1960s, when researchers such as Parkinson et al. (Parkinson et al., 1960) and Levin (Levin, 1968) quantified the perturbations induced by solar radiation on early satellites.

An ideal solar-sail model assumes the sail to be a flat and rigid surface that is perfectly reflective (Kelly & Bevilacqua, 2020). The fundamental physics of an ideal sail involves the specular reflection of photons (Swartzlander, 2022). When a photon is absorbed by a surface, it transfers its momentum to the material, generating a force in the direction of the incident light. When specularly reflected, the photon transfers the same momentum opposite to the direction of reflection, with the resultant force component thus normal to the reflecting surface. The resulting radiation pressure on a perfectly reflecting surface at 1 Astronomical Unit (AU) is approximately 9.12×10^{-6} N/m^2 (Fu et al., 2016).

For an ideal solar sail with 100% specular reflection at 1 AU, the acceleration can be expressed as:

$$\mathbf{a}_{SRP} = \frac{2P_0}{c\sigma_s} cos^2(\alpha)\mathbf{n} \tag{2.2}$$

where $P_0 = 1361\,W/m^2$ represents the solar flux at 1 AU, $c = 299792458 m/s$, represents the speed of light, σ_s is the solar-sail loading parameter defined as the ratio of the sail's total mass to surface area, $\mathbf{n}$ is the sail's normal direction, and α is the angle between the sail's normal and direction of sunlight (Carzana et al., 2022; McInnes, 2004). This equation highlights the dependence of the sail's acceleration on its attitude relative to the direction of sunlight and the importance of maximizing the area-to-mass ratio (AMR) to achieve practical accelerations. The term $2P_0/c\sigma_s$ is defined as the characteristic acceleration, a_C.

Real solar sails deviate from this ideal behavior due to non-perfect reflectivity, thermal emission, wrinkles, and other material imperfections. Diffuse reflection results in a distributed force magnitude and direction, due to scattered reflections caused by surface imperfections. More sophisticated models account for these non-ideal characteristics through optical coefficients that describe the fraction of incident light absorbed, specularly reflected, and diffusely reflected (Spencer & Carroll, 2014). These coefficients depend on material properties, surface finishing, and wavelength, necessitating detailed characterization for accurate force prediction. Further, an efficiency factor is typically used

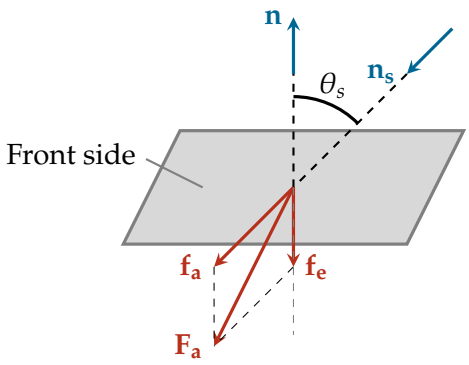

Figure 2.5: Force components on a solar sail surface showing absorbed force $\mathbf{f_a}$, emitted force $\mathbf{f_e}$, and resultant force $\mathbf{F_a}$. (adapted from Fu et al. (2016))

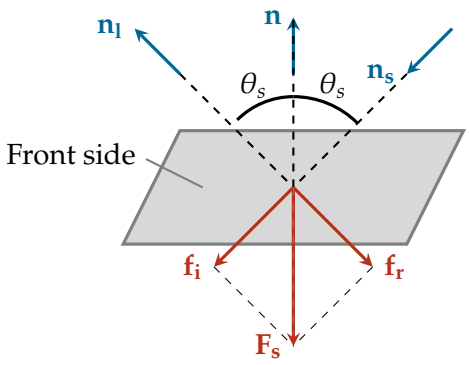

Figure 2.6: Force components on a solar sail surface showing specular reflection, with incident force $\mathbf{f_i}$, reflected force $\mathbf{f_r}$ and resultant force $\mathbf{F_s}$ (adapted from Fu et al. (2016))

to characterize the finite reflectivity of real solar sails, which is typically a value of approximately 0.9 (McInnes, 2004). For the optical sail model and sails with complex geometries, detailed numerical models accounting for shadowing, multiple reflections, and thermal re-emission are necessary for accurate force prediction (Yoshimura et al., 2023). Figures 2.5 and 2.6 provide schematics of the forces caused by absorption/emission and specular reflection, respectively.

Solar-Sailing Technologies

Recent decades have witnessed substantial advances in solar-sail materials and designs. Modern solar sails typically utilize metallized polymers such as aluminized Kapton or Mylar, with thicknesses as small as 2 μm (Fu et al., 2016; Spencer et al., 2019). These materials offer an optimal balance between reflectivity, durability, and mass efficiency, although they remain vulnerable to degradation from atomic oxygen, micrometeoroid impacts, and radiation exposure (Zhau et al., 2023). Emerging technologies include carbon fiber reinforcements to enhance structural integrity, multi-functional sail materials with embedded sensors or electronics, and novel concepts such as diffractive solar sails that manipulate light through diffraction gratings rather than simple reflection (Chu & Gong, 2024; Swartzlander, 2022).

The deployment of large, gossamer structures in space presents additional engineering challenges. Current solar-sail designs employ various folding patterns and deployment mechanisms, including the widely used four-quadrant design with diagonal booms that unfurl the sail from a compact configuration (Fu et al., 2016). Alternative approaches include spinning deployment, where centrifugal forces unfold the sail, and inflatable structures that provide initial rigidity before being jettisoned (Fu et al., 2016). Each approach offers different trade-offs regarding reliability, packed volume, mass efficiency, and final sail flatness. Schematics of the sail geometries that are of practical interest are shown in Figure 2.7.

Several missions have successfully demonstrated solar sailing in space, validating theoretical predictions and verifying deployment mechanisms. The Japanese IKAROS mission, launched in 2010, achieved the first controlled solar-sail flight using a 14-meter square sail with liquid crystal panels for attitude control (Fu et al., 2016; Zhau et al., 2023). NASA's NanoSail-D2 (2010) and The Planetary Society's LightSail-1 (2015) and LightSail-2 (2019) missions demonstrated sail deployment in Earth

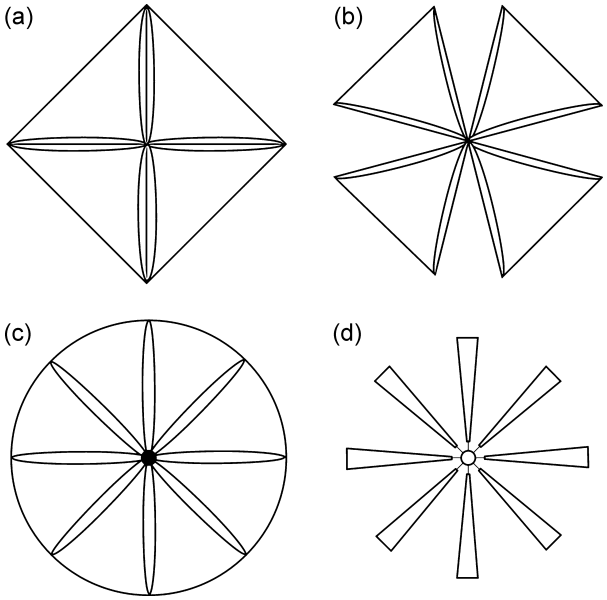

Figure 2.7: Solar sail geometries of practical interest: (a) square sail; (b) quad sail; (c) disk sail; and (d) heliogyro (Spencer et al., 2019).

orbit, with LightSail-2 notably achieving measurable orbit raising through solar sailing (Meireles et al., 2022; Zhau et al., 2023). Recent missions include NASA's Advanced Composite Solar Sail System (ACS3) mission, launched in 2024, which is currently in orbit around the Earth with a successfully deployed sail (Dono et al., 2025).

Of the past solar sails that have been launched, the ones that successfully demonstrated deployment and/or propulsive capabilities are summarized in Table 2.1. The table includes the sail area, mass, AMR, and characteristic acceleration (a_C) for each mission.

Table 2.1: Key parameters of successful solar sail missions (Ancona and Kezerashvili (2024), Biddy and Svitek (2012), Johnson et al. (2011), Spencer et al. (2021), Tsuda et al. (2011, 2013), Wilkie (2021), and Zhau et al. (2023)).

Year	Mission	Sail area [m^2]	Mass [kg]	AMR [m^2/kg]	a_C [mm/s^2]
2010	IKAROS	196	307	0.63	0.0059
2011	NanoSail-D2	10	4	2.5	0.0178
2015	LightSail-1	32	5	6.4	0.0652
2019	LightSail-2	32	5	6.4	0.0652
2024	ACS3	80	16	5	0.0454

SRP-driven Control Applications

SRP has been demonstrated as an effective mechanism for spacecraft control in various contexts beyond traditional solar-sailing missions. Research in formation flying has established that differential SRP can maintain relative positions between spacecraft without propellant consumption (Thoemel & van Dam, 2021; Williams & Wang, 2002). Williams and Wang (Williams & Wang, 2002) developed analytical models showing that differential reflectivity or area exposure could generate sufficient relative acceleration for formation maintenance in various orbit regimes. These concepts were further refined by Thoemel and van Dam (Thoemel & van Dam, 2021), who demonstrated autonomous formation control using SRP with minimal propellant expenditure. Similar principles have been

applied to satellite constellations by Kumar et al. (Kumar et al., 2014), who investigated using environmental forces, including SRP, to reduce station-keeping costs for distributed satellite systems.

Beyond formation control, SRP has been utilized for orbital corrections and end-of-life disposal. Silva Neto et al. (Silva Neto et al., 2017) analyzed the feasibility of using controlled radiation pressure to transfer satellites to graveyard orbits after mission completion, offering a potential solution for spacecraft with depleted propellant reserves. Research by Burnett and Schaub (Burnett & Schaub, 2021) demonstrated that differential attitude control could harness SRP for significant orbital adjustments over extended timeframes without propellant consumption.

The LightForce concept, developed by Yang Yang et al. (Yang Yang et al., 2016), proposed a ground-based laser system to augment natural SRP for debris collision avoidance. Their analysis indicated that even modest photon pressure could significantly reduce collision probability when applied days or weeks before conjunction, highlighting the potential effectiveness of radiation pressure approaches with sufficient lead time. While their implementation focused on ground-based lasers, the underlying physics and effectiveness metrics remain applicable to spacecraft-based SRP methods.

The control and attitude dynamics of solar sails present unique challenges compared to conventional spacecraft. The large, flexible structure creates complex dynamic behavior, including potential coupling between structural vibrations and attitude motion (Chujo, 2022; Wie, 2004). The primary control challenge arises from the need to precisely orient the sail relative to the Sun to generate the desired force vector, while also accommodating constraints such as power generation requirements and thermal limitations (Chujo et al., 2024; Wie & Murphy, 2007).

In Earth orbit, solar sailing introduces additional complexities due to the competition between SRP and other perturbations, particularly atmospheric drag in lower orbits. At altitudes below approximately 800 km, atmospheric drag typically dominates SRP effects, limiting the effectiveness of conventional solar sailing (Fieseler, 1998; Stolbunov et al., 2013). However, research has demonstrated that appropriate control strategies can exploit the complementary nature of these forces by orienting the sail such that SRP and drag are utilized in combination to achieve deviations in orbit (Carzana et al., 2022).

Analytical control laws offer closed-form solutions that enable efficient implementation under specific assumptions. For solar-sailing applications, these laws establish a mathematical relationship between the desired orbital evolution and the required sail attitude, typically expressed as a function of orbital elements and the Sun-spacecraft-Earth geometry (Macdonald & McInnes, 2005; Niccolai et al., 2017). The implementation of such control laws presents unique challenges in the LEO environment, where both SRP and atmospheric drag must be considered simultaneously. In this regime, locally optimal control laws (LOCLs) have been developed that enable effective orbit modification even in drag-dominant conditions (Carzana et al., 2022). These laws typically decompose the control problem into the selection of an orbital parameter to modify (e.g., semi-major axis or inclination) and the determination of the optimal sail orientation to maximize the instantaneous rate of change of this parameter (Carzana et al., 2022; Stolbunov et al., 2013). The optimal sail orientation is expressed relative to the direction of the Sun, as shown in Figure 2.8, where α^* is the optimal sail orientation

to maximize the SRP acceleration along the defined primer vector, $\boldsymbol{\lambda}$, which defines the optimal thrusting direction. While analytical solutions exist to maximize the independent effects of SRP or atmospheric drag, no known analytical control laws exist to maximize their combined effect.

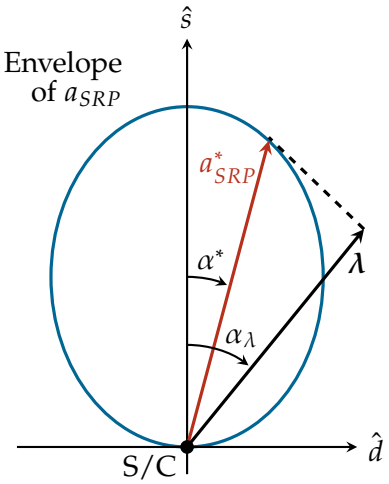

Figure 2.8: Solar sail acceleration envelope, including the optimal acceleration vector, a_{SRP}, and primer vector, $\boldsymbol{\lambda}$ (adapted from Carzana et al. (2022)).

Various attitude control systems have been proposed and implemented for solar sails. Traditional approaches include reaction wheels or control moment gyroscopes mounted on a rigid central bus (Wie, 2004). More innovative methods exploit SRP itself for control, such as tip-mounted vanes that create differential forces, sliding masses that adjust the center of mass relative to the center of pressure, and variable reflectivity devices that modify the local optical properties of the sail (Chujo, 2022; Gauvain & Tyler, 2023; Mangus & Heaton, 2004). Recent research has explored morphing or variable-shape sail designs that enable more sophisticated control strategies by actively changing the sail geometry (Chujo, 2022; Kubo & Chujo, 2024).

Recent advances in solar-sailing capabilities have enabled new applications in Earth orbit and beyond. Techniques for utilizing SRP for orbit modification, station-keeping, and relative positioning have been developed and demonstrated by recent missions (Cao et al., 2020; Meireles et al., 2023; Polat & Tekinalp, 2020). These advances provide the foundation for applying solar-sailing technology for novel applications involving orbital control. While the utlization of SRP has been theorized for many decades, its use for orbital modification of Earth-bound orbits is still a nascent field of research.

2.3. Collision-Avoidance Methods and Limitations

This section provides an overview of conventional collision-avoidance methods and their limitations followed by a discussion of novel applications, including the use of natural forces such as SRP and drag.

Conventional Collision-Avoidance Methods

Conventional collision avoidance relies predominantly on propulsive maneuvers executed before the TCA to modify the conjunction geometry and reduce collision probability (Patera & Peterson, 2003). These maneuvers must balance effectiveness in reducing collision risk against constraints such as

propellant consumption, operational impact, and the need to maintain the primary mission orbit (Kim et al., 2012).

The optimal maneuver direction depends on the specific conjunction geometry, with the most efficient approach typically being to increase the miss distance in the direction that maximizes the reduction in collision probability per unit of velocity change (ΔV). For short-term conjunctions with well-defined relative geometry, this optimal direction often aligns approximately with the semi-minor axis of the combined position uncertainty ellipse in the encounter plane, generally perpendicular to the relative velocity vector (Gonzalo et al., 2021a; Patera & Peterson, 2003).

The timing of avoidance maneuvers involves an important trade-off. Maneuvers executed earlier provide more time for the position offset to grow through a longer maneuver duration, potentially requiring less ΔV for a given miss distance. However, earlier maneuvers are based on less accurate predictions, as the uncertainty generally grows with prediction time (Gonzalo Gomez et al., 2019). Conversely, later maneuvers benefit from refined predictions but may require larger ΔV and provide less time for verification and contingency planning (Carer & Mooij, 2025). Early maneuvers may lead to performing more maneuvers than necessary, since waiting longer may lead to a decrease in P_c, thus removing the need for a maneuver.

Various analytical and numerical approaches have been developed for designing optimal avoidance maneuvers. Analytical methods, such as those developed by Patera and Peterson (Patera & Peterson, 2003) and Gonzalo et al. (Gonzalo et al., 2021a), provide closed-form solutions for simplified scenarios that enable rapid evaluation of maneuver options. These approaches typically approximate the maneuver effect through linearized dynamics and simplified perturbation models. More comprehensive numerical optimization techniques incorporate high-fidelity propagation models and can account for operational constraints, multiple conjunctions, and long-term orbit maintenance requirements (Palermo et al., 2021).

Recent research has expanded conventional approaches to include continuous low-thrust maneuvers, which offer advantages in efficiency and flexibility for spacecraft equipped with electric propulsion systems (De Vittori et al., 2022; Hernando-Ayuso & Bombardelli, 2021). These maneuvers distribute the avoidance actuation over an extended period, potentially reducing the peak acceleration and allowing for more optimal use of limited power resources (Salemme et al., 2020). Studies by De Vittori et al. (De Vittori et al., 2022) and Hernando-Ayuso and Bombardelli (Hernando-Ayuso & Bombardelli, 2021) have demonstrated that low-thrust approaches can achieve comparable or superior collision risk reduction with lower propellant consumption compared to impulsive maneuvers, particularly when planned with sufficient lead time.

Despite the advances in low-thrust technology, several limitations persist that motivate the exploration of alternative approaches. The most fundamental constraint is the finite propellant reserves carried by most spacecraft, which limit the number of avoidance maneuvers that can be performed throughout a mission lifetime (Sánchez-Ortiz et al., 2006). For spacecraft near the end of their operational lives or those that have experienced propulsion system failures, conventional avoidance capabilities may be severely limited or unavailable (Mishne & Edlerman, 2017).

While collision-avoidance is an effective method for mitigating the risk of collisions in orbit, it does not solve the underlying threat caused by a growing population of debris. As the number of debris objects increase, the number of required maneuvers will simultaneously increase, potentially reaching an unsustainable state. To prevent this state, it is necessary to remove defunct satellites from orbit. Most satellites at sufficiently low altitudes de-orbit and burn up in the atmosphere, but large, defunct satellites remain in orbit for years, continuing to pose a threat (Klinkrad et al., 2006). In order to reduce the threat posed by such satellites in orbit, active debris removal (ADR) missions have been proposed to capture and de-orbit these objects. These missions typically involve rendezvous and capture of the target object, followed by controlled re-entry into Earth's atmosphere to ensure safe disposal (Liou et al., 2010). However, these missions are limited by their ΔV, particularly when multiple debris targets need to be removed (Bonnal et al., 2013). The SWEEP (Space-waste Elimination around Earth by Photon Propulsion) project aims to demonstrate the use of solar-sail technology for ADR by capturing and de-orbiting multiple debris objects during a single mission [1]. Due to the large surface areas of solar sails, they can experience increased collision risks during their mission. The use of SRP and atmosphere drag to perform collision-avoidance maneuvers can be particularly beneficial for such missions.

Novel Collision-Avoidance Methods

The increasing number of conjunction warnings presents operational challenges for satellite operators. As the orbital population grows, the frequency of warnings requiring assessment and potential response is expected to increase substantially (Le May et al., 2018). For satellites equipped with conventional electric thrusters, a higher frequency of collision-avoidance maneuvers will require larger power budgets or lead to compromises in the power budgets for other systems - this is a significant limitation as satellites are becoming increasingly power-hungry given the trend in onboard-computing and data-processing (Mishne, 2016; Weston et al., 2025).

These limitations have motivated research into alternative approaches, including nature-driven collision-avoidance maneuvers that exploit environmental forces rather than onboard propellant. Nature-driven maneuvers could lead to extended mission lifetimes through propellant conservation and continued collision-avoidance capability for propellant-depleted spacecraft (Kim, 2024; Mishne & Edlerman, 2017). Additionally, these approaches offer cost efficiency for satellites requiring multiple avoidance maneuvers and promote sustainable space operations by reducing reliance on consumable resources (Yang Yang et al., 2016).

Two primary environmental forces have been investigated for nature-driven collision avoidance: atmospheric drag and SRP. Differential drag approaches exploit variations in spacecraft cross-sectional area relative to the velocity vector to modulate atmospheric drag forces, enabling orbital adjustments at lower altitudes (Varma, 2021). However, these methods are limited to orbits with sufficient atmospheric density, primarily below approximately 600-800 km (Gonzalo Gomez et al., 2018). Drag augmentation has been operationally demonstrated for orbit insertion via constellation phasing by Planet, a commercial Earth observation company, highlighting the practical viability of differential drag for orbit control (Foster et al., 2018). While the theoretical viability of differential drag-based

[1] https://www.tudelft.nl/lr/sweep (accessed on 12 March 2025)

collision avoidance has been established, it has not been operationally implemented yet (Aranda et al., 2024; Serfontein et al., 2021).

SRP-based methods allow for orbital control through the appropriate orientation of solar panels, deployable structures, or dedicated solar sails. Spacecraft can harness SRP to perform collision-avoidance maneuvers without consuming propellant given sufficient time and suitable orbital and physical parameters (Mishne & Edlerman, 2017). The primary advantage of SRP-based collision avoidance is the propellant-less nature of the approach, which offers the possibility of extending mission lifetimes by conserving limited propellant resources for primary mission objectives (Mishne & Edlerman, 2017). For spacecraft that rely on electric propulsion with very limited thrust capability, SRP-based methods may provide comparable effectiveness without power consumption or thruster operational constraints (De Vittori et al., 2022). The effect of SRP is the most significant on solar sails, making them potentially suitable for collision-avoidance applications.

The force direction available through SRP is constrained by the Sun-spacecraft geometry, limiting maneuverability compared to conventional propulsion systems that can thrust in virtually any direction (Kim, 2024). The optimal maneuvering direction for collision avoidance depends on the specific conjunction geometry and is generally perpendicular to the relative velocity vector at closest approach (Patera & Peterson, 2003). However, the available SRP force direction is constrained to the half-space facing away from the Sun, with maximum force in the Sun-spacecraft direction (McInnes, 2004).

Environmental factors further limit SRP-based control. Earth's shadow interrupts the effect of SRP during eclipse periods, creating potential discontinuities in the planned maneuver that must be accounted for in the design process (Ismail et al., 2015). In lower orbits, atmospheric drag interferes with SRP effects, potentially enhancing or counteracting the desired maneuver depending on the specific geometry and spacecraft orientation (Gonzalo Gomez et al., 2019). SRP and drag each create unique acceleration envelopes for solar sails which are highly dependent on the sail's attitude, its orbital regime, and its position in orbit. While the two accelerations may counteract the effects of each other, they can also be combined to achieve more effective maneuvers in certain scenarios (Carzana et al., 2022). The combined effect of SRP and drag on solar sails for collision avoidance has not been thoroughly investigated, and the potential benefits and limitations of this approach remain to be explored.

However, the prospect of SRP-based collision avoidance faces significant challenges that must be addressed to establish its viability as a practical approach. The relatively weak magnitude of SRP compared to conventional propulsion systems represents the most fundamental limitation (Kim, 2024). The characteristic acceleration, which accounts for a spacecraft's AMR, achievable through SRP typically ranges from 10^{-3} to 10^{-2} mm/s^2 for dedicated solar-sail missions (Spencer et al., 2019). These accelerations are several orders of magnitude lower than chemical propulsion systems and significantly less than typical electric propulsion options.

A solar sail's limited acceleration envelope and magnitude may necessitate longer lead times for effective avoidance maneuvers. Research by Mishne and Edlerman (Mishne & Edlerman, 2017)

suggests that for conventional satellites with solar panels, SRP-based methods may require three to seven days of continuous operation to achieve miss distances comparable to conventional approaches, depending on the specific conjunction geometry and spacecraft characteristics. This requirement contrasts with traditional impulsive maneuvers, which can generate significant displacement within hours of execution (Sánchez-Ortiz et al., 2006).

Recent work by Ambrosio (2025) shows that solar sails are capable of performing CAMs with an average maneuver duration of 25 minutes at altitudes above 1000 km. The work considered an ideal sail under the influence of central and J_2 gravity and SRP, and simulated a range of physical, orbital and conjunction parameters. A "real", more conservative case was also simulated, which led to an increase in average maneuver duration to 47 minutes. The sail was found to largely thrust in the direction of sunlight with an in-plane acceleration component always present. Further, eclipses were found to increase the maneuver duration. The results show that the performance of analytical LOCLs is similar to that of numerical optimization methods, indicating that such control laws may be utilized for performing CAMs. The work did not consider the effects of atmospheric drag as the altitudes assessed were above 1000 km. This is the only known literature focused on solar-sail applications for collision-avoidance, and presents promising results that fit within current operational frameworks for CAMs.

3 Research Objective

Through the discussion in Chapter 2, a gap in existing literature was identified: the application of sailcraft for collision-avoidance maneuvers using locally optimal control laws at altitudes where drag cannot be neglected. This section presents the research objective and research questions that will be addressed during the thesis.

Existing literature on novel collision-avoidance methods using SRP and atmospheric drag is limited to low area-to-mass ratio (LAMR) objects, which result in maneuver durations in the order of days. Recent demonstrations of solar-sail applications in LEO indicate that a sailcraft in an Earth-bound orbit is capable of maneuvering using SRP alone (Ancona & Kezerashvili, 2024). Literature on the applications of such maneuvering capabilities for collision-avoidance is, however, very limited.

The most relevant work related to collision-avoidance applications of sailcraft focused on higher orbits where SRP and J_2 gravity were the only considered perturbations (Ambrosio, 2025), creating a knowledge gap in lower orbital regimes. Further, Ambrosio (2025) showed that the performance of locally optimal control laws do not significantly deviate from numerical optimization methods, suggesting a simplified control approach may be sufficient in achieving optimal maneuver durations. Addressing this research gap will help further characterize the collision-avoidance capability of sailcraft in LEO and contribute to existing knowledge on the use of drag and SRP for maneuvering.

The following research objective and research questions are formulated to address the identified research gap:

Research Objective

Evaluate the performance and applicability of locally optimal control laws for executing collision-avoidance maneuvers of sailcraft in LEO between altitudes of 400 and 800 km.

Research Question 1

What are the minimum maneuver durations required to safely maneuver a sailcraft away from a predicted collision using locally optimal control laws under the influence of solar radiation pressure and atmospheric drag at altitudes between 400 and 800 km?

Research Question 2

How are maneuver durations and the usage of control laws affected by different physical, orbital and conjunction parameters, such as the sailcraft's area-to-mass ratio, altitude, aspect angle, and miss distance at the time of closest approach?

4 Methodologies

This chapter discusses the methodologies utilized in this work. Section 4.1 discusses the set-up of the dynamical model, followed by Section 4.2 which explains the implementation of analytical and numerical control laws. Section 4.3 presents the methods to generate representative synthetic uncertainties, which are used in defining a conjunction scenario between two objects in Section 4.4. Finally, Section 4.5 presents the optimization methods used to compute optimal collision-avoidance maneuvers.

4.1. Dynamical Model

The dynamical model involves the creation of a numerical model in which defined sail and debris objects can be propagated under the influence of perturbing forces. Subsection 4.1.1 presents the reference frames utilized for the propagation and calculation of accelerations. Subsection 4.1.2 provides the formulation of the equations of motion and methods used to compute the accelerations caused by each perturbing force. Finally, Subsection 4.1.3 provides an overview of the selection of parameters used for the numerical integration and propagation.

4.1.1. Reference Frames

This work utilizes three different reference frames. The Earth-centered Inertial (ECI) reference frame, illustrated in Figure 4.1, is used for orbit propagation. $\hat{x}_{ECI}$ points towards the vernal equinox, $\hat{z}_{ECI}$ points towards the geographic North Pole, aligned with Earth's rotation axis, and $\hat{y}_{ECI}$ completes the right-handed frame (Vallado, 2001).

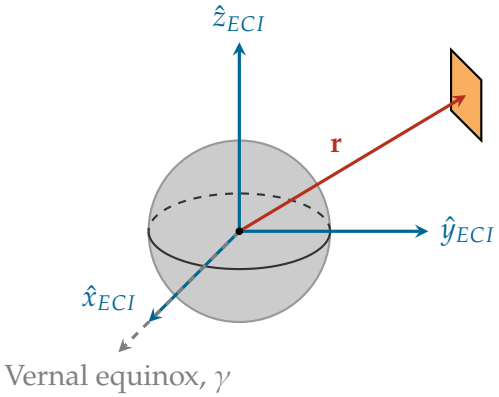

Figure 4.1: Earth-Centered Inertial (ECI) reference frame with **r** defining the sail position

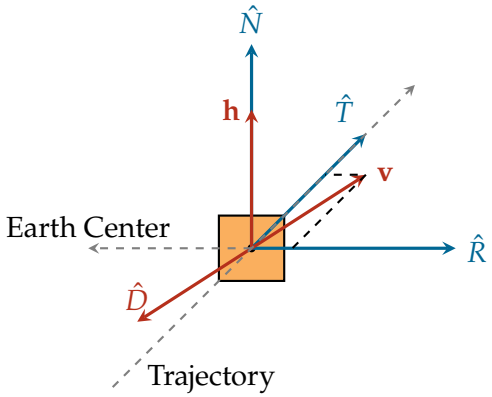

Figure 4.2: Radial-Tangential-Normal (RTN) reference frame centered on the solar sail.

The Radial-Tangential-Normal (RTN) reference frame, illustrated in Figure 4.2, is used for the formulation of state covariance ellipsoids and calculation of aerodynamic forces and miss distances

at TCA. $\hat{R}$ points in the radial direction, away from the Earth's center towards the spacecraft. $\hat{N}$ points in the normal direction, aligned with the orbital angular momentum vector, and $\hat{T}$ points in the tangential direction, completing the right-handed frame.

The third reference frame used in this analysis is the sunlight reference frame, which is useful for modeling SRP effects. The sunlight reference frame is illustrated in Figure 4.3, reproduced from Carzana et al. (2022). $\hat{x}_s$ points in the direction of sunlight, away from the Sun, $\hat{y}_s = \hat{z}_{ECI} \times \hat{x}_s$, and $\hat{z}_s$ completes the right-handed frame. The sail normal vector, $\boldsymbol{n}$, and cone angle, α, are used in the formulation of the SRP acceleration, in Section 4.1.2.

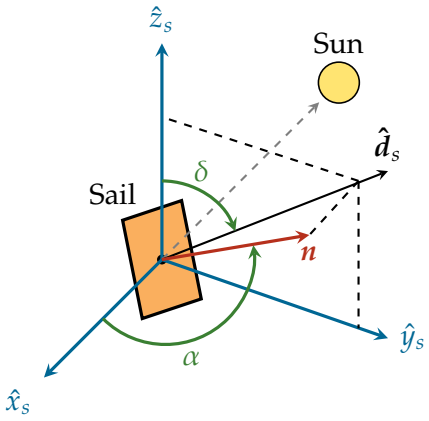

Figure 4.3: Sunlight reference frame with cone angle, α, and clock angle, δ (adapted from Carzana et al. (2022)).

The aspect angle, β, is defined as the angle between the angular momentum vector of the sail's orbit, **h** and the Sun-Earth direction, $\hat{x_s}$, and will be used in the explanation of methodologies and discussion of results in this report due to its effectiveness in quantifying the performance of solar sails (Gámez Losada et al., 2024).

4.1.2. Equations of Motion

The equations of motion are formulated using the object state in Cartesian coordinates. This allows for the sum of the forces acting on the object at a given moment to be integrated over time. The four forces considered are the central and J_2 gravity of the Earth, atmospheric drag, and SRP. In LEO regimes of altitudes below 800 km, J_2 and atmospheric drag are dominant perturbing forces (Reid, 2017), and given the analysis of solar sails in this work, SRP is also considered a significant force. The equations of motion in Cartesian coordinates of a spacecraft in the ECI reference frame are expressed as:

$$\frac{d\mathbf{r}}{dt} = \mathbf{v} \tag{4.1}$$

$$\frac{d\mathbf{v}}{dt} = \mathbf{a}_{total} = \mathbf{a}_{gravity} + \mathbf{a}_{J_2} + \mathbf{a}_{SRP} + \mathbf{a}_{drag} \tag{4.2}$$

where $\mathbf{r} = [x, y, z]^T$ represents the position vector, $\mathbf{v} = [v_x, v_y, v_z]^T$ denotes the velocity vector, and

$\mathbf{a}_{total}$ is the total acceleration vector comprising contributions from Earth's central gravity and the three perturbing forces.

Point Mass Gravity

The primary gravitational acceleration due to Earth's central mass is modeled as a point mass attraction (Wakker, 2015):

$$\mathbf{a}_{gravity} = -\frac{\mu_{Earth}}{r^3}\mathbf{r} \tag{4.3}$$

where $\mu_{Earth} = 3.986004418 \times 10^{14}$ m^3/s^2 is Earth's standard gravitational parameter (Vallado, 2001) and $r = |\mathbf{r}|$ is the magnitude of the position vector.

J_2 Perturbation

The oblateness of Earth introduces a significant perturbation to the gravitational field, modeled through the J_2 coefficient. The J_2 perturbation acceleration is given by (Yang et al., 2022):

$$\mathbf{a}_{J_2} = \frac{3\mu_{Earth}J_2R_{Earth}^2}{2r^4}\begin{bmatrix} x\left(5\frac{z^2}{r^2}-1\right) \\ y\left(5\frac{z^2}{r^2}-1\right) \\ z\left(5\frac{z^2}{r^2}-3\right) \end{bmatrix} \tag{4.4}$$

where $J_2 = 1.08262668 \times 10^{-3}$ and $R_{Earth} = 6.378137 \times 10^6$ m is Earth's equatorial radius.

Solar Radiation Pressure Model

An ideal sail model is considered to be sufficient given the scope and focus of this work, and is used for the calculation of the acceleration due to SRP with the following assumptions:

- Flat and rigid surface
- Specular reflection
- No externally-induced torques
- Constant SRP

These assumptions dictate that all SRP accelerations act through the sail's center of mass and along its normal. The SRP acceleration is thus modeled in the sunlight reference frame as (McInnes, 2004):

$$\mathbf{a}_{SRP} = \nu a_c cos^2\alpha \boldsymbol{n} \tag{4.5}$$

where $\nu \in [0,1]$ is the shadow factor, α is the cone angle as defined in Figure 4.3, $\mathbf{n}$ is the sail normal vector defined in the sunlight reference frame, and a_c is the characteristic acceleration, defined as (McInnes, 2004):

$$a_c = \frac{2P_0}{c\sigma_s} \tag{4.6}$$

with the following terms redefined for convenience: $P_0 = 1361\ W/m^2$, representing the solar flux constant at 1 AU, c = 299792458 m/s, representing the speed of light, and σ_s is the sail loading parameter, defined as the ratio of the sail's mass to surface area.

Atmospheric Drag Model

Atmospheric drag becomes the dominant perturbing force at low altitudes, particularly below altitudes of 800 km during times of high solar activity, as shown in Figure 4.5a. The NRLMSISE-00 empirical density model is used in this work due to its higher fidelity in comparison to exponential and other standard atmospheric models (Picone et al., 2002). The drag acceleration for a satellite in LEO is modeled using (Vallado & Finkleman, 2014):

$$\mathbf{a}_{drag} = -\frac{1}{2}\frac{\rho A_{drag} C_D}{m}\mathbf{v}_{rel}|\mathbf{v}_{rel}| \tag{4.7}$$

where:

- ρ is the atmospheric density
- A_{drag} is the effective cross-sectional area
- C_D is the drag coefficient
- $\mathbf{v}_{rel}$ is the velocity vector relative to the rotating atmosphere

For an exponential atmosphere, the density is modeled as (Vallado & Finkleman, 2014):

$$\rho(h_{alt}) = \rho_0 \exp\left(-\frac{h_{alt} - h_0}{H}\right) \tag{4.8}$$

where ρ_0 is the reference density, h_{alt} is the altitude, h_0 is the reference altitude, and H is the scale height. The NRLMSISE-00 model incorporates solar and geomagnetic activity indices to provide time-dependent density estimates based on (Picone et al., 2002):

$$\rho = f(h_{alt}, \theta_{lat}, \theta_{lon}, t, F_{10.7}, F_{10.7A}, A_p) \tag{4.9}$$

where θ_{lat} and θ_{lon} are the geographic latitude and longitude, respectively, t is the epoch, $F_{10.7}$ is the daily solar flux index, $F_{10.7A}$ is the 81-day average solar flux, and A_p is the geomagnetic index.

The variation in SRP is approximately 0.1% during the 11-year solar cycle, and is therefore considered negligible in comparison to the sensitivity of the atmospheric density to changes in the flux and geomagnetic indices (Ermolli et al., 2013). The main parameters affecting the output of the NRLMSISE-00 model are the solar, geomagnetic and geographic parameters. In this work, the atmosphere is considered to be homogenous across latitudes and longitudes, as these parameters have relatively smaller effects on the computed density in comparison to the solar and geomagnetic flux (Picone et al., 2002).

To assess the sensitivity of the atmospheric density model implemented in this work to solar and geomagnetic fluxes, minimum and maximum values for these parameters during the 11-year solar cycle are chosen based on Figure 4.4 and plotted for the modelled perturbations at different altitudes, in Figure 4.5, which is shown for an AMR of 5 m^2/kg for circular orbits and C_D = 2.2 = and C_r = 1, representing the drag and radiation coefficients, respectively (Colombo et al., 2017).

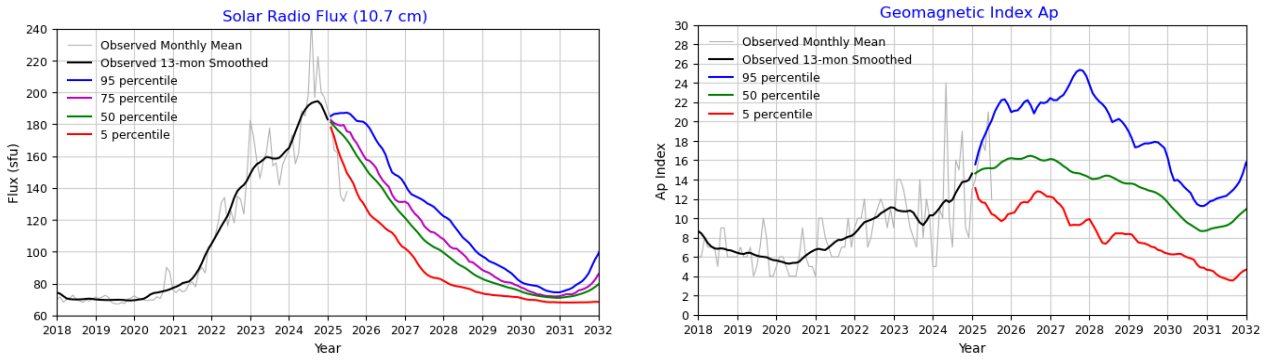

(a) **(b)**

Figure 4.4: F10.7cm flux data and geomagnetic index used in the NRLMSISE-00 model. (a) F10.7cm flux variation and (b) geomagnetic A_p index measurements and predictions (NASA Marshall Space Flight Center, 2025).

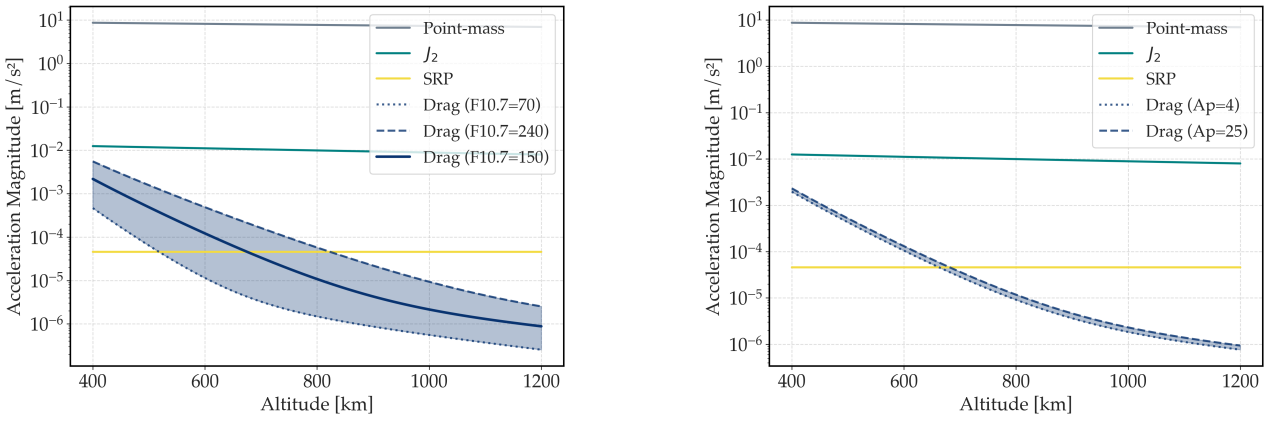

(a) **(b)**

Figure 4.5: Variation of point-mass gravity, J_2, SRP and drag accelerations with altitude, including the range of drag variation between Solar minimum and maximum for (a) F10.7cm flux variation and (b) geomagnetic A_p index variation for default values of A_p = 15 and F10.7 flux = 150, respectively.

Figure 4.5 shows that depending on the point within a solar cycle, the magnitudes of SRP and drag are equal between an altitude range of approximately 520 to 830 km for minimum and maximum solar flux values. The variation indicates that the acceleration due to drag is highly sensitive to the solar cycle. The A_p boundaries lead to a variation of up to approximately 20 km in altitude at which the relative magnitude of the SRP and drag forces are equal. The analyses in this work are performed for average flux and geomagnetic values, but Figure 4.5 will help contextualize the obtained results.

Eclipse Modeling

The solar radiation pressure is interrupted during eclipse periods when the spacecraft passes through Earth's shadow. A conical eclipse model, as illustrated in Figure 4.6, is implemented to determine the eclipse state:

$$\nu = \begin{cases} 0 & \text{if } \theta_{sep} < \theta_{Earth} + \theta_{Sun} \\ 1 & \text{otherwise} \end{cases} \tag{4.10}$$

where θ_{sep} is the angular separation between Earth and Sun as viewed from the spacecraft, $\theta_{Earth} = \arcsin(R_{Earth}/r)$ is Earth's angular radius, and $\theta_{Sun} = \arcsin(R_{Sun}/r_{Sun})$ is the Sun's angular radius, with $R_{Sun} = 6.957 \times 10^8$ m representing the Sun's radius (Vallado, 2001) and r_{Sun} representing the position of the spacecraft with respect to the Sun. While a continuous shadow function is typically utilized to model shadow factors between zero and one within the penumbra region (Li et al., 2019), this work assumes that a shadow factor of $\nu = 0$ is used in both umbra and penumbra regions to remain conservative.

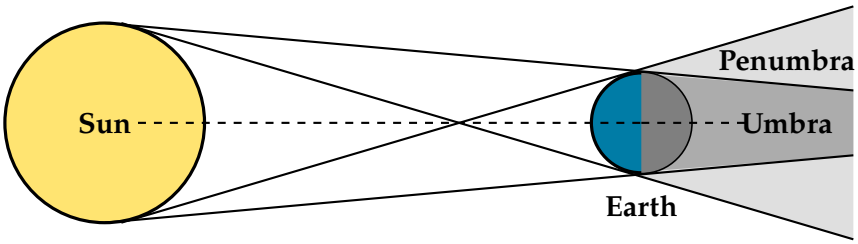

Figure 4.6: Conical eclipse geometry showing the umbra and penumbra regions formed by Earth's shadow (not to scale).

4.1.3. Numerical Integration

For the propagation of the sail's state, the Cowell propagator is chosen as it demonstrates high accuracy for propagations including geo-potential and drag perturbations (Pollock, 1994). However, according to Pollock (1994), the Cowell propagator, while the most accurate, is also computationally expensive. To choose a suitable combination of accuracy and computational efficiency, an integrator analysis is conducted to select a specific integrator and appropriate relative and absolute tolerances. The chosen settings from the integrator analysis along with other parameters used in the dynamical model are provided in Table 4.1. The results of the integrator analysis can be found in Appendix A.

Table 4.1: Parameters used for the set-up of the dynamical model, including environment models and numerical propagator/integrator choices.

Parameter	Selection
Gravity	Oblate Earth (central and J_2)
Atmospheric density	NRLMSISE-00
SRP model	Ideal
Sun ephemeris	SPICE
Eclipse	Conical (conservative)
Propagator	Cowell
Integrator	DOP853 (rtol = 10^{-8}, atol = 10^{-8})

4.2. Control Laws

This section describes the control laws utilized in this work. The control objective is driven by the need to modify the spacecraft's orbit to reduce the collision probability at a predicted conjunction. This work considers the use of locally-optimal control laws to maximize the instantaneous rate of change of specific orbital elements; a specific subset of these control laws demonstrated similar performance to a direct collocation method (Ambrosio, 2025), and their applicability is therefore assessed in this work. Subsection 4.2.1 provides the thrusting vectors for locally-optimal control, followed by an analytical formulation of the optimal sail orientation to maximize accelerations along the optimal thrusting vector in Subsection 4.2.2. Subsection 4.2.3 develops a numerical methodology for computing the optimal sail orientation when subject to both SRP and drag forces.

4.2.1. Locally-optimal Control

The optimization of orbital element rates under low-thrust propulsion is formulated using Gauss's planetary equations in the RTN reference frame. For a spacecraft subjected to perturbative acceleration $\mathbf{a} = [a_R, a_T, a_N]^T$, the instantaneous rates of change of classical orbital elements are governed by (Battin, 1999; Pu et al., 2025):

$$\frac{da}{dt} = \frac{2a^2}{h}\left[a_R e \sin\theta + a_T \frac{p}{r}\right] \tag{4.11}$$

$$\frac{de}{dt} = \frac{a}{h}\left[a_R \sin\theta + a_T(\cos\theta + \cos E)\right] \tag{4.12}$$

$$\frac{di}{dt} = \frac{a\cos u}{h} a_N \tag{4.13}$$

$$\frac{d\Omega}{dt} = \frac{a \sin u}{h \sin i} a_N \tag{4.14}$$

where $h = \sqrt{\mu a(1-e^2)}$ is the specific angular momentum, $p = a(1-e^2)$ is the semi-latus rectum, θ is the true anomaly, E is the eccentric anomaly, and $u = \omega + \theta$ is the argument of latitude. The argument of periapsis is omitted in this analysis as its locally-optimal control law is undefined for eccentricities of $e = 0$ (Macdonald & McInnes, 2005). The true anomaly is not considered a modifiable orbital element as it only describes the position of an object within its orbit, and not the orbit's shape, size, or orientation (Nugnes, Colombo, et al., 2022).

Each orbital element rate can be expressed as a linear combination of acceleration components:

$$\frac{d(\text{œ})}{dt} = C_R a_R + C_T a_T + C_N a_N \tag{4.15}$$

where the coefficients C_R, C_T, and C_N are extracted directly from Gauss's equations. To maximize the instantaneous rate of change for a given thrust magnitude, the optimal thrust direction $\boldsymbol{\lambda}_{\text{opt}}$ must align with the coefficient vector $\mathbf{C} = [C_R, C_T, C_N]^T$ (Kechichian, 1997):

$$\boldsymbol{\lambda}_{\text{opt}} = \frac{\mathbf{C}}{|\mathbf{C}|} \tag{4.16}$$

Applying the optimization methodology to each orbital element yields the following optimal thrust directions, or primer vectors, in the RTN frame:

$$\boldsymbol{\lambda}_{O,a} = \begin{bmatrix} e\sin\theta \\ 1 + e\cos\theta \\ 0 \end{bmatrix} \tag{4.17}$$

$$\boldsymbol{\lambda}_{O,i} = \begin{bmatrix} 0 \\ 0 \\ \text{sgn}(\cos(\omega + \theta)) \end{bmatrix} \tag{4.18}$$

$$\boldsymbol{\lambda}_{O,e} = \begin{bmatrix} \sin\theta \\ \cos\theta + \cos E \\ 0 \end{bmatrix} \tag{4.19}$$

$$\boldsymbol{\lambda}_{O,\Omega} = \begin{bmatrix} 0 \\ 0 \\ \text{sgn}(\sin(\omega + \theta)) \end{bmatrix} \tag{4.20}$$

These results demonstrate that in-plane orbital modifications require coordinated radial and tangential thrust components, while out-of-plane changes are achieved through strategically timed normal thrust maneuvers. The detailed mathematical derivations for each orbital element are provided in Appendix B.

4.2.2. SRP-only Control

An analytical formulation for optimal sail orientation to maximize the SRP acceleration along a primer vector, defined in Equations 4.17-4.20, is provided by McInnes (2004). Given α_λ and δ_λ, which define the cone and clock angles of the primer vector in the sunlight reference frame, respectively, the optimal cone and clock angles can be formulated.

The optimal cone angle, α_{opt}, is determined by:

$$\alpha_{opt} = \tan^{-1}\left(\frac{-3\cos\alpha_\lambda + \sqrt{9\cos^2\alpha_\lambda + 8\sin^2\alpha_\lambda}}{4\sin\alpha_\lambda}\right) \tag{4.21}$$

The optimal clock angle, δ_{opt}, is given by:

$$\delta_{opt} = \delta_\lambda \tag{4.22}$$

These optimal cone and clock angles provide the instantaneously optimal sail orientation for maximizing the rate of change of the desired orbital elements along the relevant primer vectors in Equations 4.17 - 4.20. This analytical control law will be referred to as SRP-only, as it only maximizes the SRP acceleration component along the primer vector. Since the research objective of this work involves analyses at low altitudes where atmospheric drag is non-negligible, a control law that accounts for the effects of both SRP and drag needs to be implemented. The SRP-only control law will still be suitable at altitudes above approximately 800 km, where atmospheric drag effects are negligible.

4.2.3. SRP+Drag Control

Unlike the SRP-only control law, no analytical formulation exists to maximize the combined effect of SRP and drag along a primer vector (Carzana et al., 2022). Carzana et al. (2022) presents a sophisticated numerical optimization method to formulate a "full-dynamics" locally-optimal control law to find optimal sail orientations under both SRP and drag effects. However, reproducing this methodology was considered to be out of the scope of this work. A simplified grid-search method is implemented in this work instead.

Given that a single-phase grid-search would be too computationally expensive to obtain accurate results, a hierarchical grid-search is implemented. To limit the search space, a two-stage grid-search is performed, using a coarse grid to identify the best potential areas and then using a finer grid to converge to the optimal orientation. This method allows for a more efficient search space when compared to a full grid-search over all possible orientations. However, there are potential pitfalls to using this method; there is no guarantee of global minimum given the restricted and discrete nature of the search. Further, when the relative drag magnitude is large, near-edgewise cases can lead to rapid changes in the optimal normal vector, as there are multiple attitudes at which drag is minimized. These edge-cases were tested for selected scenarios in which expected convergence was observed, but there is no guarantee that unexpected behaviour may not arise in certain scenarios.

The SRP+drag control problem can be formulated as an optimization of the combined acceleration vector $\mathbf{a}_{\text{SRP+drag}}$ acting on the solar sail, which comprises contributions from both SRP and atmospheric drag:

$$\mathbf{a}_{\text{SRP+drag}} = \mathbf{a}_{\text{SRP}}(\alpha, \delta) + \mathbf{a}_{\text{drag}}(\alpha, \delta) \tag{4.23}$$

The SRP and drag acceleration formulations are provided in Chapter 4.1; note that the drag acceleration vector needs to be formulated in the sunlight reference frame with defined cone and clock angles. A lift force is also typically generated in addition to atmospheric drag, but is ignored in this analysis as it is an order of magnitude smaller than drag (Ivanov et al., 2018).

Hierarchical Grid-Search Optimization

The optimization of the combined acceleration along the primer vector $\boldsymbol{\lambda}$ is formulated as:

$$\max_{\alpha,\delta} \quad \boldsymbol{\lambda}^T \mathbf{a}_{\text{SRP+drag}}(\alpha, \delta) \tag{4.24}$$

subject to the physical constraints:

$$0 \leq \alpha \leq \frac{\pi}{2} \tag{4.25}$$

$$0 \leq \delta \leq 2\pi \tag{4.26}$$

Phase 1 - Coarse grid-search: The attitude space is discretized using a coarse grid with resolution $\Delta\alpha_{\text{coarse}}$ and $\Delta\delta_{\text{coarse}}$. The objective function is evaluated at each grid point:

$$f(\alpha_i, \delta_j) = \boldsymbol{\lambda}^T[\mathbf{a}_{\text{SRP}}(\alpha_i, \delta_j) + \mathbf{a}_{\text{drag}}(\alpha_i, \delta_j)] \tag{4.27}$$

where $i = 1, 2, \ldots, N_\alpha$ and $j = 1, 2, \ldots, N_\delta$ represent the discrete grid indices.

Phase 2 - Fine Grid Refinement: The search is refined within a local neighborhood around the optimal solution from Phase 1:

$$\alpha_{\text{fine}} \in [\alpha^* - \Delta\alpha_{\text{coarse}}, \alpha^* + \Delta\alpha_{\text{coarse}}] \tag{4.28}$$

$$\delta_{\text{fine}} \in [\delta^* - \Delta\delta_{\text{coarse}}, \delta^* + \Delta\delta_{\text{coarse}}] \tag{4.29}$$

with finer resolution $\Delta\alpha_{\text{fine}} \ll \Delta\alpha_{\text{coarse}}$ and $\Delta\delta_{\text{fine}} \ll \Delta\delta_{\text{coarse}}$, and α^* and δ^* representing the optimal cone and clock angles, respectively, found through the coarse grid-search.

The coarse and fine grid-searches are visualized in Figure 4.7, showing a uniformly distributed grid across a search space by a range and resolution of cone and clock angles within their respective angular domains. The domains are chosen via trial and error while ensuring that all possible orientations are contained within them.

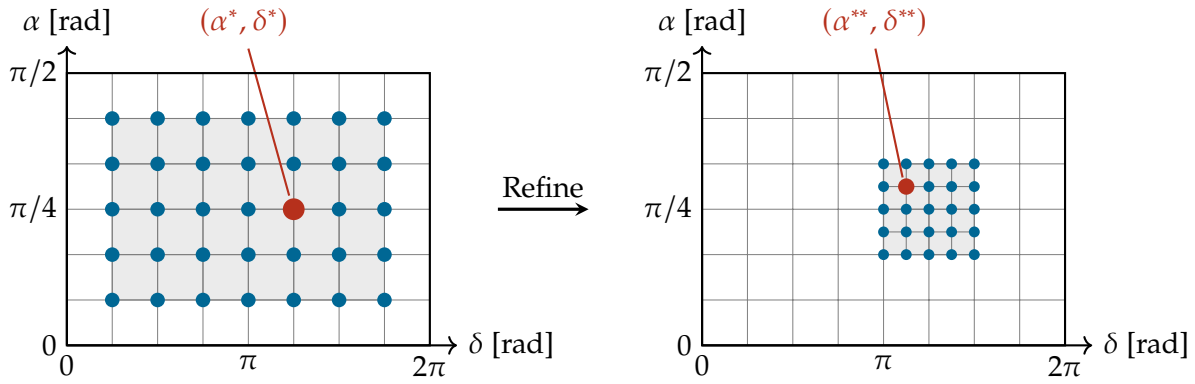

Figure 4.7: Hierarchical grid-search optimization for combined SRP+drag control, employing a two-phase approach: (1) coarse grid evaluation across the attitude search space (α, δ), and (2) fine grid refinement within a local neighborhood of the coarse optimum. The search space is defined by a search angle.

The combined SRP+drag control algorithm is summarized in the following steps:

Algorithm Steps:

1. Evaluate $f(\alpha_i, \delta_j)$ on a uniformly-distributed coarse grid
2. Identify $(\alpha^*, \delta^*) = \arg\max f$
3. Define refinement region around course-optimum using search angle
4. Evaluate $f(\alpha_i, \delta_j)$ on fine grid
5. Return $(\alpha^{**}, \delta^{**}) = \arg\max f_{\text{fine}}$

Force Magnitude Threshold and Switching Logic

The relative significance of SRP and drag forces varies substantially with altitude and sail orientation. To address computational efficiency and control stability, a threshold-based switching mechanism is implemented, such that when either SRP or drag is the dominant force, a switch is made to analytical SRP-only and drag-only control laws. The relative force magnitude ratio is defined as:

$$R_{\text{force}} = \frac{|\mathbf{a}_{\text{SRP}}|}{|\mathbf{a}_{\text{drag}}|} \tag{4.30}$$

$\mathbf{a}_{\text{SRP}}$ and $\mathbf{a}_{\text{drag}}$ were computed using the maximum effective cross-sectional areas in both cases, respectively. A threshold of $R_{\text{force}} = 0.01$ and $R_{\text{force}} = 100$ were chosen for switching to drag-only and SRP-only control laws, respectively, as at these thresholds it was observed that the SRP+drag control law resulted in negligible discrepancies with the drag-only or SRP-only control laws. Once the detected relative magnitude of SRP is below the threshold, the combined control law is simplified to the drag-only binary control method with two modes:

$$\mathbf{n} = \begin{cases} \hat{\mathbf{v}} & \text{(face-on, maximum drag)} \\ \hat{\mathbf{v}} \times \hat{\mathbf{h}} & \text{(edge-on, minimum drag)} \end{cases} \tag{4.31}$$

The face-on and edge-on orientations are optimal for a_{min} (semi-major axis minimization) and a_{max} (semi-major axis maximization) control laws, respectively; since the drag force only acts opposite to the velocity direction, as shown in Equation 4.7, it is not possible to generate accelerations with an out-of-plane component, therefore limiting the drag-only control to SMA (semi-major axis) control laws.

The hierarchical grid-search approach provides a computational advantage over exhaustive search methods, reducing the total number of function evaluations from $O(N_\alpha \times N_\delta)$ to $O(N_{\alpha,\text{coarse}} \times N_{\delta,\text{coarse}} + N_{\alpha,\text{fine}} \times N_{\delta,\text{fine}})$. However, this methodology introduces several inherent limitations that must be acknowledged. The selection of appropriate grid resolutions represents a critical trade-off between solution accuracy and computational expense. Very coarse grids may fail to capture optimal solutions, while overly fine discretizations can lead to very long computation times.

Figures 4.8 and 4.9 show the optimal cone angle achieved by the grid-search for two scenarios in

which the sail is at a true anomaly of 0 degrees in complete sunlight using a_{max} and a_{min} control. In the first scenario, shown in Figure 4.8, the grid-search is performed for varying number of coarse and fine grid points at an altitude of 1000 km, where drag can be neglected. It is expected that the SRP+drag control law converges to the optimal SRP-only sail cone angle in this configuration of +/-35 degrees (McInnes, 2004), which is indeed observed. A step-like convergence is observed, likely due to the discovery of more optimal orientations after a certain increase in grid resolution. Figure 4.9 shows the same results for an altitude of 590 km, where drag is more dominant than SRP but still within the switching threshold, as observed in Figure 4.5a. As expected, the increased effect of drag leads to a compromised cone-angle for a_{max}, but the effect is still dominant enough for the sail to orient itself at a cone angle of 90 degrees, corresponding to a face-on orientation, when using a_{min} control.

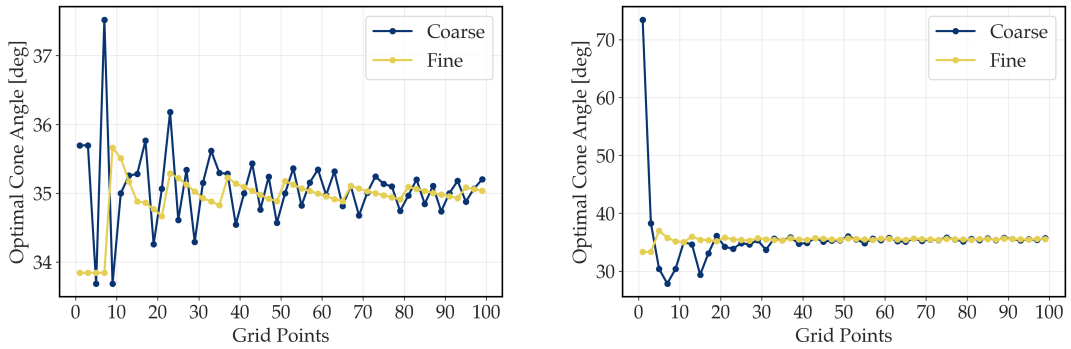

(a) a_{max} **(b)** a_{min}

Figure 4.8: Convergence of the optimal cone angle for the SRP+drag control law at a 1000 km altitude and a true anomaly of zero degrees in complete sunlight for (a) a_{max} and (b) a_{min} control.

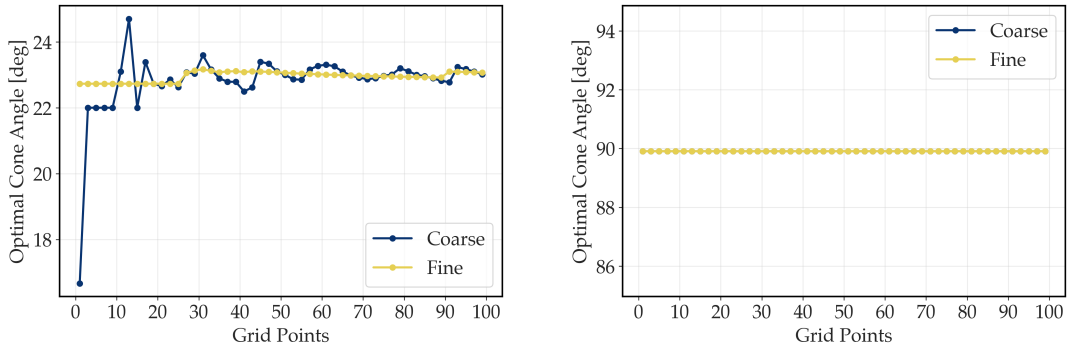

(a) a_{max} **(b)** a_{min}

Figure 4.9: Convergence of the optimal cone angle for the SRP+drag control law at a 590 km altitude and a true anomaly of zero degrees in complete sunlight for (a) a_{max} and (b) a_{min} control.

Table 4.2 presents the parameters used in this analysis for the hierarchical grid-search for the SRP+drag control, found through a mix of trial-and-error and an analysis of the convergence behaviour of the optimal cone angle in obtaining known solutions.

Figures 4.10 and 4.11 show schematics of the sail in relation to the SRP acceleration envelope, $\boldsymbol{\lambda}_{a_{max}}$ and $\boldsymbol{a}_{SRP+drag}$ with its vector components. Figures 4.10 represents the SRP-only control law maximizing

Table 4.2: Parameters used for the grid-search optimization for the SRP+drag control law.

Variable	Value
Coarse Grid Points	20
Fine Grid Points	25
Search angle [deg]	50

$\boldsymbol{a}_{SRP}$ along $\boldsymbol{\lambda}_{a_{max}}$ in the presence of a non-negligible drag acceleration. This results in a $\boldsymbol{a}_{SRP+drag}$ that is ineffective in increasing the SMA due to its negative component along $\boldsymbol{\lambda}_{a_{max}}$. Figure 4.11, on the other hand, maximizes $\boldsymbol{a}_{SRP+drag}$ itself, resulting in a positive component along $\boldsymbol{\lambda}_{a_{max}}$, and thus an increase in the SMA.

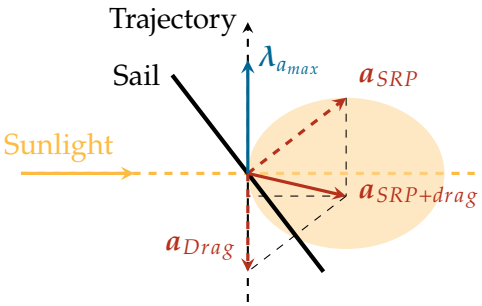

Figure 4.10: Optimal sail orientation at $\theta = 0$ and $\beta = 90$ for maximizing $\boldsymbol{a}_{SRP}$ along $\boldsymbol{\lambda}_{a_{max}}$ in the presence of a non-negligible drag acceleration, $\boldsymbol{a}_{Drag}$.

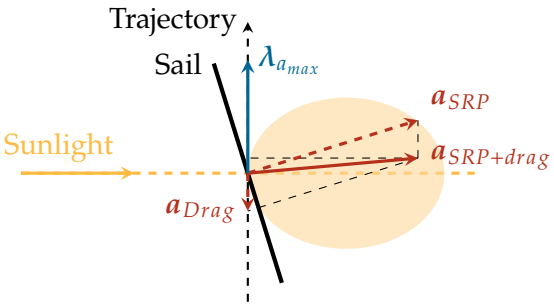

Figure 4.11: Optimal sail orientation at $\theta = 0$ and $\beta = 90$ for maximizing the combined effect of SRP and drag, $\boldsymbol{a}_{SRP+drag}$, along $\boldsymbol{\lambda}_{a_{max}}$.

Figures 4.12 and 4.13 show the evolution of the acceleration vector direction and magnitude for a polar orbit with $\beta = 0$ deg at 1000 km and 590 km, respectively, when using the a_{max} and a_{min} for SRP+drag control. The sail orientation representations in Figures 4.10 and 4.11 correspond to the dark blue dots in Figures 4.12a and 4.13a, respectively. At an altitude of 1000 km, the SRP+drag behaves like the SRP-only control law, with a_{min} in Figure 4.12b showing the acceleration vector directed opposite to the orbit's positive tangent, as expected. At an altitude of 590 km, the effect of drag leads to a face-on orientation with respect to the velocity when using a_{min}, as seen in Figure 4.13b.

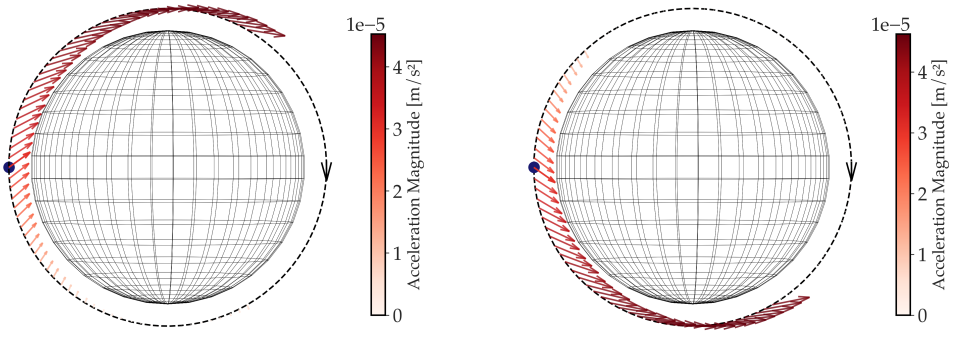

(a) a_{max} **(b)** a_{min}

Figure 4.12: Evolution of the acceleration vector for SRP+drag SMA control laws over one orbit for an aspect angle and inclination of 90 degrees at an altitude of 1000 km.

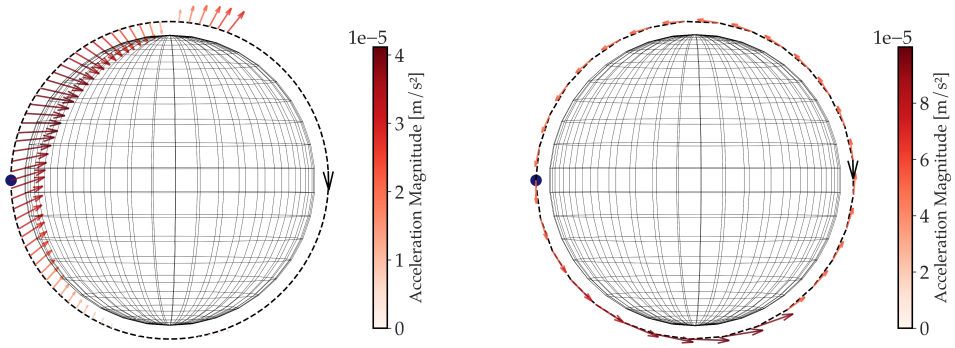

(a) a_{max} **(b)** a_{min}

Figure 4.13: Evolution of the acceleration vector for SRP+drag SMA control laws over one orbit for an aspect angle and inclination of 90 degrees at an altitude of 590 km.

Figure 4.14 shows the evolution of the SMA for a polar orbit with $\beta = 0$ degrees using a_{max} control with respect to a nominal orbit, where the sail normal remains pointed towards the Sun at all times; Figure 4.14a is shown for the SRP-only control law, and Figure 4.14b is shown for the SRP+drag control law. The SRP+drag control is capable of maintaining the SMA with an increase in SMA of approximately 0.1 km in 24 hours compared to a decrease in SMA of approximately 2.7 km for the SRP-only control in the same duration; this decrease is due to $a_{SRP+drag}$ having a negative component along $\lambda_{a_{max}}$, as shown in Figure 4.10. The increase in SMA observed in Figure 4.14b is caused by the positive component of $a_{SRP+drag}$ along $\lambda_{a_{max}}$, corresponding to Figure 4.11. This shows the relative effectiveness of using SRP+drag control over SRP-only control at altitudes where drag cannot be neglected.

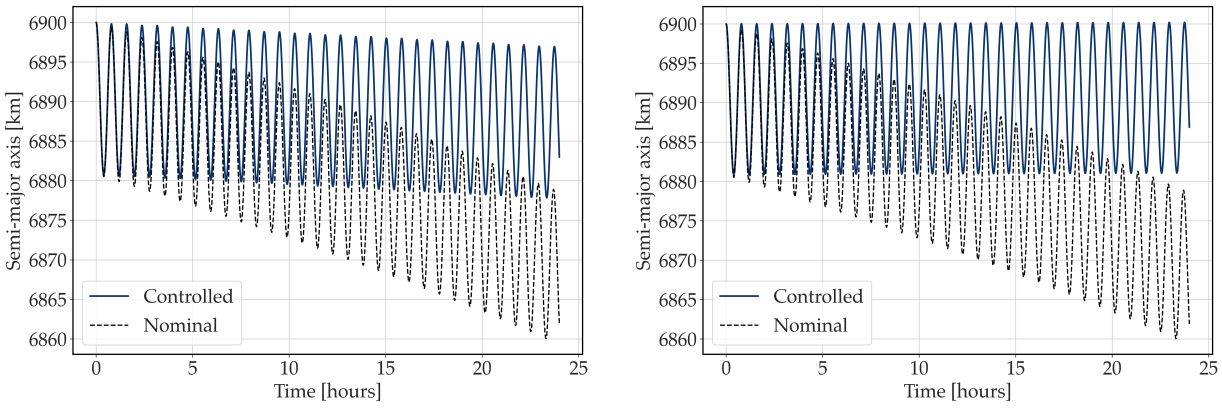

(a) SRP-only **(b)** SRP+drag

Figure 4.14: Evolution of SMA over 24 hours for SRP-only and SRP+drag a_{max} control laws compared to a nominal orbit.

4.3. Uncertainty Generation

In order to simulate the collision risk between two objects, it is necessary to obtain their state uncertainties at the TCA. The reliability of uncertainty characterization, commonly referred to as uncertainty realism, is fundamental for effective Space Situational Awareness and collision avoidance operations. Traditional theoretical covariance matrices generated during orbit determination processes often fail to adequately represent the true orbital uncertainties experienced in operational environments. These limitations arise from several sources, including incomplete force modeling, un-modeled perturbations, and tracking measurement biases that are not captured in the standard covariance propagation process. This section outlines the methodology employed to generate representative uncertainties through a fitting process performed on a dataset of CDMs.

4.3.1. Covariance Model

The covariance model employed in this work is based on the simplified formulation presented in Zollo et al. (2024), which assumes diagonal positional uncertainties without velocity cross-correlations. The assumption of uncorrelated velocity uncertainties is justified by the relatively short prediction spans typically encountered in collision avoidance scenarios. This approach significantly reduces computational complexity while maintaining sufficient accuracy for collision avoidance applications.

The covariance matrix **C** for each object is constructed in the RTN reference frame, illustrated in Figure 4.2, which provides an intuitive representation of orbital uncertainties. The simplified covariance matrix is formulated as:

$$\mathbf{C}_{RTN} = \begin{bmatrix} \sigma_R^2 & 0 & 0 \\ 0 & \sigma_T^2 & 0 \\ 0 & 0 & \sigma_N^2 \end{bmatrix} \tag{4.32}$$

where σ_R, σ_T, and σ_N represent the 1-σ positional uncertainties in the radial, tangential, and normal directions, respectively.

4.3.2. Dataset

The dataset utilized in this work is provided by the European Space Agency (ESA)[1] and contains over 160,000 conjunctions representing approximately 13,000 unique events. Figure 4.15 illustrates the coverage of the dataset across different parameters, demonstrating comprehensive representation across the orbital regimes of interest to this work. The most represented orbits are near-circular with altitudes between 400 and 800 km and a spike in data density at inclinations of near 100 degrees, indicating a comprehensive representation of SSO orbits. Relatively low solar fluxes make up a majority of the dataset, and object sizes are below $5m^2$. The CDMs are well represented at different times before the TCA, up to 7 days.

[1] https://kelvins.esa.int/collision-avoidance-challenge/data/ (accessed on 14 June 2025)

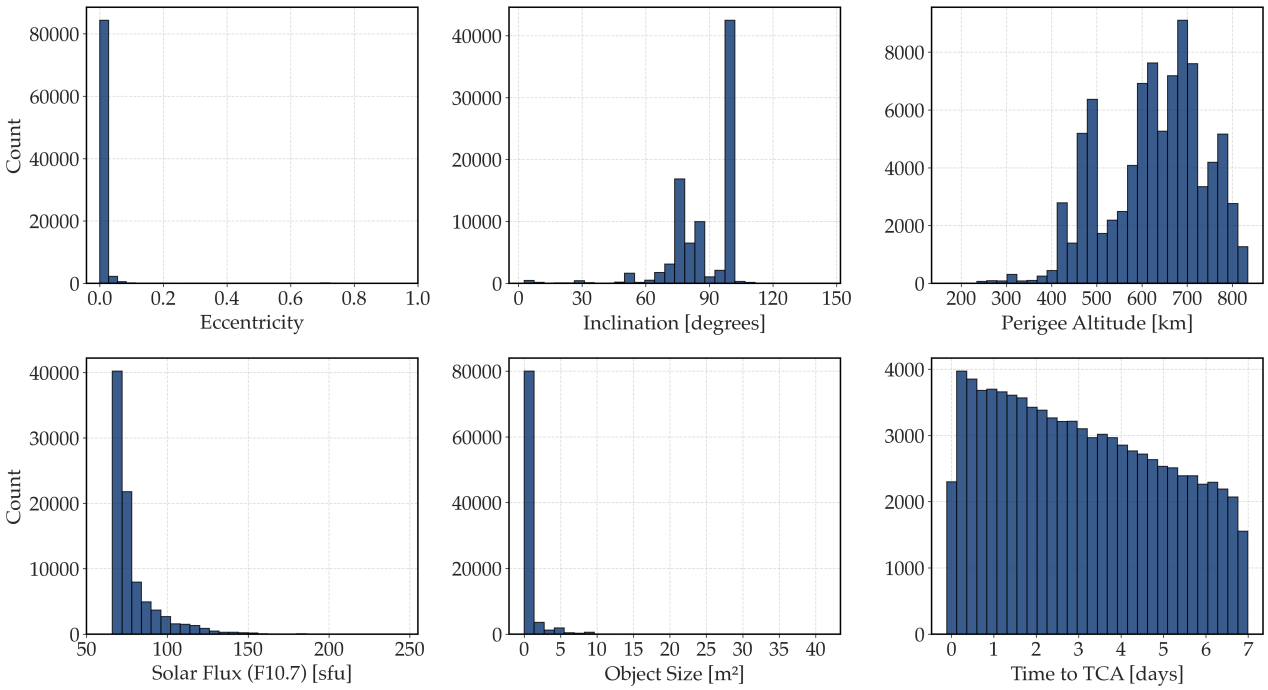

Figure 4.15: Distribution of the six fitting parameters within the dataset.

Each CDM in the dataset contains the following key information for the primary and secondary objects:

- Orbital elements
- Time to TCA (time interval between CDM generation and TCA)
- Solar weather conditions
- Relative state at TCA in RTN coordinates
- 6x6 covariance components
- Cross-sectional area

This information can be used to derive cross-correlations between different parameters to develop robust fitting methods.

4.3.3. Classification

The classification process aims to group CDMs with similar uncertainty characteristics to enable effective statistical analysis and curve-fitting. Following the methodology described in Zollo et al. (2024), the classification scheme considers five parameters that significantly influence orbital uncertainty evolution:

1. **Altitude of Perigee**: Objects at different altitudes experience varying levels of atmospheric drag and gravitational perturbations, directly affecting uncertainty growth rates.
2. **Eccentricity**: Highly eccentric orbits exhibit complex uncertainty evolution patterns due to

varying orbital velocities and altitudes.

3. **Inclination**: The inclination affects exposure to solar radiation pressure and the relative importance of various gravitational perturbations.
4. **Solar Flux Index (F10.7)**: Atmospheric density variations driven by solar activity significantly impact uncertainty evolution, particularly for objects in drag-dominant regimes.
5. **Object Cross-sectional Area-to-Mass Ratio**: This parameter influences sensitivity to both atmospheric drag and solar radiation pressure.

The classification procedure divides the parameter space into discrete bins, creating a multi-dimensional grid of orbital classes. The bin sizes are selected to ensure adequate statistical representation within each class while maintaining sufficient resolution to capture parameter dependencies. The following binning strategy is employed (Zollo et al., 2024):

Table 4.3: Dataset classification parameters (Zollo et al., 2024).

Parameter	Number of Bins	Range	Unit
Perigee Altitude (h_p)	8	[400, 1000]	km
Eccentricity (e)	6	[0, 0.2]	-
Inclination (i)	7	[0, 180]	Degrees
Solar Flux ($F10.7$)	6	[70, 250]	SFU
Size (s)	5	[0.001, 10]	m^2

Each CDM is assigned to the appropriate class based on its orbital and physical parameters. Classes with insufficient statistical representation (fewer than 10 CDMs) are merged with neighboring classes to ensure robust curve-fitting results (Zollo et al., 2024).

The covariance matrix is modelled as a function of these 5 parameters, in addition to the time between the CDM epoch and the TCA, Δt:

$$C = f(\Delta t, F10.7, s, h_p, e, i) \tag{4.33}$$

The covariance itself is not propagated in this time, it is fitted to be representative of the expected covariance at the TCA given Δt and the five other parameters.

4.3.4. Curve-Fitting

Once the CDMs are classified into appropriate orbital classes, the positional uncertainties in each RTN component are analyzed as functions of the prediction time span Δt. The curve-fitting process employs a non-linear least-squares regression, using a quadratic fit to capture the temporal evolution of orbital uncertainties, following the approach established by Zollo et al. (2024).

For each orbital class and RTN component, the uncertainty evolution is modeled using:

$$\sigma_j = a_j + b_j \Delta t + c_j (\Delta t)^2 \tag{4.34}$$

where $j \in \{R, T, N\}$ represents the RTN coordinate components, Δt is the prediction time span from the epoch of the orbital state to the TCA, and a_j, b_j, and c_j are the fitting coefficients determined through the regression.

The quadratic form is selected to capture both the linear uncertainty growth typically associated with process noise and the quadratic growth characteristic of un-modeled accelerations (Zollo et al., 2024). The physical interpretation of the coefficients is as follows:

- a_j: Initial uncertainty level, representing measurement errors and state determination accuracy
- b_j: Linear growth rate, associated with process noise and systematic biases
- c_j: Quadratic growth rate, related to un-modeled accelerations and force model uncertainties

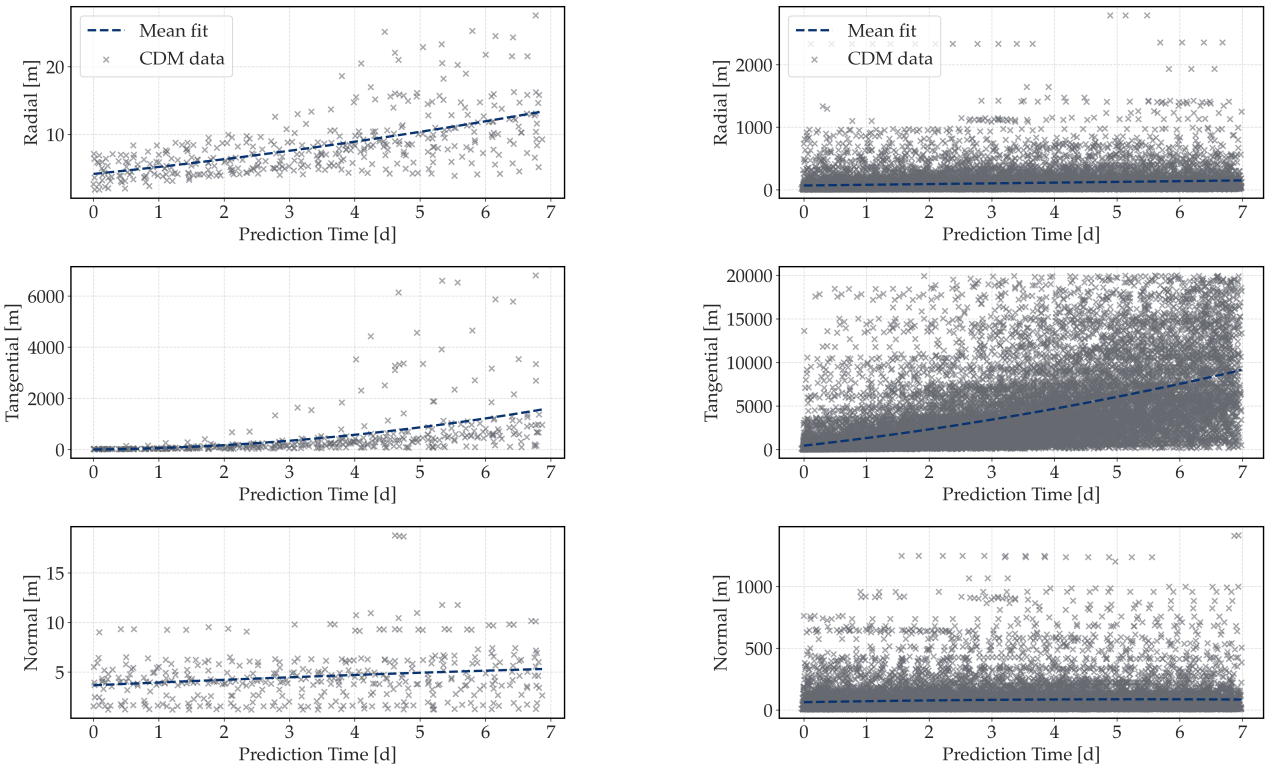

Figure 4.16: Fitting results for different propagation times for a relatively (a) sparse and (b) dense dataset.

Figure 4.16 shows the results of the fitting for two classes within the dataset, one with sparse data points and another with relatively dense data points. The vertical axis represents the 1-sigma RTN position uncertainties. The trends in uncertainty magnitude and temporal growth are clear in both classes; the tangential uncertainty is much larger than the normal and radial components, with the uncertainty increasing more with propagation time.

The quality of the curve-fitting is assessed using the root-mean-square error (RMSE) of the fit; Figure 4.17 shows the results of the implemented curve-fitting applied to the ESA dataset and a smaller

dataset of CDMs of the Delfi[2] satellites, accessed internally from TU Delft. The mean RMSE of 2540.47 meters obtained from the fitting performed on the ESA Dataset is similar to the equivalent value of 2649.15 meters obtained by Zollo et al. (2024), verifying the implementation of the fitting method and confirming the equivalent representation of position uncertainties between the ESA dataset used in this work and the GSOC (German Space Operations Centre) dataset used by Zollo et al. (2024). The larger uncertainty of 9127.53 meters obtained from the fitting performed on the Delfi dataset is likely caused by the smaller dataset of 876 CDMs of the Delfi satellites.

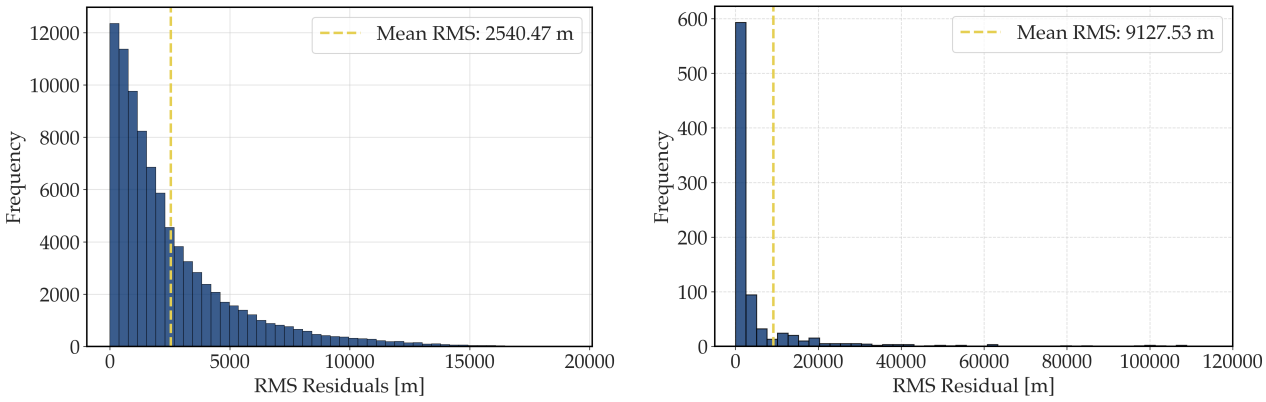

(a) (b)

Figure 4.17: 3D RMS residuals for the fitted coefficients against the (a) CDM dataset from ESA and (b) Delfi dataset.

The RMS residuals obtained by Zollo et al. (2024) are provided in Appendix A, where a comparative analysis is made with the implemented method in this work for verification purposes.

4.4. Conjunction Definition

This section explains the process used to define a conjunction between a sail and debris object at a TCA. The computation of collision risk metrics are first presented in Subsection 4.4.1, followed by the formulation of a synthetic collision-avoidance scenario in Subsection 4.4.2.

4.4.1. Collision Risk Metrics

The collision probability P_c and the Mahalanobis distance d_M are used to quantify the risk of collision between two objects. The collision probability is calculated using the 2D Foster method, according to Equation 4.35, and the Mahalanobis distance is calculated using Equation 4.37 (Foster, 2001; Hall et al., 2023). Equation 4.36 shows the Alfano method for calculating the collision probability, which uses analytical approximations resulting in a faster, but more conservative, estimate of the collision probability (Alfano & Oltrogge, 2018). The encounter plane is defined by T, which is aligned with the relative velocity vector between the two objects at TCA, and N, which is perpendicular to T and lies in the encounter plane, which is normal to the relative velocity vector.

$$P_{c_{Foster}} = \iint_D \frac{1}{2\pi\sqrt{|\mathbf{C}|}} \exp\left(-\frac{1}{2}(\mathbf{r}_c - \boldsymbol{\delta}_c)^T \mathbf{C}^{-1}(\mathbf{r}_c - \boldsymbol{\delta}_c)\right) d\mathbf{r}_c \tag{4.35}$$

[2] https://www.tudelft.nl/lr/delfi-space/delfi-program (accessed on 4 September 2025)

$$P_{c_{Alfano}} = \frac{R^2}{2\pi\sqrt{|\mathbf{C}|}} \exp\left(-\frac{1}{2}\boldsymbol{\delta}_c^T \mathbf{C}^{-1} \boldsymbol{\delta}_c\right) \tag{4.36}$$

$$d_M = \sqrt{\boldsymbol{\delta}_c^T \mathbf{C}^{-1} \boldsymbol{\delta}_c} \tag{4.37}$$

where:

- $D = \{\mathbf{r}_c = [x, y]^T : x^2 + y^2 \leq R^2\}$ is the collision disk
- $\boldsymbol{\delta}_c = [\delta_T, \delta_N]^T$ is the miss vector in the $T - N$ encounter plane
- $\mathbf{C} = \mathbf{C}^{T-N}_{\text{primary}} + \mathbf{C}^{T-N}_{\text{secondary}}$ is the combined 2×2 position covariance matrix
- $|\mathbf{C}| = \det(\mathbf{C})$ is the determinant of the covariance matrix
- $R = R_1 + R_2$ is the combined HBR
- $\mathbf{r}_c = [x, y]^T$ is the position vector in the $T - N$ encounter plane

In addition to the covariances of the primary and secondary objects, in order to compute P_c and d_M, a miss distance in RTN at TCA needs to be defined, and knowledge of the HBR of both objects is required. The inclusion of the Mahalanobis miss distance as a collision risk metric is justified due to dilution effects of the 2D collision probability method. For increasing uncertainties, the predicted collision probability initially grows, but begins to decrease after a point, leading to a false sense of safety caused by extremely large uncertainties (Modenini et al., 2022). The Mahalanobis distance is a useful metric to consider in such scenarios, as it represents an uncertainty-scaled miss distance, and thus remains small when uncertainties are large, even when large miss distances can cause diluted collision probabilities (Alfano & Oltrogge, 2018).

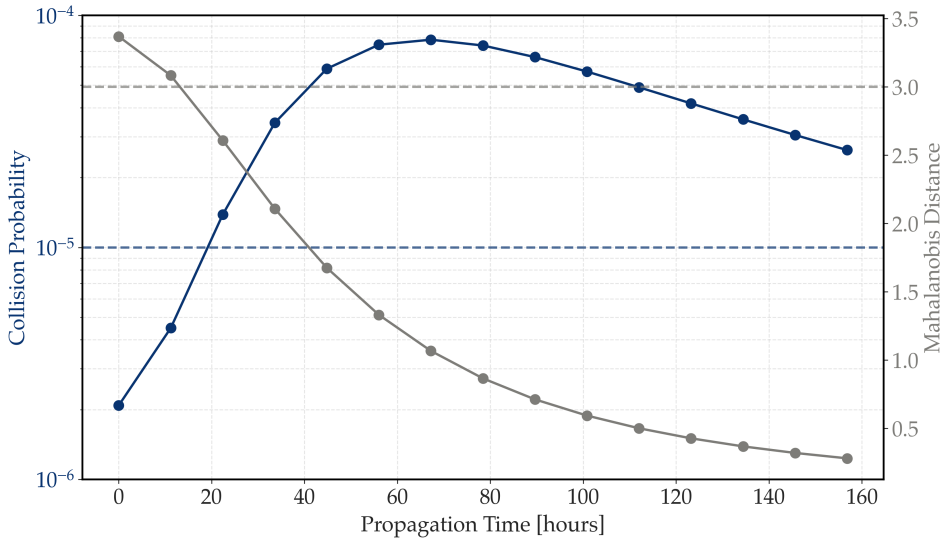

Figure 4.18: Evolution of P_c and d_M with propagation time

The dilution effect is illustrated in Figure 4.18, showing the evolution with time of the implemented 2D Foster collision probability and Mahalanobis distance. Longer propagation times correspond to increased uncertainties, and the dilution effect is clearly evident for the collision probability, as it starts to decrease after a propagation time of approximately 70 hours. While this is much longer than the expected duration of collision-avoidance maneuvers, the dilution effect may kick-in at lower propagation times in certain scenarios.

4.4.2. Collision-Avoidance Scenario Definition

Figure 4.19 shows a 3D schematic of an example conjunction scenario definition. A conjunction at some TCA is defined by the relative separation of the primary object in RTN coordinates with respect to the secondary object. The primary and secondary objects are then back-propagated from this TCA state to their initial states which are achieved after some propagation time. The specific propagation time is determined by the optimizer, discussed in section 4.5. The back-propagation represents the nominal trajectories of both objects and is performed without any control or non-conservative perturbing forces to preserve the resulting effects of the optimal control laws. From their initial states, the primary and secondary objects are forward-propagated using the eight different control laws, as defined in Section 4.2. Depending on the outcome of the controlled forward-propagation, the back- and forward-propagation may be performed multiple times to achieve a desired collision risk reduction at the TCA.

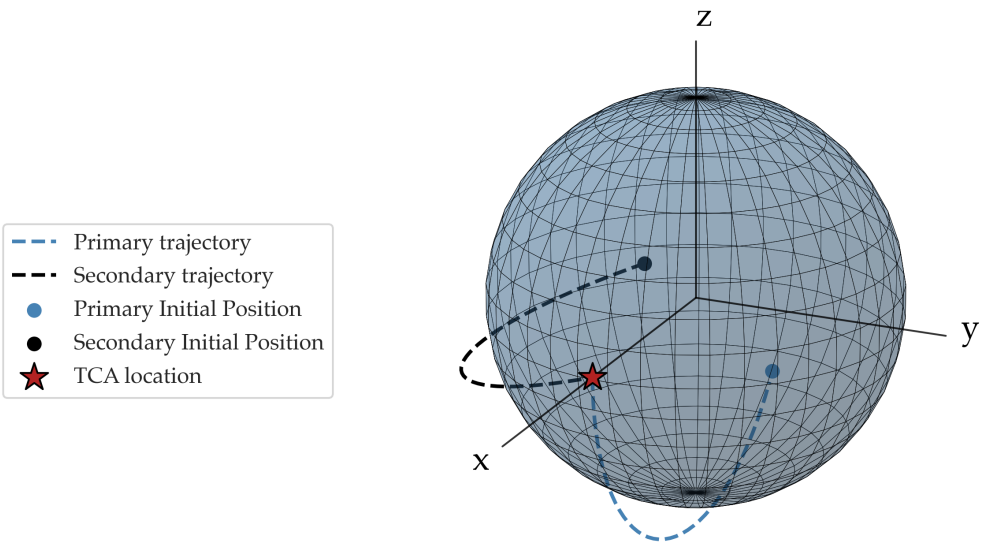

Figure 4.19: Back-propagation (nominal trajectory) to initial states from the TCA.

Figure 4.20 shows a visualization of the collision-avoidance scenario definition. The first step of running a simulation involves the definition of the orbital and physical parameters of the primary and secondary objects and their conjunction parameters at the TCA. Based on the state of the objects at an initial guess of propagation time, representative position covariance matrices at the TCA are generated using the fitted coefficients. The yellow box contains the modules used to generate the fitted covariance coefficients; this process is performed once, as the covariance coefficients are stored

in different classes and accessed as required during each iteration of the optimizer for each control law. From the states at the initial guess, the primary and secondary objects are propagated to the TCA by applying each control law to the sail. P_c and d_M are computed using the covariance uncertainties, miss distance at TCA and the combined HBR of the two objects. Based on the collision risk metrics, the optimization module determines the successive propagation time guesses to converge to an optimal maneuver duration and corresponding control law.

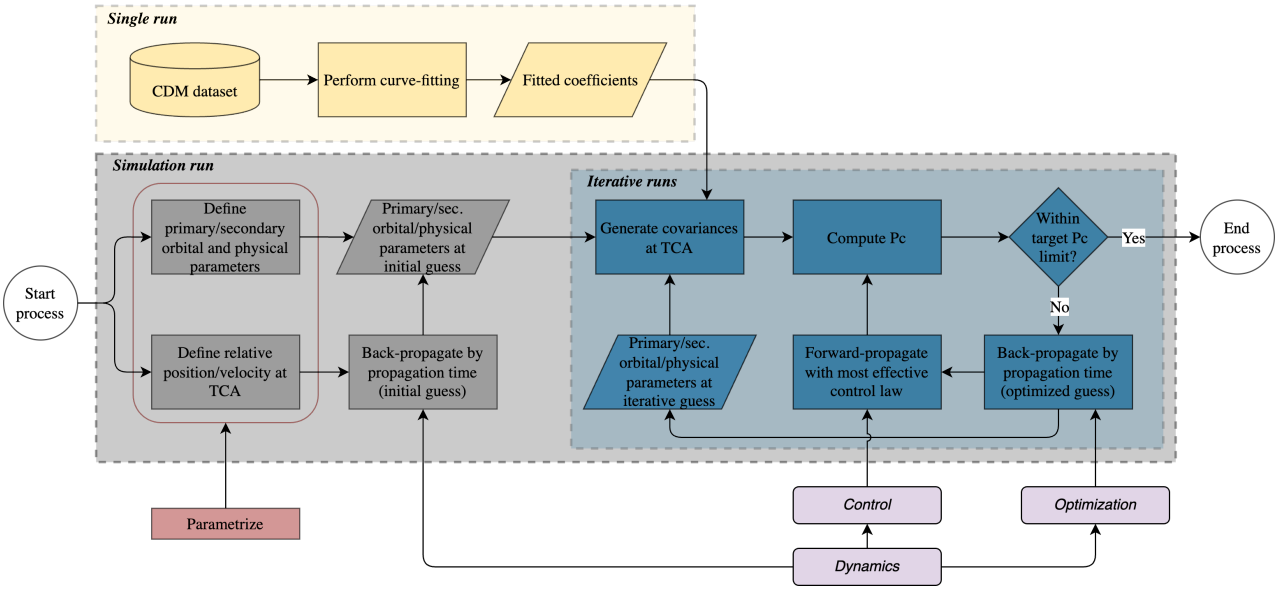

Figure 4.20: Methodology for defining the conjunction and collision-avoidance scenario.

Table 4.4 shows the main scenarios used in generating some results.

Table 4.4: Selected orbital scenarios used to generate results.

Parameter	Scenario 1/2	Scenario 3/4	Scenario 5/6
Altitude [km]	500	590	1000
Aspect angle [deg]	0/90	0/90	0/90

The SMA and RAAN are chosen as the key orbital parameters to vary as the SMA (and hence altitude) is the only orbital parameter that effects a_{drag} (given the assumptions of a geographically homogenous atmosphere, stated in Section 4.1) and the aspect angle, which can be obtained given a certain RAAN and inclination of an orbit, significantly influences a_{SRP}. The eccentricity of all initial orbits is assumed to be zero, and the inclination is set to be 90 degrees, since varying the RAAN is assumed to cover the whole range of aspect angles. All simulations are performed at vernal equinox, such that at a RAAN of 0 degrees the ascending node of the orbit points towards the Sun. Unless mentioned otherwise, all analyses are performed using a sail AMR of 5 m^2/kg, equal to that of ACS3, a miss distance of 0 meters, and a debris HBR of 1 m. Simulations were run for a true anomaly at TCA of $\theta = 0$ degrees, when the sail is in complete sunlight.

To test the extent to which the maneuvers utilized in this work are applicable to objects with lower AMRs than solar sails, the analysis is run for AMR values of typical satellites in LEO. Such maneuvers

may be particularly useful for cube-sats, that typically lack propulsion systems. Cube-sats have larger AMR values than larger satellites due to the scaling effects of area and mass with spacecraft size. A major limitation of this analysis is that the LAMR objects are still modelled as sailcraft, thus neglecting their three-dimensional shapes and assuming perfect reflectivity. It is assumed that the cubesat is modelled as a sail. While this imposes significant limitations on the analysis, it still provides a preliminary assessment of LAMR maneuvering capabilities using LOCLs.

Table 4.5 shows the ranges used for the parametric analysis. Within the range, 20 equally-spaced values are used to generate the results.

Table 4.5: Ranges used for the parametric analysis.

Parameter	Range	Unit
Altitude	[400, 2000]	km
RAAN	[0, 360]	deg
AMR	[0.01, 5]	m^2/kg
HBR	[0.1, 10]	m
TCA ΔT	[-500, 500]	m
TCA ΔN	[-50, 50]	m

4.5. Maneuver Optimization

The goal of the optimization process is to find the minimum maneuver durations required to satisfy the collision risk thresholds using the formulated analytical and numerical control laws. This section presents the optimal control problem and the implemented bisection algorithm.

4.5.1. Optimal Control Problem

The optimization problem can be formulated as:

$$\begin{aligned} \min_{\Delta t_{\text{man}}, C} \quad & \Delta t_{\text{man}} \\ \text{subject to} \quad & P_c(\Delta t_{\text{man}}, C) \leq P_c^{\text{thresh}} \\ & d_M(\Delta t_{\text{man}}, C) \geq d_M^{\text{thresh}} \\ & C \in \mathcal{C} = \{C_1, C_2, \ldots, C_8\} \end{aligned} \tag{4.38}$$

where P_c is the collision probability computed via the Foster method, d_M is the Mahalanobis distance metric, and $\mathcal{C}$ is the discrete set of available control laws.

Assumption 1 (Monotonicity of Risk Metrics)**.** *The collision risk metrics exhibit monotonic behavior with respect to maneuver duration:*

- $\frac{\partial P_c}{\partial \Delta t_{man}} < 0$ *for all feasible control laws*
- $\frac{\partial d_M}{\partial \Delta t_{man}} > 0$ *for all feasible control laws*

Most maneuver durations were found to be within the region in which the calculation of P_c is robust without suffering from the dilution effect, as discussed in Section 4.4.

Assumption 2 (Feasibility Guarantee)**.** *There exists at least one control law $C^* \in \mathcal{C}$ and duration*

$\Delta t^*_{man} \in [0, \infty]$ *such that both collision risk criteria are satisfied.*

The maneuver is assumed to start at the initial time, defined by the back-propagation, up to the TCA, such that control law under consideration is in continuous use throughout the maneuver duration.

4.5.2. Bisection Method

To find the minimum maneuver time required to satisfy the collision risk thresholds using a subset of LOCLs, a bisection optimization method is chosen due to its straightforward implementation process, and was found to converge in a small number of iterations. However, the proposed bisection method assumes the monotonic properties established in Assumption 1 to search for the minimal feasible maneuver duration. In scenarios where this assumption breaks down, optimal maneuver durations may not be found, but these scenarios were not encountered in the analyses performed in this work. Scenarios in which Assumption 1 breaks down are likely to be encountered when only a single control law is utilized in the optimization framework, making certain combinations of conjunction separation and control law usage lead to a growth in collision risk for increasing maneuver durations. The usage of multiple control laws limits these scenarios as the optimizer always picks the best one, even if others do not converge.

The algorithmic flow of the bisection optimization algorithm is illustrated in Algorithm 1. The values of t_{min} and t_{max} are defined by an initial bound-finding algorithm, to avoid the need to define and constrain the maximum or minimum maneuver duration. Based on an initial guess of t_{man}, the bound-finding algorithm repeatedly doubles or halves the maneuver duration until the upper or lower bounds are found, after which the bisection algorithm is implemented for convergence. This ensures that extremities are not excluded, and large ranges need not be defined by default. During each iteration of the algorithm, each control law in the subset is evaluated based on its risk-reduction effect. If one or more control laws satisfy the collision risk thresholds, t_{man} is reduced to find the minimum time, t^*_{man}, and if no control laws satisfy the thresholds, t_{man} is increased until at least one suitable control law is found. Cases where multiple control laws yield the same minimum maneuver time did occur between maximization/minimization control pairs, and were dealt with by choosing the maximization variant in such scenarios. The convergence results of the implemented algorithm are shown in Section 5.2.

The total computational cost of the bisection method comprises:

- Number of bisection iterations
- Control law evaluations per iteration
- Propagation cost per evaluation

As the number of control laws evaluated is fixed and the propagation time is a free variable chosen by the optimizer, an appropriate maximum limit needs to be set for the number of iterations to limit computational times.

Algorithm 1 Bisection Method for Optimal Maneuver Duration

Require: Initial interval $[t_{\min}, t_{\max}]$, thresholds P_c^{thresh}, d_M^{thresh}, tolerance ϵ, control law set C
Ensure: Optimal maneuver duration Δt_{man}^* and control law C^*

procedure BisectionOptimizer($t_{\min}, t_{\max}, P_c^{\text{thresh}}, d_M^{\text{thresh}}, \epsilon$)
  while $(t_{\max} - t_{\min}) > \epsilon$ **do**
    $t_{\text{mid}} \leftarrow (t_{\min} + t_{\max})/2$
    for all control law $C_i \in C$ **do**
      $(P_c^i, d_M^i) \leftarrow$ SimulateManeuver(t_{mid}, C_i)
      if $P_c^i \leq P_c^{\text{thresh}}$ **and** $d_M^i \geq d_M^{\text{thresh}}$ **then**
        feasible $\leftarrow$ TRUE
        if $P_c^i < P_c^{\text{best}}$ **then**
          $P_c^{\text{best}} \leftarrow P_c^i$
          $d_M^{\text{best}} \leftarrow d_M^i$
          $C^{\text{best}} \leftarrow C_i$
        end if
      end if
    end for
    if feasible = TRUE **then**
      $t_{\max} \leftarrow t_{\text{mid}}$ ▷ Explore shorter durations
      $\Delta t_{\text{man}}^* \leftarrow t_{\text{mid}}$
      $C^* \leftarrow C^{\text{best}}$
    else
      $t_{\min} \leftarrow t_{\text{mid}}$ ▷ Require longer duration
    end if
  end while
  return $\Delta t_{\text{man}}^*, C^*$
end procedure

Table 4.6 shows the parameters used for the bisection algorithm implementation, which were chosen to balance computational efficiency and maneuver duration resolution during the simulations.

Table 4.6: Values used for the implementation of the bisection algorithm during each optimization run

Parameter	Value
Convergence time tolerance [s]	60
Maximum iterations	20
Initial guess [s]	1200
P_c^{thresh}	10^{-5}
d_M^{thresh}	3

The time tolerance determines the resolution of the optimal maneuver duration obtained using the bisection method. A value of 60 seconds is chosen for the tolerance, as maneuver durations were found to largely lie in the range of several minutes to hours. A 60 seconds tolerance was

considered sufficient to differentiate between the simulated scenarios while limiting the number of iterations. A maximum number of iterations of 20 is chosen, but this limit was never reached during the simulations.

The values chosen for P_c^{thresh} and d_M^{thresh} are common values used in literature and during operational CAM design (Lewis & Skelton, 2024; Modenini et al., 2022). The initial guess is kept fixed for all analysis scenarios, even though maneuver duration results were observed to differ significantly for different simulation scenarios; the upper bound of the majority of maneuver durations was found to be under two hours, such that even a two-hour optimal maneuver would require a bound-finding search of only three additional iterations before beginning to converge.

5 Results

This chapter presents the relevant results obtained using the methodologies described in the previous chapter. The effectiveness of the utilized control laws is first presented in Section 5.1, followed by a discussion of the resulting optimal maneuver durations, in Section 5.2. The chapter concludes with the discussion of results from a parametric study in Section 5.3.

5.1. Control Law Effectiveness

This section discusses the relative effectiveness of each of the control laws considered in this work in an effort to determine relations between the use of particular control laws in specific conjunction scenarios.

While eight LOCLs were formulated in Section 4.2 (for the maximization/minimization of the four orbital elements), initial simulations showed similarities between the usage and performance of a and e control laws, and Ω and i control laws, respectively. As provided in Section 4.2, a and e control laws both contain only in-plane primer vector components, with the e control law containing a larger radial component. The a control law consistently performed better; this is likely because one of the most effective ways of reducing collision risk is by increasing tangential separation via a change in orbital period, which is best achieved by the a control law. The Ω and i control laws contain the same primer vector components, with the only difference being the points within an orbit at which the direction switches. This switching can be compensated by either control law by choosing the maximization or minimization variants of the control law. The Ω control law is chosen in this analysis. Therefore, the e and i control laws are omitted in the analysis hereafter.

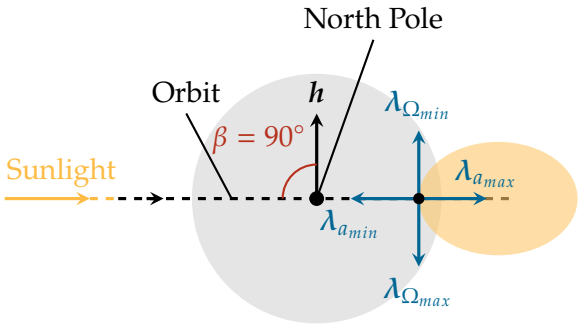

Figure 5.1: Primer vectors for four control laws in relation to the SRP acceleration envelope for an orbit with an aspect angle of $\beta = 90°$at a RAAN of $\Omega = 0°$ at vernal equinox.

Figures 5.1, 5.2 and 5.3 show schematics of three orbital scenarios to aid the interpretation of the results presented hereafter. In each scenario, the four primer vectors are provided with respect to

the SRP acceleration envelope along a polar orbit as seen from above the Earth's North Pole. The orbits are represented by the black dashed line, with the sail represented by the black dot along the orbit at the origin of each primer vector. Figure 5.1 shows a scenario with an aspect angle of $\beta = 90$ deg (corresponding to $\Omega = 0$ deg at vernal equinox), showing that $\lambda_{a_{max}}$ is most coincident with the SRP acceleration envelope. As the sail crosses the descending node and moves towards the ascending node, $\lambda_{a_{min}}$ will become coincident with respect to the SRP acceleration envelope, which remains fixed in size and orientation with respect to the sunlight vector. Figure 5.2 shows a scenario with an aspect angle of $\beta = 0$ deg (corresponding to $\Omega = 90$ deg at vernal equinox), showing that $\lambda_{\Omega_{max}}$ is most coincident with the SRP acceleration envelope; Figure 5.3 is also shown for an aspect angle of $\beta = 0$ deg but for a RAAN of $\Omega = 270$ deg, such that $\lambda_{\Omega_{min}}$ becomes most coincident with the SRP acceleration envelope. The coincidence of each primer vector relative to the SRP acceleration envelope drives the selection of certain control laws in different scenarios in the results presented in this chapter.

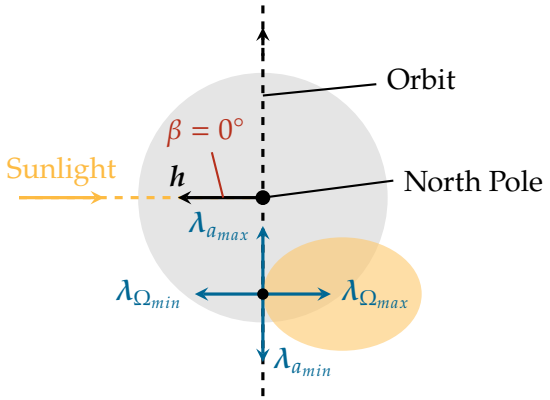

Figure 5.2: Primer vectors for the four control laws in relation to the SRP acceleration envelope for a polar orbit with an aspect angle of $\beta = 0°$ at a RAAN of $\Omega = 90°$ at vernal equinox.

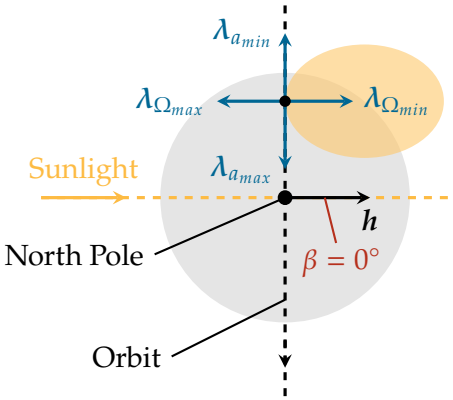

Figure 5.3: Primer vectors for the four control laws in relation to the SRP acceleration envelope for an orbit with an aspect angle of $\beta = 0°$ at a RAAN of $\Omega = 270°$ at vernal equinox.

Figure 5.4 shows the effect of each considered control law on the P_c, d_M and miss distance d at the TCA for orbital scenario 5; Figure 5.4a and 5.4b are for a Δt equal to half an orbit and one orbit, respectively. For a propagation of half an orbit, Ω_{max} is most effective in reducing collision risk, even though its miss distance at the TCA is smaller than the $a_{max/min}$ control laws. Ω_{min} is ineffective because for $\beta = 0$ deg, the Ω_{min} primer vector does have any coincidence with the SRP bubble during the simulated orbital arc. However, due to the switching nature of the Ω control laws at the ascending/descending nodes (Equation 4.20), a propagation over a full orbit leads to Ω_{min} also becoming effective, since the Ω_{min} primer vector switches to coincide with the SRP bubble. This effect is also noticed in the convergence of the optimization scheme in Section 5.2, where it is further explained. For a full orbit, the a control laws become more effective in reducing collision risk. Figure 5.4a shows that larger miss distances do not always correspond to larger reductions in collision risk; this is because the covariance ellipsoid is not symmetrical in the RTN reference frame, with uncertainties typically much larger along the tangential axis than the normal or radial axes, as seen in Section 4.3. Therefore, while a control laws are effective in increasing tangential separation, they require larger separations to

escape the elongated ellipsoid in comparison to Ω control laws, which require smaller separations.

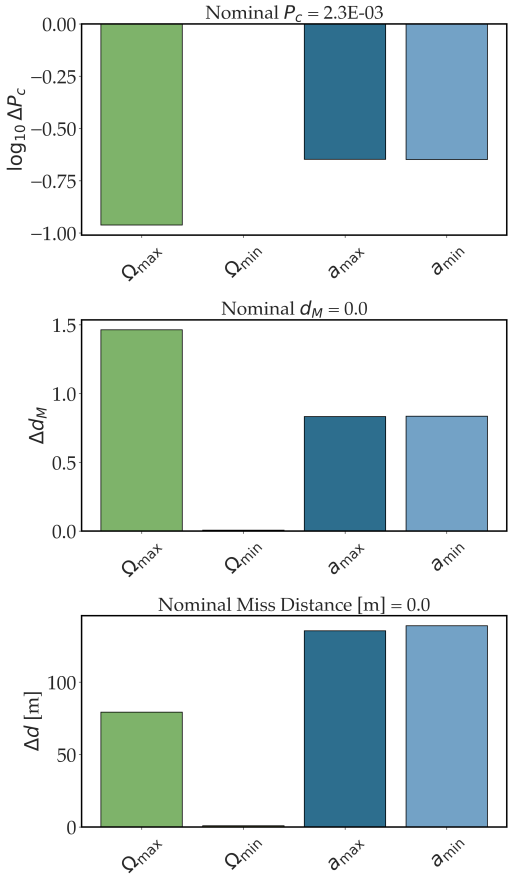

(a) h_{alt} = 1000 km, β = 0 degrees, Δt = 1/2 orbital period

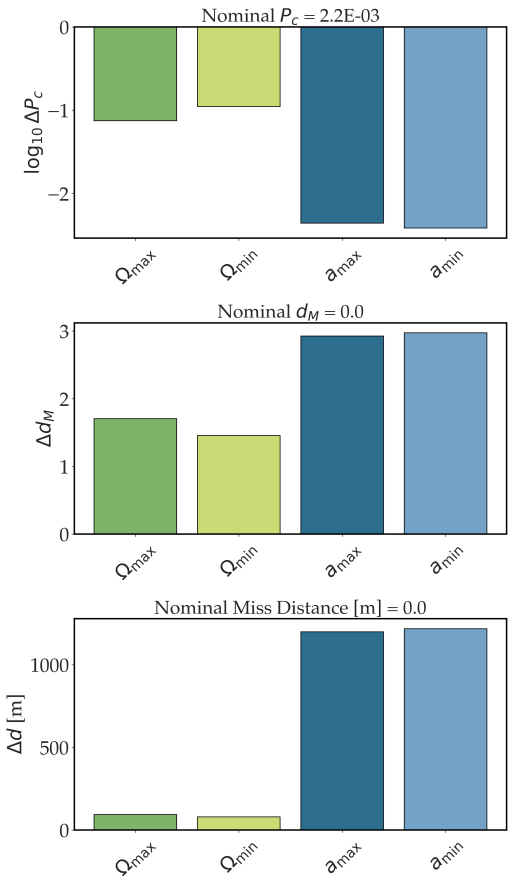

(b) h_{alt} = 1000 km, β = 0 degrees, Δt = 1 orbital period

Figure 5.4: Relative effects of each control law on the collision risks and miss distance for scenario 5.

These trends align with those presented in Gonzalo et al. (2021b) and Dominguez-Gonzalez et al. (2013). According to Dominguez-Gonzalez et al. (2013), short-term maneuvers involve a ΔV applied normal to the flight direction, and long-term maneuvers involve an along-track impulse a certain number of orbits before TCA. Gonzalo et al. (2021b) compares CAM strategies with minimum collision probability and maximum separation objectives, and concludes that for both objectives, the optimum ΔV tends to align with the tangential direction for lead times greater than half an orbital period. CAMs with a minimum collision-probability objective lead to faster variations in the encounter plane, as they tend to move away from the principle axis of the covariance. This typically results in a smaller separation when compared to maximum-separation maneuvers. These conclusions align with astrodynamics principles; a ΔV in the along-track direction changes the SMA and orbital period, which leads to a quadratic drift in the relative along-track position (Ghrist & Plakalovic, 2012). Since a cross-track deviation scales linearly with a change in RAAN, it is expected that along-track deviations become increasingly effective for an increasing number of orbits before TCA.

Figure 5.4 also highlights that in scenario 5, a_{max} and a_{min} have very similar effects on all three metrics. Given that drag is negligible at 1000 km, the resultant acceleration, a_{SRP}, has equal components along

$\boldsymbol{\lambda}_{a_{max}}$ and $\boldsymbol{\lambda}_{a_{min}}$; these two vectors are opposite and collinear and are aligned with the orbit's tangent, such that at an aspect angle of $\beta = 0$ deg, the optimal cone angles for $\boldsymbol{\lambda}_{a_{max}}$ and $\boldsymbol{\lambda}_{a_{min}}$ are equal.

Figure 5.5 shows the evolution of the tangential separation, ΔT, and the normal separation, ΔN, for different maneuver durations before the TCA. The along-track separation growth increases quadratically with propagation time before the TCA, while the cross-track separation growth is linear, in agreement with Gonzalo et al. (2021b). Note the large difference in the separation values between both axes; the tangential separation is much larger, but that does not necessarily lead to proportionally larger reductions in collision risk, as discussed previously. This indicates an expected pattern in control law usage, with SMA control laws being more effective for longer maneuvers and RAAN control laws being more effective for shorter durations. This effect may, however, be influenced by additional parameters such as the aspect angle or conjunction miss geometry.

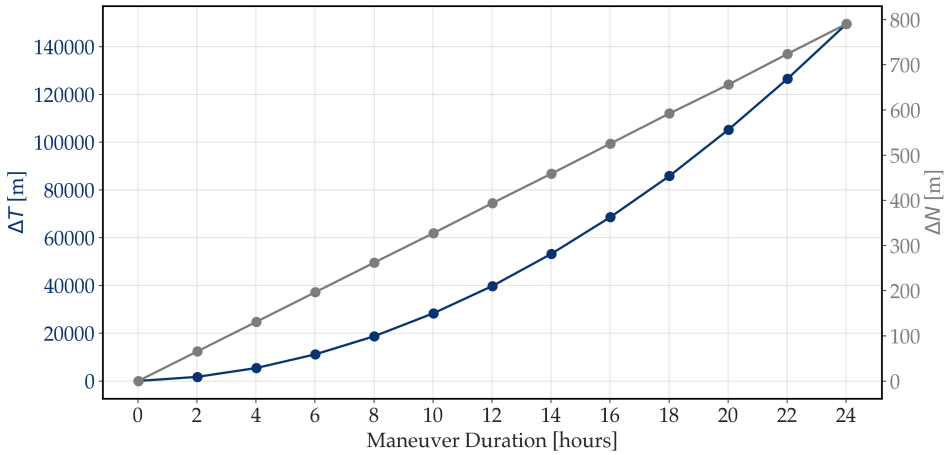

Figure 5.5: Evolution of (ΔT) and (ΔN) with maneuver duration using a_{max} and Ω_{max}, respectively.

5.2. Optimal Maneuver Durations

This section presents the result of the bisection optimization for scenarios 1 and 5, showing the convergence of the maneuver times and the evolution of the risk metrics over iterations. Scenarios 1 and 5 are shown because they produce interesting phenomena that result from the aspect angle of 0 degrees and altitudes of 500 and 1000 km, respectively. Given the relative significance of the SRP force and drag at these two different altitudes, a comparison is made between the use of SRP-only control for scenario 5 and SRP+drag control for scenario 1.

Figures 5.6 and 5.7 show the convergence of the optimizer and the corresponding evolution of collision risk over each iteration for the control laws. The yellow lines represent the initial bound-finding phase of the optimizer, starting with the initial guess of 1200 seconds (0.33 hours in the figures), while the blue lines represent the bisection algorithm over iterations until convergence. Figure 5.6 shows the results of the SRP-only control law for scenario 5; the Ω_{max} control law is most effective, while the Ω_{min} control law is noticeably ineffective in changing the collision risk. This is because it is impossible to achieve an SRP acceleration component along $\boldsymbol{\lambda}_{\Omega_{min}}$, which, in this scenario, points towards the Sun and therefore has no coincidence with the SRP acceleration envelope, as explained

in Section 5.1 and depicted in Figure 5.2. The a_{max} and a_{min} control laws are both equally effective, but less effective than Ω_{max}; this is in agreement with the observation in Figure 5.4a in Section 5.1.

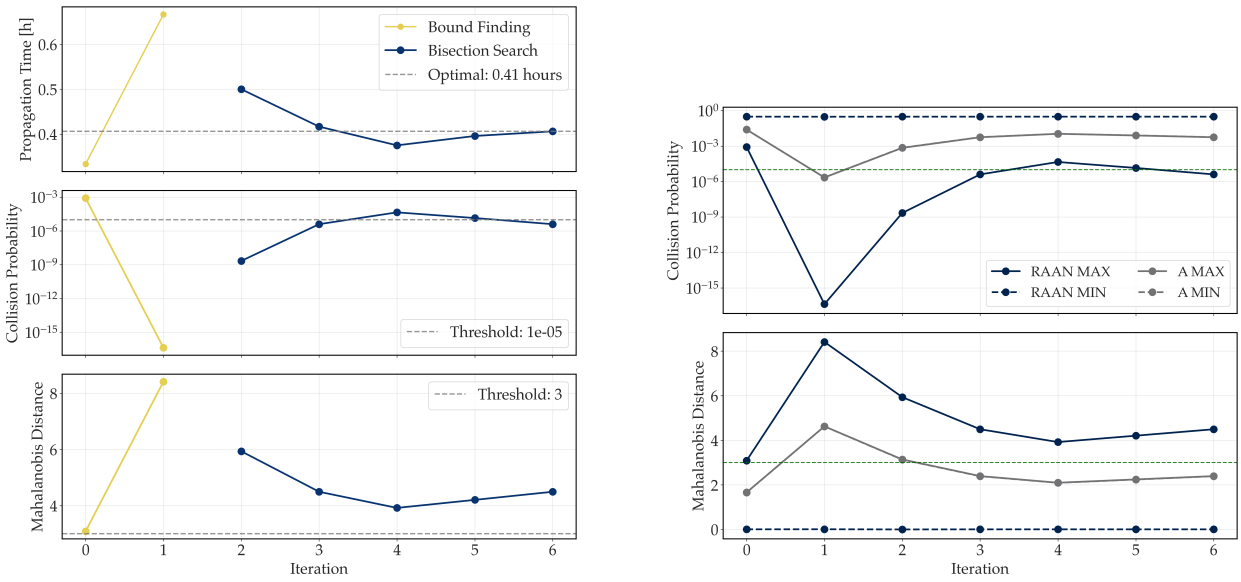

Figure 5.6: Collision risk and propagation time evolution for SRP-only control at a 1000 km altitude and 0 degree aspect angle.

Figure 5.7 shows the convergence of the optimizer for scenario 1 using the SRP+drag control law. The observed similarity between the a_{min} and Ω_{min} control laws can be explained by the geometry of the orbit's aspect angle and the nature of the two control laws. At an aspect angle of 0 deg, as depicted in Figure 5.2, $\lambda_{\Omega_{min}}$ points out-of-plane towards the sun, and hence lies outside the SRP acceleration envelope; the closest the Ω_{min} control law can get to pointing within the SRP acceleration envelope is by pointing the sail normal along the orbit's tangential direction, effectively becoming edge-on with respect to the sunlight direction.

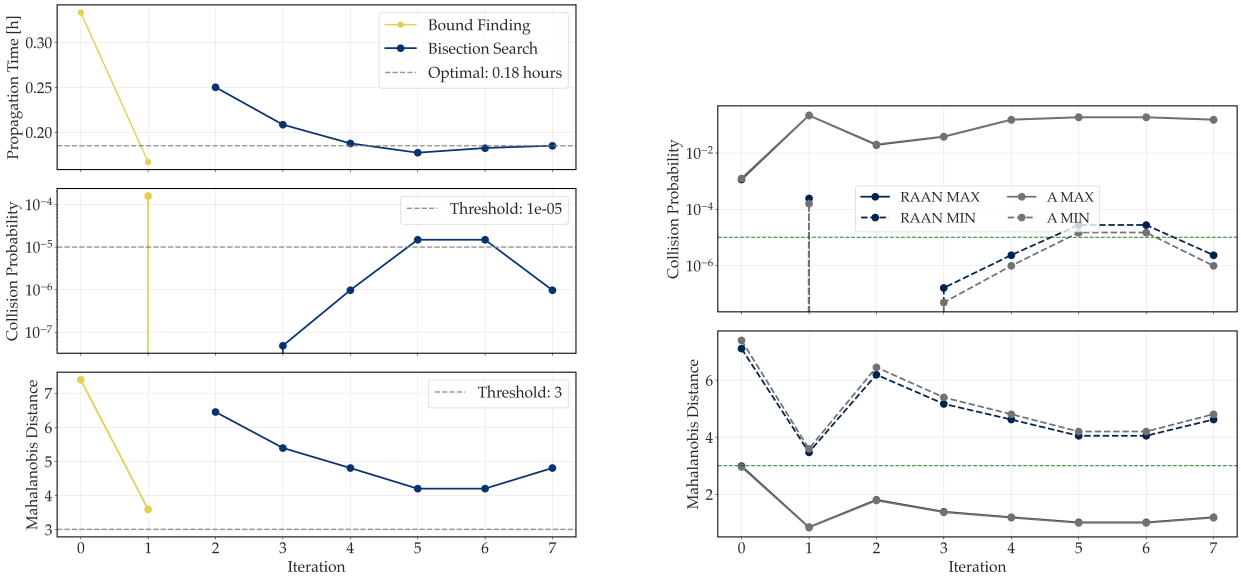

Figure 5.7: Collision risk and propagation time evolution for SRP+drag control at a 500 km altitude and 0 degree aspect angle.

Figures 5.8 and 5.9 show schematics of scenario 1 with representations of the sail orientations resulting from the use of a_{min} and Ω_{min} control laws at key points in the orbit; Figure 5.8 shows the scenario as seen with the sunlight vector pointed into the page and Figure 5.9 shows the scenario as seen from above the North Pole. At a true anomaly of $\theta = 90$ degrees, the orientation attained via the Ω_{min} control law coincides with that attained by the a_{min} control law, which, at an altitude of 500 km, is effectively face-on with respect to the velocity vector for maximum drag. While this explains the similarity in behaviour of the two control laws, the small discrepancy between the behaviour of a_{min} and Ω_{min} observed in Figure 5.7 can be explained by the different orientations attained by the two control laws as the sail moves away from a true anomaly of $\theta = 90$ degrees towards the equator. Figure 5.9 shows how the orientation of the a_{min} control law remains face-on with respect to the velocity vector, while the Ω_{min} control law only maintains its edge-on orientation with respect to the Sun-line, without rotating to remain face-on with respect to the velocity vector. The optimizer in Figure 5.7 converges to an optimal maneuver duration of 0.18 hours, shorter than the 0.41 hours for scenario 5 in Figure 5.6; this is due to the significant effect of drag which results in more effective separations in the encounter plane.

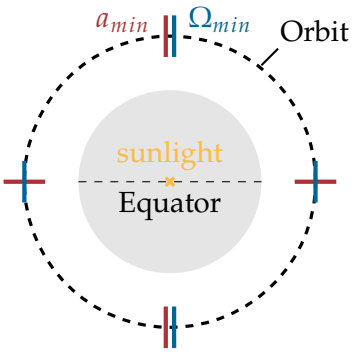

Figure 5.8: Schematic of a sail's orientation at true anomalies of $\theta = 0$, 90, 180, and 270 degrees, using the a_{min} and Ω_{min} control laws during a polar orbit with an aspect angle of $\beta = 0$. The Sun-Earth line is pointed into the page.

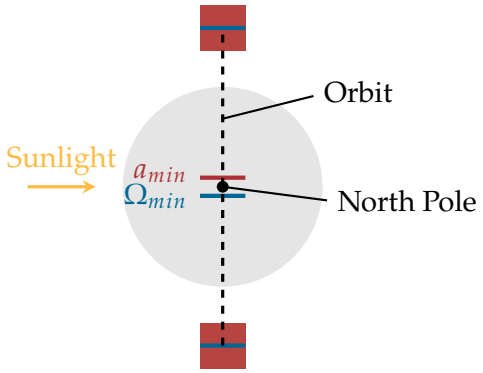

Figure 5.9: Schematic of a sail's orientation at true anomalies of $\theta = 0$, 90, and 180 degrees, using the a_{min} and Ω_{min} control laws during a polar orbit with an aspect angle of $\beta = 0$.

The relative frequency of the usage of control laws across different altitudes and RAANs is presented in Figure 5.10, which is provided for simulations performed across ranges presented in Table 4.5 in Section 4.4. There is a clear tendency for the usage of a_{min} at altitudes below 500 km, where the atmospheric density makes face-on orientations for maximum SMA decrease most effective. The a_{max} control law is mostly used at higher altitudes for RAANs close to zero, corresponding to an aspect angle of 90 degrees, when the sunlight direction is most aligned with the SMA maximization primer vector. The Ω_{max} control law is utilized across several combinations of altitude and RAAN, with a tendency to be the most chosen at RAANs close to 90 degrees, corresponding to an aspect angle of 0 degrees; this is when the sunlight direction is most aligned with the RAAN maximization primer vector. The relatively low usage of the RAAN minimization control law is merely a result of the simulated scenarios; an analysis of RAANs between 0 and -90 degrees, instead, would lead to a switch in distribution between the RAAN maximization and minimization control laws. For RAANs between 0 and 90 degrees, the RAAN minimization primer vector is mostly not contained within the

SRP acceleration envelope, resulting in the relatively small observed frequency in the usage of Ω_{min}, as observed and explained in Section 5.1.

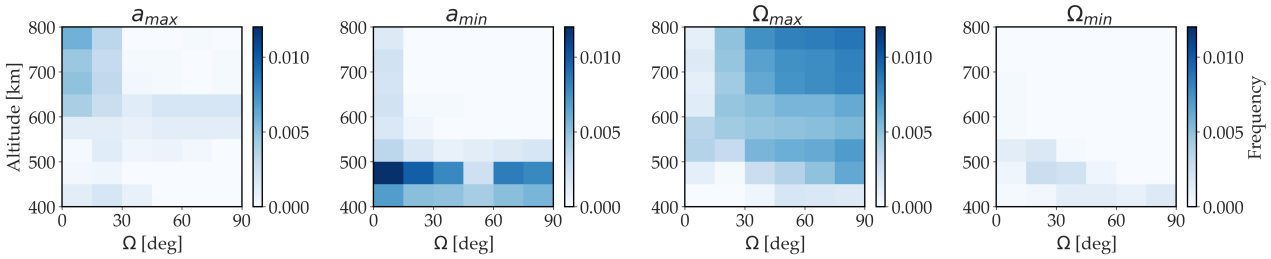

Figure 5.10: Frequency of control law usage across altitudes and RAANs

While the usage of the SMA minimization control laws are very effective, they essentially insert the sail into a lower orbit, potentially leading to a greater likelihood of de-orbit due to increased atmospheric density. To analyze the capability of a sail to "escape" such altitudes, the effectiveness of the a_{max} control law is assessed for the ACS3 solar sail at different initial altitudes and for different fixed maneuver durations. The goal is to assess the altitudes at which the sail can achieve positive changes in SMA that allow it to escape very low altitudes and recover to nominal mission orbits following a CAM. The following plots show this capability for ACS3 using SRP-only and SRP+drag control laws.

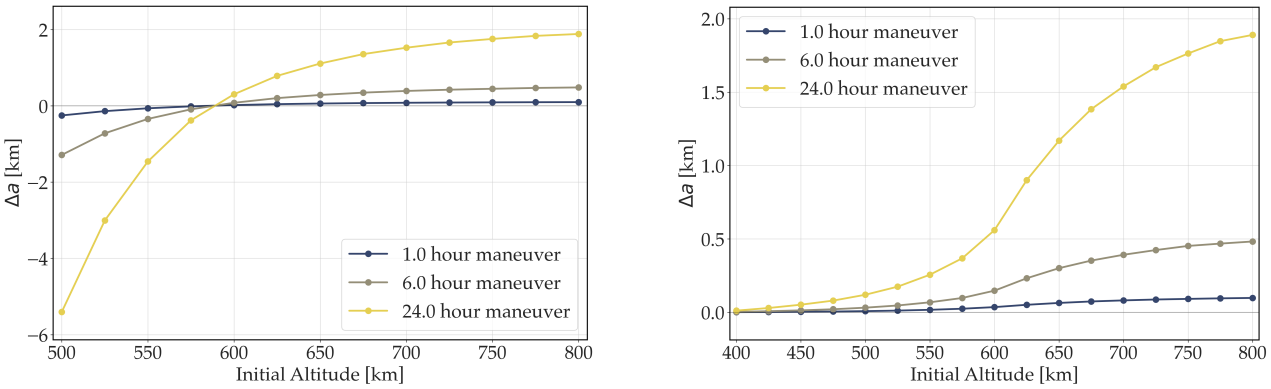

(a) SRP-only control

(b) SRP+drag control

Figure 5.11: Effectiveness of a_{max} control for different durations and initial altitudes.

Figure 5.11a indicates that the SRP-only control law is unusable at altitudes below approximately 590 km, where drag becomes too large. Figure 4.5a shows that at a nominal solar flux, the drag at an altitude of 600 km is over 5 times larger than the SRP force, which explains the ineffectiveness of the SRP-only a_{max} control law. The a_{max} control law is noticeably more effective when using SRP+drag control. At very low altitudes dominated by drag, the SRP+drag control law orients the sail edge-wise with respect to the velocity vector, thus effectively eliminating any decrease in SMA due to drag; however, this is also not effective in harnessing SRP to increase SMA, resulting in small increases in SMA between altitudes of 400 and 500 km. Theoretically, a sail can maintain its SMA at any altitude by remaining perfectly edge-on with respect to the velocity, but this is not operationally

possible given that a real sail will still have a non-zero cross-sectional area at this orientation. Longer maneuvers will result in more favourable SMA increases for both scenarios, but this was not analyzed due to computational limits and a lack of relevance to the focus of this work. Above altitudes of approximately 650 km, both control laws have a similar orbit-raising effect, which is expected given that the SRP+drag control law tends towards the SRP-only control law at higher altitudes as the SRP force becomes increasingly dominant over drag.

5.3. Parametric Analysis

This section discusses the results of parametric studies conducted to determine the effect of varying orbital, physical and conjunction parameters on the maneuver durations and control law usage.

5.3.1. The Effect of Physical Parameters

The physical parameters of the sail and debris were analyzed using two sets of variables: the sail's AMR and the sail's and debris' HBR at TCA. The former affects the control authority through its direct proportionality with the SRP and drag accelerations, while the latter represents the effective object radius at the TCA and is only used in the collision probability calculation, without having any effect on the control authority.

While this work is focused on assessing the collision avoidance performance of solar sails, it is interesting to also assess how these type of control laws perform for LAMR objects. Figure 5.12 shows the distribution of maneuver durations for AMR values of 0.01 to 0.1 m^2/kg and altitudes of 400 to 600 km. The altitude range was chosen such that the combined control law is effective, while the AMR range was chosen to include typical LAMR values (ESA, 2024). The simulation is performed for orbits with an aspect angle of $\beta = 0$ to prevent eclipses from affecting the results; the maneuver duration variations are therefore purely an effect of AMR and altitude.

As seen in Figure 5.12, there is a clear correlation between the maneuver duration and the ranges of altitudes and AMRs analyzed, with LAMR objects at high altitudes requiring the most time to maneuver away from a predicted collision, and HAMR objects at low altitudes being most effective due to the larger combined effects of SRP and drag. Given the relative insignificance of the SRP force relative to drag at altitudes close to 400 km, the objects can effectively be considered drag sails, thus indicating that drag sails with AMRs over 0.05 at altitudes below 425 km are capable of performing CAMs in approximately one hour. Only a_{max} and a_{min} control laws are used in this scenario, which follows from the analysis in Section 5.1, showing that SMA control laws become more effective over longer maneuver durations. Given the dominance of drag at the analyzed altitude range, a_{min} is used most frequently, with a switch to a_{max} at higher altitudes where SRP becomes significant enough to produce positive tangential accelerations that exceed the negative tangential accelerations produced by a_{min}. This switch happens at lower altitudes for lower AMR objects, which is unexpected given that the SRP force and drag scale equally with AMR; while the reason for this behaviour is unclear, it is hypothesized that since smaller AMRs cause longer maneuver durations, during the maneuver the aspect angle changes as the Earth revolves around the Sun to cause a sufficient increase in coincidence between the SRP acceleration envelope and $\boldsymbol{\lambda}_{a_{max}}$. This effect is shown in Figure 5.13 for an exaggerated aspect angle of $\beta = 20$ degrees.

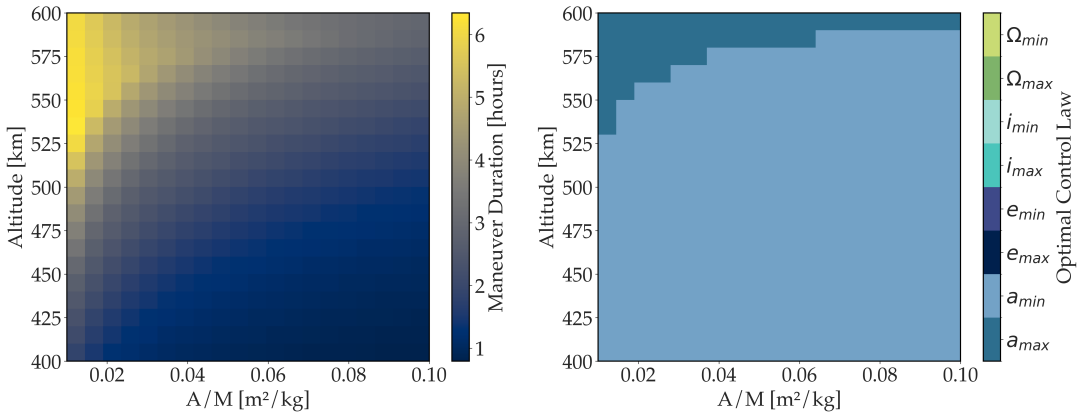

Figure 5.12: The effect of AMR and altitude on maneuver duration, simulated for a polar orbit with an aspect angle of 0 degrees using the SRP+drag control law (left) and the corresponding optimal control laws used for each scenario (right)

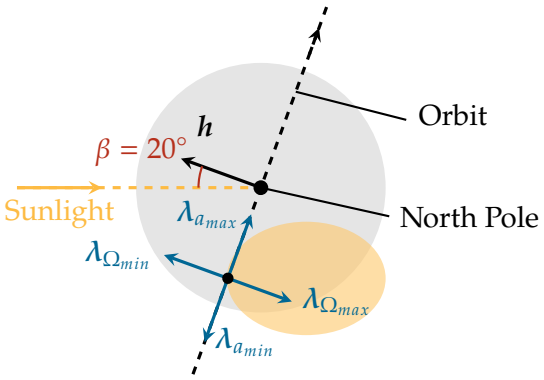

Figure 5.13: Schematic of the primer vectors for four control laws in relation to the SRP acceleration envelope for a polar orbit with an aspect angle of $\beta = 20°$ at a RAAN of $\Omega = 90°$ some duration after the vernal equinox.

An important consideration during the analysis is the effective cross-sectional area of the sail at the TCA. Since the collision probability is computed using an integration of the combined HBR of the sail and debris over the combined covariance ellipsoid, the collision risk can be reduced by orienting the sail edge-wise with respect to the conjunction plane just before the TCA; this would significantly reduce the combined HBR, and potentially reduce the required maneuver duration for a sufficient reduction in collision risk. To assess the affect of such an attitude change right before the TCA, a range of the sail's HBR at TCA is plotted against the secondary object's HBR, as shown in Figure 5.14, for scenario 5 and a fixed AMR of 5 m^2/kg. Figure 5.14a is shown for a miss distance of zero meters and Figure 5.14b is shown for a miss distance in the T-N plane of $\Delta T = 50$ m, $\Delta N = 10$ m. In both cases, the Ω_{max} control law was found to be most optimal across the entire range of simulated values.

For a miss distance of zero meters, maneuver durations reduce by approximately 20% when the sail is near edge-on relative to the conjunction plane (a minimum value of HBR = 0.1 m was used to simulate near edge-on cross-sectional areas, as an HBR of 0 m would lead to a trivial solution) compared to when it is near face-on (HBR values near 10 m). While 20% is a seemingly modest reduction in maneuver duration for such a significant reduction in effective sail HBR, collision probabilities are still significant given the miss-distance of zero meters; this means the combined HBR is located

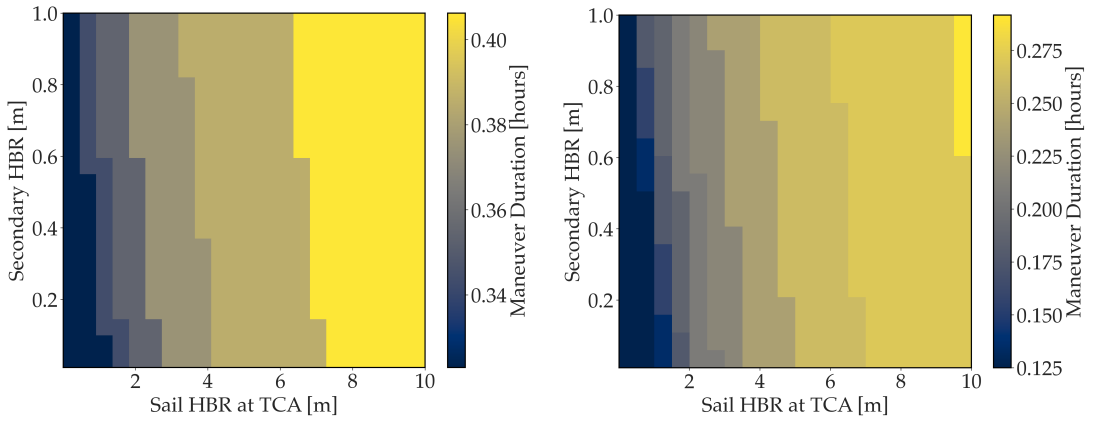

(a) $\Delta T = 0$ m, $\Delta N = 0$ m

(b) $\Delta T = 50$ m, $\Delta N = 10$ m

Figure 5.14: The effect of HBR of the primary and secondary objects on manuever duration for ACS3 and a conjunction separation in the *T-N* plane.

at the center of the error ellipsoid in the largest uncertainty region, leading to still non-negligible collision probabilities and hence modest decreases in maneuver duration. To isolate this phenomenon, the same HBR values were simulated for a non-zero miss distance in the *T-N* plane; as expected, the reduction in maneuver duration from near face-on to near edge-on orientations relative to the conjunction plane increases to approximately 55%, as a reduced HBR combined with a non-zero miss distance is more effective in reducing collision probabilities.

5.3.2. The Effect of Orbital Parameters

This section discusses the effects of varying the aspect angle and altitude on the maneuver durations. The aspect angle strongly determines the relative geometry between the primer vectors of each control law and the SRP acceleration envelope. Figures 5.1 and 5.2 show schematics of the primer vectors and SRP acceleration envelope for a polar orbit with aspect angles of 90 and 0 degrees, respectively. For an aspect angle of 90 degrees, $\lambda_{a_{max}}$ is most aligned with the SRP acceleration envelope, while for an aspect angle of 0 degrees, $\lambda_{\Omega_{max}}$ is most aligned. As the goal of the LOCLs is to maximize the acceleration component along a primer vector, control laws with primer vectors that are most aligned with the SRP acceleration envelope, and hence the direction of sunlight, will experience the largest acceleration components in the desired direction in scenarios where the SRP force is dominant over drag. As drag becomes increasingly dominant at lower altitudes, it is expected that the observed patterns in control law usage will change, with a smaller favourability to aligning with the SRP acceleration envelope .

Figure 5.15 shows how the maneuver duration is affected by ranges of altitude and RAAN. A reduction in maneuver duration is observed at lower altitudes, which is expected given the greater drag. Further, the use of control laws are consistent with the expectations in Section 5.2, where a clear trend is observed between the use of SMA control laws for large aspect angles and RAAN control laws for smaller aspect angles. Further, the maneuver durations observed are shorter for RAAN control, with SMA control being utilized for longer duration maneuvers. An expected switch between RAAN maximization and minimization is observed; $\lambda_{\Omega_{max}}$ and $\lambda_{\Omega_{min}}$ are most aligned with the SRP acceleration envelopes at RAANs close to 90 and 270 degrees, respectively (corresponding to

Figures 5.2 and 5.3, respectively). SRP only becomes significant relative to the drag force at an altitude of 800 km, when the SMA maximization control law is the most effective at high aspect angles.

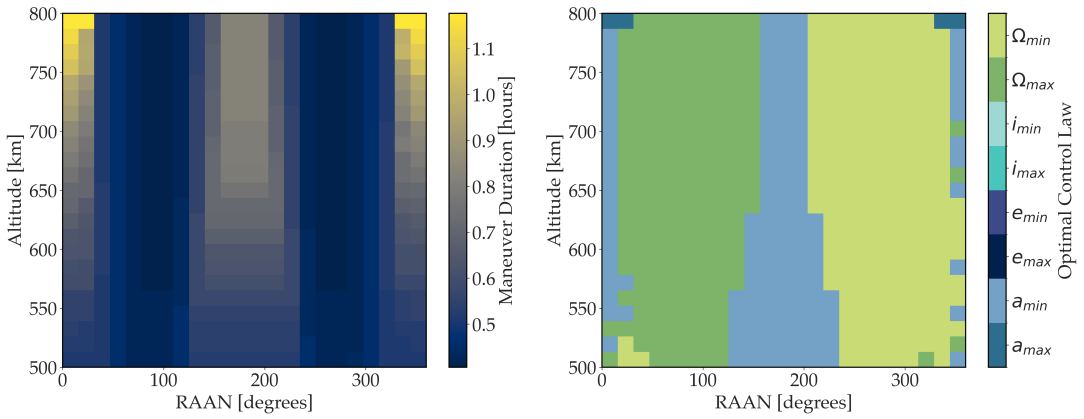

Figure 5.15: Maneuver durations and control law usage across RAANs and altitudes.

Figure 5.16 shows the maneuver durations, control law usage and eclipse fractions for a range of altitudes and RAANs using SRP-only control. The observed jump in maneuver duration across the diagonal corresponds to maneuvers entering eclipse, thus leading to increases in maneuver durations equal to the eclipse fraction of the orbital period of the corresponding altitude-RAAN combination. To verify this, the difference in maneuver durations across the diagonal as fractions of the orbital period for four selected combinations of altitude and RAAN from Figure 5.16 are presented in Table 5.1. The results show a general agreement with the computed eclipse fractions, indicating that the jump in maneuver duration indeed corresponds to the respective orbit's eclipse fraction. Given that the minimum altitude in this analysis is 750 km, it is expected that apart from SRP, there are no additional forces that affect the sail's orbit, such that during eclipse, no orbital modifications are made, leading to a jump in maneuver duration equivalent to the eclipse fraction duration.

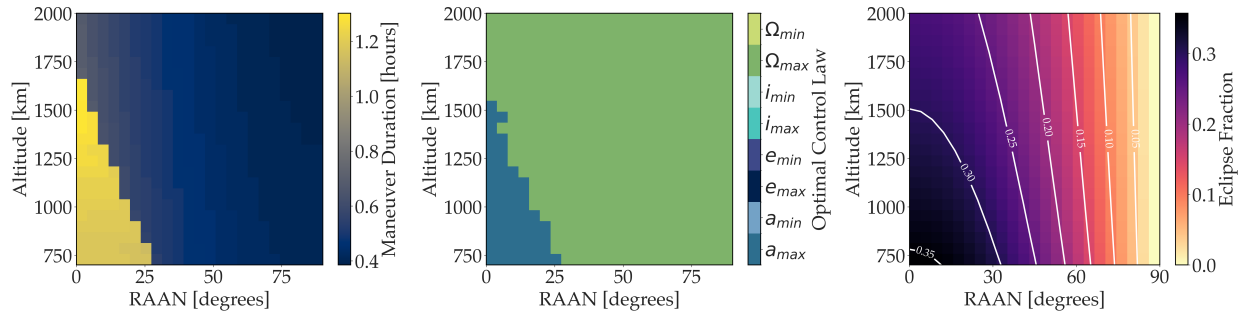

Figure 5.16: Maneuver duration, control law and eclipse fraction distribution for different RAANs and altitudes using the SRP-only control law.

5.3.3. The Effect of Conjunction Parameters

The effect of varying the conjunction separation in both tangential and normal directions on the maneuver duration is analyzed for different aspect angles. Figure 5.17 shows the effect of different separations in the T-N plane for scenario 4, where the aspect angle is 90 degrees. The separation is defined in terms of the secondary object with respect to the primary object, such that a positive

Table 5.1: Differences in maneuver duration across the diagonal as a fraction of orbital period for altitude-RAAN combinations along the diagonal separating the long and short maneuver durations in Figure 5.16.

$h[km], \Omega[deg]$	Eclipse fraction	$(t_{man,long} - t_{man,short})/T_{h,\Omega}$
$h = 750, \Omega = 25.2$	0.31	0.31
$h = 1000, \Omega = 18.0$	0.31	0.32
$h = 1250, \Omega = 10.8$	0.31	0.31
$h = 1500, \Omega = 3.6$	0.30	0.28

TCA ΔT represents a separation at TCA where the secondary object is positioned somewhere in the positive along-track direction of the primary object. The results show symmetry about TCA $\Delta N = 0$ m in maneuver duration, with a switch between the Ω_{max} and Ω_{min} control laws depending on the direction of the normal separation. Interestingly, the a_{min} control law is most effective even for positive tangential separations, which is due to the drag effects at this altitude.

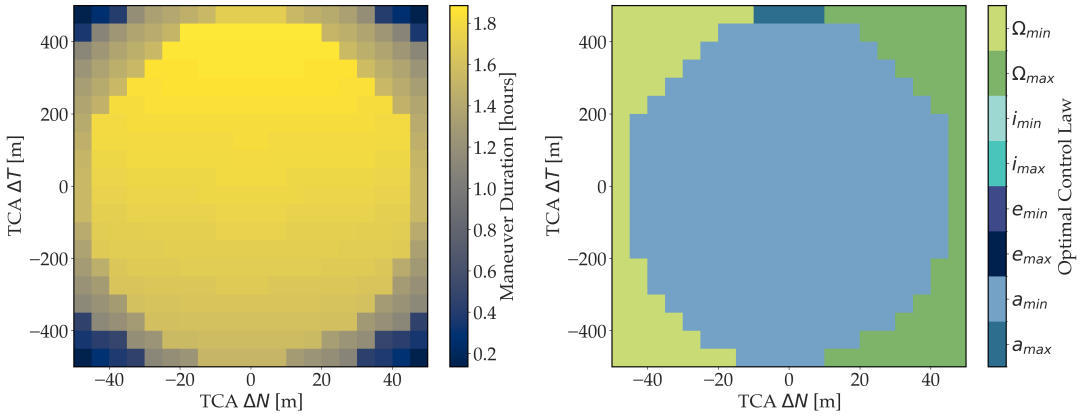

Figure 5.17: Effect of tangential and normal separation at TCA on maneuver duration for a 590 km altitude and aspect angle of 90 degrees.

For scenario 3, where the aspect angle is 0 degrees, a conjunction separation in the *T-N* plane leads to asymmetrical maneuver duration results, as seen in Figure 5.18. The asymmetry is due to the fact that the sail can only generate out-of-plane accelerations on one side of the orbital plane in this scenario. The "curve" dividing the usage of the Ω_{max} and $a_{max/min}$ control law defines a region where Ω_{max} is effective; positive values of ΔN lead to a greater positive ΔN via Ω_{max}. A switch between a_{max} and a_{min} control is observed, which is symmetric about TCA $\Delta T = 0$ m. This corresponds to an increase or decrease in orbital period when using the a_{max} or a_{min} control laws, respectively, thus causing an even greater positive or negative separation, respectively, in the tangential axis.

The change in maneuver duration observed is significant in Figure 5.17, with durations reducing by over an hour for a change in TCA ΔN from 0 to 40 meters at large vales of TCA ΔT. This corresponds to the small uncertainties in the normal direction, such that small displacements in the normal direction lead to large decreases in uncertainty (compared to similar displacements in the tangential direction), and hence lower maneuver times to satisfy the collision risk threshold. The required increase in miss distance in the tangential direction for similar reductions in maneuver duration are considerably higher, corresponding to the much larger uncertainties in the tangential direction.

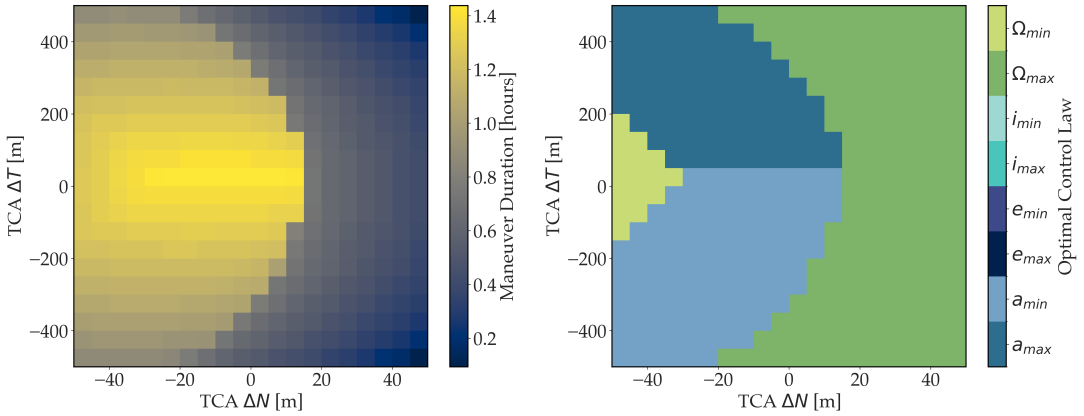

Figure 5.18: Effect of tangential and normal separation at TCA on maneuver duration for a 590 km altitude and aspect angle of 0 degrees.

Figure 5.19 shows the distribution of maneuver durations for the SRP-only and SRP+drag control laws for all simulated ranges in Table 4.5. While the use of SRP-only and SRP+drag is determined by the simulated altitude, a large overlap in maneuver duration values is observed due to the ranges of multiple other parameters that were used in generating the results. The main peak in SRP-only results is centered around 24-26 minutes, which is within the range obtained by Ambrosio (2025). Maneuver durations over 2 hours were omitted due to their sparseness and association to results generated only for LAMR objects. A larger fraction of SRP+drag control maneuvers are of relatively short duration in comparison to the SRP-only maneuvers, resulting from their effective usage at low altitudes. A secondary peak for the SRP-only control is observed around the 70-minute mark; this corresponds to the high-altitude (above 750 km) and high-aspect angle (close to 90 degrees) scenarios where there is a jump in maneuver durations for maneuvers that enter eclipse regions.

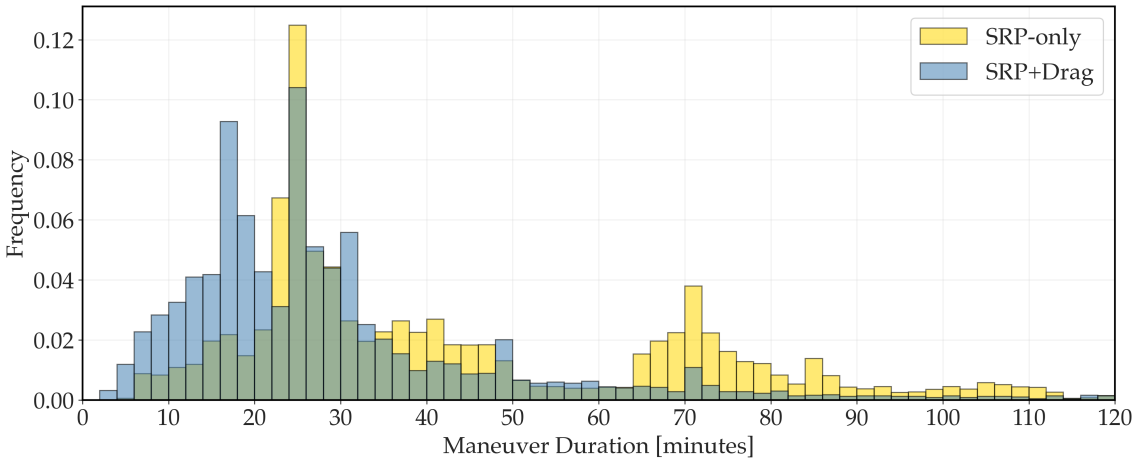

Figure 5.19: Histogram of maneuver duration for SRP-only and SRP+drag control laws

6 Conclusions and Future Work

This chapter concludes the thesis and presents the main findings and contributions of the work. Section 6.1 summarizes the key results and insights of the thesis in the context of the research questions formulated in Chapter 3, followed by Section 6.2 which discusses the limitations of the work and suggests avenues for future research.

6.1. Conclusions

This work involved the development of a simulation framework to assess the applicability of locally optimal control laws for collision-avoidance maneuvers of solar sails in low Earth orbit (LEO) where drag is non-negligible. Several capabilities were developed in order to perform this assessment, including a dynamical model that includes perturbing effects from Earth's oblateness, solar radiation pressure (SRP) and atmospheric drag. Results show a significant range of maneuver durations, with clear effects of atmospheric drag and patterns in the use of specific control laws across simulation scenarios. More focused conclusions are drawn in relation to the research questions formulated in Chapter 3:

Research Question 1

What are the minimum maneuver durations required to safely maneuver a sailcraft away from a predicted collision using locally optimal control laws under the influence of solar radiation pressure and atmospheric drag at altitudes between 400 and 800 km?

The results indicate a high variability in optimal maneuver durations, ranging from as low as 5 minutes for large sails at very low altitudes to over 6 hours for low area-to-mass ratio (LAMR) objects at high altitudes. The range of maneuver durations is much higher than the results found in the work by Ambrosio (2025), in which maneuver durations are clustered between 30 and 60 minutes for scenarios in which only SRP and J_2 gravity are considered as perturbations at altitudes above 1000 km.

The lower maneuver durations are a result of the exponential increase in atmospheric density at lower altitudes, which initiates the use of the a_{min} (semi-major axis minimization) control law to quickly lower the sail's altitude using a face-on orientation relative to the velocity vector. Such maneuvers become increasingly "effective" at lower altitudes, with maneuver durations theoretically approaching zero minutes at lower altitudes. However, these scenarios become increasingly impractical given that the sail will rapidly de-orbit after executing such a maneuver, and in the best-case scenario, maintain its altitude using an edge-on orientation; this is however not an operational possibility given that a real sail will still have a non-zero cross-sectional area in an edge-on orientation,

and will be incapable of performing any attitude maneuvers without increasing its cross-sectional area.

Research Question 2

How are maneuver durations and the usage of control laws affected by different physical, orbital and conjunction parameters, such as the sailcraft's area-to-mass ratio, altitude, aspect angle, and miss distance at the time of closest approach?

The parametric analysis revealed several trends in the optimal maneuver durations as well as the usage of control laws across different ranges of parameters.

The physical parameters of the sail and debris were analyzed using the sail's area-to-mass ratio (AMR) and the sail's and debris' hard-body radii (HBR) at the time of closest approach (TCA). Higher sail AMR values lead to shorter maneuver durations, as expected, and also largely utilize a_{min} control at altitudes below approximately 525 km and switch to a_{max} control at higher altitudes when SRP becomes relatively significant. Lower AMR values lead to a switch from a_{min} to a_{max} at lower altitudes, presumably because the longer maneuver durations lead to a change in aspect angle as the Earth revolves around the Sun that is significant enough for a sufficient increase in coincidence between the SRP acceleration envelope and the optimal thrusting direction of the a_{max} control law.

Variations in the HBR of the sail represent scenarios in which a sail, of fixed AMR, changes its orientation relative to the conjunction plane right before the TCA. For an initial miss distance of zero meters, maneuver durations reduce by approximately 20% when the sail is near edge-on to the conjunction plane in comparison to being face-on. A miss distance in the T-N plane of 50 m and 10 m, respectively, leads to a reduction in maneuver duration of approximately 55% between face-on and near edge-on cases, as a reduced HBR combined with a miss distance is more effective in reducing collision probabilities.

The altitude of the sail's orbit had the largest effect on maneuver duration due to the exponential increase in atmospheric density at lower altitudes; this lead to the a_{min} control law being used most frequently at altitudes below 500 km. The aspect angle had a strong correlation with the control law usage, with SMA control laws being used more frequently for high aspect angles, and RAAN (Right Ascension of Ascending Node) control laws being used more frequently at lower aspect angles. This corresponds to the scenarios in which the SRP acceleration envelope is most aligned with the respective primer vectors. An interesting phenomenon is observed when analyzing the distribution of maneuver durations for SRP-only control across altitudes and RAANs; a jump in maneuver duration occurs for different combinations of altitude and RAAN, which is found to be equal to the amount of time spent in eclipse for those specific orbits. This indicates that eclipses are an important factor when implementing such collision-avoidance maneuvers.

The conjunction separation at TCA reveals interesting patterns about the use of specific control laws for separations between the primary and secondary objects in the T-N plane. Conjunctions that occur at a true anomaly of 0 degrees and an aspect angle of 90 degrees show a largely symmetric distribution

of maneuver duration, with an expected switch between RAAN minimization and maximization for negative and positive separations in the normal direction. When a similar conjunction occurs at an aspect angle of 0 degrees, separations in the negative normal direction, which point towards the Sun, yield a significant jump in maneuver duration, as SMA control laws, which are relatively ineffective at low aspect angles, need to be largely utilized.

Overall, the maneuver durations and control law usage display clear trends across different altitudes, aspect angles and physical parameters. Since at low altitudes the a_{min} control law becomes effective in reducing the SMA, the minimum altitudes at which a sail can still perform orbit-raising were analyzed; results show that during average solar weather conditions, orbit-raising can be performed using SRP-only control by sailcraft with an AMR of 5 m^2/kg (such as ACS3) at altitudes above approximately 590 km; when using SRP+drag control, increases in altitude of over 100 m can be achieved at initial altitudes above approximately 500 km for maneuver durations up to 24 hours. This indicates that altitudes below 500 km are unusable for solar sails, as orbit raising is ineffective given that the sail is heavily constrained to edge-on orientations relative to the velocity, and rapid increases in drag occur for small deviations away from this orientation.

6.2. Limitations and Future Work

This work involved several assumptions and limitations that could be addressed in future work, which are highlighted in this section.

Environment Model

This work did not consider the effect of gravitational perturbations of order greater than two or third-body perturbations. Including these perturbations in the model will lead to increased propagation accuracy, but given that most collision-avoidance maneuvers are performed within one orbit, it is unlikely that the results will display any noticeable change. The biggest improvement in environmental modelling can be made by extending the utilization of the NRLMSISE-00 model for atmospheric density. While considered one of the most accurate empirical models available, this work did not utilize its time-varying nature, and instead considered average values of solar and geomagnetic flux and a static atmosphere. It would be insightful to analyze the effect of varying solar, geomagnetic, geographic and temporal parameters on the collision-avoidance performance at low altitudes, as the atmospheric density was found to significantly vary for different points in the solar cycle.

Object Model

This work considered the primary object to be an ideal solar-sail with perfect reflectivity. Extending this model to an optical model will yield more accurate results. The attitude dynamics were not treated in this work, and it was assumed that the sail could instantaneously achieve desired attitudes at any epoch in the simulation. This is a significant limitation, as real sails will be limited by their attitude control authority, which is dictated by their Attitude Determination and Control System (ADCS). Further, no torque effects were considered, and it was assumed that all forces acted through the center of mass of the sail. The attitude changes required to orient the sail's normal vector to the desired direction was assumed to be purely driven by the ADCS. Future work could consider the

effect of external torques, and may even utilize them to passively achieve an edge-on orientation with respect to the conjunction plane, leading to a direct reduction in collision risk without the need to maneuver. Due to a sail's large surface area, differential drag along the sail's surface may also be utilized to generate passive torques to achieve reductions in the cross-sectional area projected on the conjunction plane. Certain orbital configurations may allow for the combined utilization of SRP and drag for passive attitude maneuvers.

Uncertainty Generation

The uncertainties of the primary and secondary objects in this work were generated using a regression model based on a dataset of conjunction data with limited density and coverage. This limits the confidence of the regression, particularly in regions of low data density. While it will certainly be beneficial to gain access to a more comprehensive dataset, given a limited dataset, it may be possible to achieve improved results using more advanced machine learning techniques that can better capture the cross-correlations between different parameters and their effect on state uncertainties.

Since the results generated in this work fundamentally depend on the uncertainties of the objects, exploring the effect of different uncertainty magnitudes in the RTN reference frame could yield insightful results on the sensitivity of the computed optimal maneuver durations to the uncertainties along different axes. For example, it is expected that larger uncertainties in the tangential direction would lead to an increased usage of RAAN control laws, which were shown in this work to be used more frequently for short duration maneuvers; SMA control laws would need to be utilized for longer durations in order to escape the elongated error ellipsoid along the tangential axis.

Control Laws

The implementation of a hierarchical grid-search method for SRP+drag is limited by the discretization of the grid, which leads to no guarantee of finding the globally optimal solution. Further, for high accuracy requirements, computational efficiency rapidly decreases. It would be beneficial to implement a robust and efficient control law that is capable of dealing with edge-cases.

The treatment of locally-optimal control laws in this work fundamentally limits the optimality of the obtained solutions. The goal of maximizing the instantaneous change in orbital elements is not the most optimal control mechanism for a collision avoidance maneuver. While they were shown to be effective in generating relatively short-term maneuvers, they have limitations related to their applicability across different orbital configurations and conjunctions; this indicates that the maneuver durations found in this work cannot be independently correlated to the orbital/physical/conjunction parameters or the control laws. Therefore, the implementation of a numerical control method that accounts for both SRP and drag with the objective of decreasing collision risk (instead of maximizing the change in orbital elements) would be particularly useful.

Operational Constraints

This work did not consider any operational constraints in the simulated scenarios. Maneuvers were performed right up to the TCA, but typical CAMs are performed well in advance of the TCA. There is no guarantee that the results found in this work will be applicable if the maneuver execution is simply performed at an earlier time. This is primarily due to the effects of drag, which would affect

the orbit of the sail between the end of the maneuver up to the TCA. This effect would be detrimental at low altitudes when a_{max} control laws are utilized, as drag would undo the orbit-raising effects after the end of the maneuver. Future work could characterize this effect by finding scenarios in which a range of maneuver execution "lead times" lead to favourable or detrimental results.

Another avenue for future work could involve the determination of maneuvers for a sail to return to its operational orbit after performing a CAM. This would limit the number and type of possible CAMs that can be performed, especially when the objective is to return to a nominal orbit in the minimum possible time. Further, if the mission has certain pointing requirements for purposes such as communication with ground stations, these can be added as constraints in the optimal control problem.

References

[1] Alfano, S., & Oltrogge, D. (2018). Probability of collision: Valuation, variability, visualization, and validity. *Acta Astronautica*, *148*, 301–316. https://doi.org/https://doi.org/10.1016/j.actaastro.2018.04.023

[2] Alfriend, K. T., Akella, M. R., Frisbee, J., Foster, J. L., Lee, D.-J., & Wilkins, M. (1999). Probability of collision error analysis. *Space Debris*, *1*(1), 21–35. https://doi.org/https://doi.org/10.1023/A:1010056509803

[3] Ambrosio, G. (2025). *Characterizing minimum-time collision avoidance maneuvers for solar sails in earth orbit* [Master's thesis]. Delft University of Technology.

[4] Ancona, E., & Kezerashvili, R. Y. (2024). Recent advances in space sailing missions and technology: Review of the 6th international symposium on space sailing (isss 2023). https://doi.org/https://doi.org/10.48550/arXiv.2411.12492

[5] Aranda, D., Gago, P., Pastor, A., & Escobar, D. (2024). Drag augmentation for collision avoidance in leo. *Advances in Space Research*. https://doi.org/https://doi.org/10.1016/j.asr.2024.07.014

[6] Battin, R. H. (1999). *An introduction to the mathematics and methods of astrodynamics, revised edition*. AIAA.

[7] Biddy, C., & Svitek, T. (2012). Lightsail-1 solar sail design and qualification. *Proceedings of the 41st Aerospace Mechanisms Symposium*, 451–463.

[8] Bonnal, C., Ruault, J.-M., & Desjean, M.-C. (2013). Active debris removal: Recent progress and current trends. *Acta Astronautica*, *85*, 51–60. https://doi.org/https://doi.org/10.1016/j.actaastro.2012.11.009

[9] Braun, V., Flohrer, T., Krag, H., Merz, K., Lemmens, S., Bastida Virgili, B., & Funke, Q. (2016). Operational support to collision avoidance activities by esa's space debris office. *CEAS Space Journal*, *8*(3), 177–189.

[10] Burnett, E. R., & Schaub, H. (2021). Spacecraft formation and orbit control using differential attitude-dependent solar radiation pressure. *Advances in Space Research*, *67*(11), 3396–3408. https://doi.org/https://doi.org/10.1016/j.asr.2020.03.047

[11] Cao, J., Clemente, C., McInnes, C. R., & Soraghan, J. J. (2020). Solar radiation pressure enabled femtosatellite-based earth remote sensing. *IEEE Transactions on Aerospace and Electronic Systems*, *56*(5), 3450–3461. https://doi.org/10.1109/TAES.2020.2972242

[12] Carer, C., & Mooij, E. (2025). Space debris collision avoidance manoeuvre design and analysis. https://doi.org/10.2514/6.2025-0984

[13] Carzana, L., Visser, P., & Heiligers, M. (2021). Solar-sail control laws for perturbed earth-bound trajectories. *72nd Int. Astronaut. Conf.*

[14] Carzana, L., Visser, P., & Heiligers, J. (2022). Locally optimal control laws for earth-bound solar sailing with atmospheric drag. *Aerospace Science and Technology*, *127*, 107666. https://doi.org/https://doi.org/10.1016/j.ast.2022.107666

[15] Chan, F. K. (2008). *Spacecraft collision probability*. American Institute of Aeronautics; Astronautics, Inc.

[16] Chu, Y., & Gong, S. (2024). Minimum-time rendezvous for sun-facing diffractive solar sails with diverse deflection angles. *Astrodynamics*, *8*(4), 613–631. https://doi.org/https://doi.org/10.1007/s42064-024-0207-7

[17] Chujo, T. (2022). Propellant-free attitude control of solar sails with variable-shape mechanisms. *Acta Astronautica*, *193*, 182–196. https://doi.org/https://doi.org/10.1016/j.actaastro.2021.12.044

[18] Chujo, T., Watanabe, K., & Takao, Y. (2024). Integrated attitude—orbit control of solar sail with single-axis gimbal mechanism. *Astrodynamics*, *8*(4), 483–506. https://doi.org/https://doi.org/10.1007/s42064-023-0192-2

[19] Colombo, C., Giudici, L., Muciaccia, A., Gonzalo Gomez, J., Del Campo, B., Vyavahare, N., Dutra, D., Letizia, F., Lemmens, S., et al. (2023). Assessment of the collision risk in orbital slots and the overall space capacity. *2nd International Orbital Debris Conference (IOC II)*, 1–10.

[20] Colombo, C., Rossi, A., Vedova, F., Braun, V., Bastida Virgili, B., Krag, H., et al. (2017). Drag and solar sail deorbiting: Re-entry time versus cumulative collision probability. *International Astronautical Congress: IAC Proceedings*, 3535–3553.

[21] Curtis, H. D. (2005). *Orbital mechanics for engineering students*. Elsevier Butterworth-Heinemann.

[22] De Vittori, A., Palermo, M. F., Lizia, P. D., & Armellin, R. (2022). Low-thrust collision avoidance maneuver optimization. *Journal of Guidance, Control, and Dynamics*, *45*(10), 1815–1829. https://doi.org/https://doi.org/10.2514/1.G006630

[23] Dominguez-Gonzalez, R., Sanchez-Ortiz, N., Gelhaus, J., & Krag, H. (2013). Update of esa drama ares: Comparison of envisaged collision alerts with operational statistics and impact of catalogue accuracy. *6th European Conference on Space Debris*, *723*, 168.

[24] Dono, A., Hendriks, T., Wilkie, K., Rhodes, A., & Aquilina, R. (2025). Navigation for the acs3 solar sail mission. *Small Satellites Systems and Services Symposium (4S 2024)*, *13546*, 469–482.

[25] Ermolli, I., Matthes, K., Dudok de Wit, T., Krivova, N. A., Tourpali, K., Weber, M., Unruh, Y. C., Gray, L., Langematz, U., Pilewskie, P., et al. (2013). Recent variability of the solar spectral irradiance and its impact on climate modelling. *Atmospheric Chemistry and Physics*, *13*(8), 3945–3977.

[26] ESA, S. D. O. (2024). *Esa's annual space environment report* (tech. rep.). Technical report.

[27] Fieseler, P. D. (1998). A method for solar sailing in a low earth orbit. *Acta Astronautica*, *43*(9–10), 531–541. https://doi.org/https://doi.org/10.1016/S0094-5765(98)00175-1

[28] Foster, C., Mason, J., Vittaldev, V., Leung, L., Beukelaers, V., Stepan, L., & Zimmerman, R. (2018). Constellation phasing with differential drag on planet labs satellites. *Journal of Spacecraft and Rockets*, *55*(2), 473–483. https://doi.org/https://doi.org/10.2514/1.A33927

[29] Foster, J. (2001). The analytic basis for debris avoidance operations for the international space station. *EUROPEAN SPACE AGENCY-PUBLICATIONS-ESA SP*, *473*, 441–446.

[30] Fu, B., Sperber, E., & Eke, F. (2016). Solar sail technology—a state of the art review. *Progress in Aerospace Sciences*, *86*, 1–19. https://doi.org/https://doi.org/10.1016/j.paerosci.2016.07.001

[31] Gámez Losada, F., Visser, P., & Heiligers, J. (2024). Fundamentals of solar-sail transfers around planetary bodies. *Available at SSRN 5182531*.

[32] Gauvain, B. M., & Tyler, D. A. (2023). A solar sail shape modeling approach for attitude control design and analysis. *6th International Symposium on Space Sailing (ISSS)*.

[33] Ghrist, R., & Plakalovic, D. (2012). Impact of non-gaussian error volumes on conjunction assessment risk analysis. *AIAA/AAS Astrodynamics specialist conference*, 4965.

[34] Gong, S., & Macdonald, M. (2019). Review on solar sail technology. *Astrodynamics*, *3*(2), 93–125. https://doi.org/https://doi.org/10.1007/s42064-019-0038-x

[35] Gonzalo, J. L., Colombo, C., & Di Lizia, P. (2021a). Analytical framework for space debris collision avoidance maneuver design. *Journal of Guidance, Control, and Dynamics*, *44*(3), 469–487. https://doi.org/https://doi.org/10.2514/1.G005398

[36] Gonzalo, J. L., Colombo, C., & Di Lizia, P. (2021b). Analytical framework for space debris collision avoidance maneuver design. *Journal of Guidance, Control, and Dynamics*, *44*(3), 469–487. https://doi.org/https://doi.org/10.2514/1.G005398

[37] Gonzalo Gomez, J., Colombo, C., Di Lizia, P., et al. (2019). Drag-and srp-induced effects in uncertainty evolution for close approaches. *4th International Workshop on Key Topics in Orbit Propagation Applied to Space Situational Awareness (KePASSA)*, 45–45.

[38] Gonzalo Gomez, J. L., Colombo, C., Di Lizia, P., et al. (2018). Analysis and design of collision avoidance maneuvers for passive de-orbiting missions. *Advances in the Astronautical Sciences*, *167*, 2189–2208.

[39] Hall, D. T., Baars, L. G., & Casali, S. J. (2023). A multistep probability of collision computation algorithm. *AAS/AIAA Astrodynamics Specialist Conference*.

[40] Hernando-Ayuso, J., & Bombardelli, C. (2021). Low-thrust collision avoidance in circular orbits. *Journal of Guidance, Control, and Dynamics*, *44*(5), 983–995. https://doi.org/https://doi.org/10.2514/1.G005547

[41] Ismail, M., Bakry, A., Selim, H., & Shehata, M. (2015). Eclipse intervals for satellites in circular orbit under the effects of earth's oblateness and solar radiation pressure. *NRIAG Journal of Astronomy and Geophysics*, *4*(1), 117–122. https://doi.org/10.1016/j.nrjag.2015.06.001

[42] Ivanov, D., Kushniruk, M., & Ovchinnikov, M. (2018). Study of satellite formation flying control using differential lift and drag. *Acta Astronautica*, *152*, 88–100.

[43] Johnson, L., Whorton, M., Heaton, A., Pinson, R., Laue, G., & Adams, C. (2011). Nanosail-d: A solar sail demonstration mission. *Acta astronautica*, *68*(5-6), 571–575.

[44] Kechichian, J. A. (1997). Optimal low-thrust transfer using variable bounded thrust. *Acta Astronautica*, *40*(11), 779–784.

[45] Kelly, P., & Bevilacqua, R. (2020). Geostationary debris mitigation using minimum time solar sail trajectories with eclipse constraints. *Optimal Control Applications and Methods*, *42*(1), 279–304. https://doi.org/https://doi.org/10.1002/oca.2676

[46] Kim, E.-H., Kim, H.-D., & Kim, H.-J. (2012). A study on the collision avoidance maneuver optimization with multiple space debris. *Journal of Astronomy and Space Sciences*, *29*(1), 11–21. https://doi.org/10.5140/JASS.2012.29.1.011

[47] Kim, K. (2024). Preliminary trajectory design for mitigating debris utilizing solar sailing and conventional propulsion. *International Journal of Aeronautical and Space Sciences*. https://doi.org/https://doi.org/10.1007/s42405-024-00833-2

[48] Klinkrad, H., Alarcón, J., & Sánchez, N. (2006). Space debris. *Springer Praxis Books*, 215–240. https://doi.org/https://doi.org/10.1007/3-540-37674-7_8

[49] Kubo, Y., & Chujo, T. (2024). Optimization of body configuration and joint-driven attitude stabilization for transformable spacecraft under solar radiation pressure. *Astrodynamics*, *8*(1), 47–60. https://doi.org/https://doi.org/10.1007/s42064-023-0167-3

[50] Kumar, K. D., Misra, A. K., Varma, S., Reid, T., & Bellefeuille, F. (2014). Maintenance of satellite formations using environmental forces. *Acta Astronautica*, *102*, 341–354. https://doi.org/https://doi.org/10.1016/j.actaastro.2014.05.001

[51] Le May, S., Gehly, S., Carter, B., & Flegel, S. (2018). Space debris collision probability analysis for proposed global broadband constellations. *Acta Astronautica*, *151*, 445–455. https://doi.org/https://doi.org/10.1016/j.actaastro.2018.06.036

[52] Levin, E. (1968). Solar radiation pressure perturbations of earth satellite orbits. *AIAA Journal*, *6*(1), 120–126. https://doi.org/https://doi.org/10.2514/3.4451

[53] Lewis, H. G., & Skelton, G. (2024). Safety considerations for large constellations of satellites. *Journal of Space Safety Engineering*, *11*(3), 439–445.

[54] Li, R., & Lei, J. (2021). The determination of satellite orbital decay from pod data during geomagnetic storms. *Space Weather*, *19*(4), e2020SW002664.

[55] Li, Z., Ziebart, M., Bhattarai, S., & Harrison, D. (2019). A shadow function model based on perspective projection and atmospheric effect for satellites in eclipse. *Advances in Space Research*, *63*(3), 1347–1359.

[56] Liou, J.-C., Johnson, N., & Hill, N. (2010). Controlling the growth of future leo debris populations with active debris removal. *Acta Astronautica*, *66*(5–6), 648–653. https://doi.org/https://doi.org/10.1016/j.actaastro.2009.08.005

[57] Liu, H.-K., Li, B., Zhang, Y., & Sang, J.-Z. (2023). A data-driven method for realistic covariance prediction of space object with sparse tracking data. *Research in Astronomy and Astrophysics*, *23*(8), 085014. https://doi.org/10.1088/1674-4527/acd7be

[58] Macdonald, M., & McInnes, C. R. (2005). Analytical control laws for planet-centered solar sailing. *Journal of Guidance, Control, and Dynamics*, *28*(5), 1038–1048.

[59] Macdonald, M., McKay, R., Vasile, M., & Frescheville, F. B. d. (2010). Extension of the sun-synchronous orbit. *Journal of Guidance, Control, and Dynamics*, *33*(6), 1935–1940.

[60] Mangus, D., & Heaton, A. (2004). Solar sail control actuator concepts. *Solar Sail Technology and Applications Conference*.

[61] Matney, M., Anz-Meador, P., & Foster, J. (2004). Covariance correlations in collision avoidance probability calculations. *Advances in Space Research*, *34*(5), 1109–1114. https://doi.org/https://doi.org/10.1016/j.asr.2003.11.012

[62] McInnes, C. R. (2004). *Solar sailing: Technology, dynamics and mission applications*. Springer Science & Business Media.

[63] McInnes, C. R., Eiden, M., Groepper, P., & Peacock, T. (2001). Solar sailing-mission opportunities and innovative technology demonstration. *ESA European Space Agency Bulletin*, *108*, 58–65.

[64] Meireles, L. G., Prado, A. F. B. A., de Melo, C. F., & Pereira, M. C. (2022). A study on different attitude strategies and mission parameters based on lightsail-2. *Revista Mexicana de Astronomía y Astrofísica*, *58*(1), 23–35. https://doi.org/https://doi.org/10.22201/ia.01851101p.2022.58.01.02

[65] Meireles, L. G., Gomes, V. M., Prado, A. F. B. d. A., & Melo, C. F. d. (2023). Optimum, suboptimal and solar sailing orbital maneuvers for a spacecraft orbiting the earth. *Symmetry*, *15*(2), 512. https://doi.org/https://doi.org/10.3390/sym15020512

[66] Merz, K., Bastida Virgili, B., Braun, V., Flohrer, T., Funke, Q., Krag, H., Lemmens, S., & Siminski, J. (2017). Current collision avoidance service by esa's space debris office. *7th European Conference on Space Debris*, 219.

[67] Mishne, D. (2016). Collision avoidance maneuver of propulsionless satellite, using solar radiation pressure. *The 56th Israel Annual Conference on Aerospace Sciences, Israel Soc. of Aeronautics and Astronautics Paper WeL2T3*, *3*.

[68] Mishne, D., & Edlerman, E. (2017). Collision-avoidance maneuver of satellites using drag and solar radiation pressure. *Journal of Guidance, Control, and Dynamics*, *40*(5), 1191–1205. https://doi.org/https://doi.org/10.2514/1.G002376

[69] Modenini, D., Curzi, G., & Locarini, A. (2022). Relations between collision probability, mahalanobis distance, and confidence intervals for conjunction assessment. *Journal of Spacecraft and Rockets*, *59*(4), 1125–1134.

[70] NASA Marshall Space Flight Center. (2025, August). Solar cycle progression and forecast [Accessed: 2025-08-22].

[71] Newman, L. K., Frigm, R., & McKinley, D. (2009). It's not a big sky after all: Justification for a close approach prediction and risk assessment process. *2009 AAS/AIAA Astrodynamics Specialist Conference*, (AAS 09-369).

[72] Niccolai, L., Quarta, A. A., & Mengali, G. (2017). Analytical solution of the optimal steering law for non-ideal solar sail. *Aerospace Science and Technology*, *62*, 11–18. https://doi.org/https://doi.org/10.1016/j.ast.2016.11.031

[73] Nugnes, M., Colombo, C., et al. (2022). Multi-revolution low-thrust trajectory optimisation using differential dynamic programming in orbital element formulation. *INTERNATIONAL ASTRONAUTICAL CONGRESS: IAC PROCEEDINGS*, 1–9.

[74] Palermo, M. F., Di Lizia, P., Armellin, R., et al. (2021). Numerically efficient methods for low-thrust collision avoidance maneuver design. *8th European Conference on Space Debris, ESA/ESOC*, 1–15.

[75] Parkinson, R. W., Jones, H. M., & Shapiro, I. I. (1960). Effects of solar radiation pressure on earth satellite orbits. *Science*, *131*(3404), 920–921. https://doi.org/https://doi.org/10.1126/science.131.3404.920

[76] Patera, R. (2000). A general method for calculating satellite collision probability (aas 00-182). *Advances in the astronautical sciences*, *105*(2), 1275–1290.

[77] Patera, R. P. (2003). Satellite collision probability for nonlinear relative motion. *Journal of Guidance, Control, and Dynamics*, *26*(5), 728–733. https://doi.org/https://doi.org/10.2514/2.5127

[78] Patera, R. P., & Peterson, G. E. (2003). Space vehicle maneuver method to lower collision risk to an acceptable level. *Journal of Guidance, Control, and Dynamics*, *26*(2), 233–237. https://doi.org/10.2514/2.5063

[79] Picone, J., Hedin, A., Drob, D. P., & Aikin, A. (2002). Nrlmsise-00 empirical model of the atmosphere: Statistical comparisons and scientific issues. *Journal of Geophysical Research: Space Physics*, *107*(A12), SIA–15.

[80] Polat, H., & Tekinalp, O. (2020). Station-keeping strategy for a solar sail satellite at low earth elliptical orbit. *Southeast Europe Space Conference*.

[81] Pollock, K. (1994). An analysis of orbital propagators for low earth orbit rendezvous(m. s. thesis).

[82] Pu, H., Guangwei, W., & Zhaokui, W. (2025). Simultaneously adjusting deployment strategies for mega-constellations using low-thrust maneuvers. *Journal of Spacecraft and Rockets*, *62*(1), 196–205.

[83] Reid, T. G. R. (2017). *Orbital diversity for global navigation satellite systems* [Doctoral dissertation, Stanford University].

[84] Salemme, G., Armellin, R., & Di Lizia, P. (2020). Continuous-thrust collision avoidance manoeuvres optimization. https://doi.org/https://doi.org/10.2514/6.2020-0231

[85] Sánchez-Ortiz, N., Belló-Mora, M., & Klinkrad, H. (2006). Collision avoidance manoeuvres during spacecraft mission lifetime: Risk reduction and required $Delta$v. *Advances in Space Research*, *38*(9), 2107–2116. https://doi.org/https://doi.org/10.1016/j.asr.2005.07.054

[86] Serfontein, Z., Kingston, J., Hobbs, S., Holbrough, I. E., & Beck, J. C. (2021). Drag augmentation systems for space debris mitigation. *Acta Astronautica*, *188*, 278–288. https://doi.org/https://doi.org/10.1016/j.actaastro.2021.05.038

[87] Shan, M., Guo, J., & Gill, E. (2016). Review and comparison of active space debris capturing and removal methods. *Progress in Aerospace Sciences*, *80*, 18–32. https://doi.org/https://doi.org/10.1016/j.paerosci.2015.11.001

[88] Silva Neto, J., Sanchez, D., Prado, A., & Smirnov, G. (2017). On the use of controlled radiation pressure to send a satellite to a graveyard orbit. *Revista mexicana de astronomía y astrofísica*, *53*(2).

[89] Smid, S. C., McNeish, D., Miočević, M., & van de Schoot, R. (2020). Bayesian versus frequentist estimation for structural equation models in small sample contexts: A systematic review. *Structural Equation Modeling: A Multidisciplinary Journal*, *27*(1), 131–161.

[90] Spencer, D. A., Betts, B., Bellardo, J. M., Diaz, A., Plante, B., & Mansell, J. R. (2021). The lightsail 2 solar sailing technology demonstration. *Advances in Space Research*, *67*(9), 2878–2889.

[91] Spencer, D. A., Johnson, L., & Long, A. C. (2019). Solar sailing technology challenges. *Aerospace Science and Technology*, *93*, 105276. https://doi.org/https://doi.org/10.1016/j.ast.2019.07.009

[92] Spencer, H., & Carroll, K. A. (2014). Real solar sails are not ideal, and yes it matters. In *Advances in solar sailing* (pp. 921–940). Springer.

[93] Stolbunov, V., Ceriotti, M., Colombo, C., & McInnes, C. R. (2013). Optimal law for inclination change in an atmosphere through solar sailing. *Journal of Guidance, Control, and Dynamics*, *36*(5), 1310–1323. https://doi.org/10.2514/1.59931

[94] Sumanth, R. (2019). Computation of eclipse time for low-earth orbiting small satellites. *International Journal of Aviation, Aeronautics, and Aerospace*, *6*(5), 15.

[95] Swartzlander, G. A. (2022). Theory of radiation pressure on a diffractive solar sail. *Journal of the Optical Society of America B*, *39*(9), 2556. https://doi.org/10.1364/JOSAB.468588

[96] Thoemel, J., & van Dam, T. (2021). Autonomous formation flight using solar radiation pressure. *CEAS Space Journal*, *13*(4), 555–566. https://doi.org/https://link.springer.com/article/10.1007/s12567-020-00344-2

[97] Tsuda, Y., Mori, O., Funase, R., Sawada, H., Yamamoto, T., Saiki, T., Endo, T., & Kawaguchi, J. (2011). Flight status of ikaros deep space solar sail demonstrator. *Acta astronautica*, *69*(9-10), 833–840.

[98] Tsuda, Y., Mori, O., Funase, R., Sawada, H., Yamamoto, T., Saiki, T., Endo, T., Yonekura, K., Hoshino, H., & Kawaguchi, J. (2013). Achievement of ikaros—japanese deep space solar sail demonstration mission. *Acta Astronautica*, *82*(2), 183–188.

[99] Vallado, D. A. (2001). *Fundamentals of astrodynamics and applications*. Microcosm Press.

[100] Vallado, D. A., & Finkleman, D. (2014). A critical assessment of satellite drag and atmospheric density modeling. *Acta Astronautica*, *95*, 141–165.

[101] Varma, S. (2021). Control of satellites using environmental forces: Aerodynamic drag / solar radiation pressure. https://doi.org/https://doi.org/10.32920/ryerson.14649270.v1

[102] Wakker, K. F. (2015). Fundamentals of astrodynamics. *TU Delft Repository, Delft*, 604–612.

[103] Weston, S. V., Burkhard, C. D., Stupl, J. M., Ticknor, R. L., Yost, B. D., Austin, R. A., Galchenko, P., Newman, L. K., & Soto, L. S. (2025). State-of-the-art small spacecraft technology.

[104] Wie, B. (2004). Solar sail attitude control and dynamics, part 1. *Journal of Guidance, Control, and Dynamics*, *27*(4), 526–535. https://doi.org/10.2514/1.11134

[105] Wie, B., & Murphy, D. (2007). Solar-sail attitude control design for a flight validation mission. *Journal of Spacecraft and Rockets*, *44*(4), 809–821. https://doi.org/10.2514/1.22996

[106] Wilkie, W. K. (2021). Overview of the nasa advanced composite solar sail system (acs3) technology demonstration project. *AIAA scitech 2021 forum*, 1260.

[107] Williams, T., & Wang, Z.-S. (2002). Uses of solar radiation pressure for satellite formation flight. *International Journal of Robust and Nonlinear Control*, *12*(2–3), 163–183. https://doi.org/10.1002/rnc.681

[108] Yang, B., Li, S., Feng, J., & Vasile, M. (2022). Fast solver for j2-perturbed lambert problem using deep neural network. *Journal of Guidance, Control, and Dynamics*, *45*(5), 875–884.

[109] Yang Yang, F., Nelson, B., Aziz, J., Carlino, R., Dono Perez, A., Faber, N., Foster, C., Frost, C., Henze, C., Karacalıoğlu, A. G., Levit, C., Marshall, W., Mason, J., O'Toole, C., Swenson, J., Worden, S. P., & Stupl, J. (2016). Lightforce photon-pressure collision avoidance: Efficiency analysis in the current debris environment and long-term simulation perspective. *Acta Astronautica*, *126*, 411–423. https://doi.org/https://doi.org/10.1016/j.actaastro.2016.04.032

[110] Yoshimura, Y., Matsushita, Y., Takahashi, K., Nagasaki, S., & Hanada, T. (2023). Analytic approximation of high-fidelity solar radiation pressure. *Journal of Guidance, Control, and Dynamics*, *46*(1), 171–176. https://doi.org/https://doi.org/10.2514/1.G005961

[111] Zhau, P., Wu, C., & Li, Y. (2023). Design and application of solar sailing: A review on key technologies. *Chinese Journal of Aeronautics*, *36*(5), 125–144. https://doi.org/https://doi.org/10.1016/j.cja.2022.11.002

[112] Zollo, A., Di Campli Bayard de Volo, G., Weigel, M., Aida, S., Kahle, R., & San Juan Díaz, J. F. (2024). Synthetic orbit uncertainty generation through regression analysis of historical conjunction data messages. *Journal of Space Safety Engineering*, *11*(3), 454–461. https://doi.org/https://doi.org/10.1016/j.jsse.2024.06.001

A Software Verification

This chapter provides the methodologies used to verify the core capabilities of the developed software. Unit tests are performed to verify individual functionality of functions and scripts, and integration tests are performed to verify correct integration and interaction between the individual software modules and system tests are performed to verify overall functionality of a core capability of the software.

A.1. Dynamical Model

This section presents the methods used to verify the implementation of the dynamical model, control laws, uncertainty generation and collision probability computation.

Force Models

Figure A.1 shows the 24-hour evolution of orbital elements under the influence of only point-mass gravity of the Earth, displaying expected results consistent with literature (Vallado, 2001).

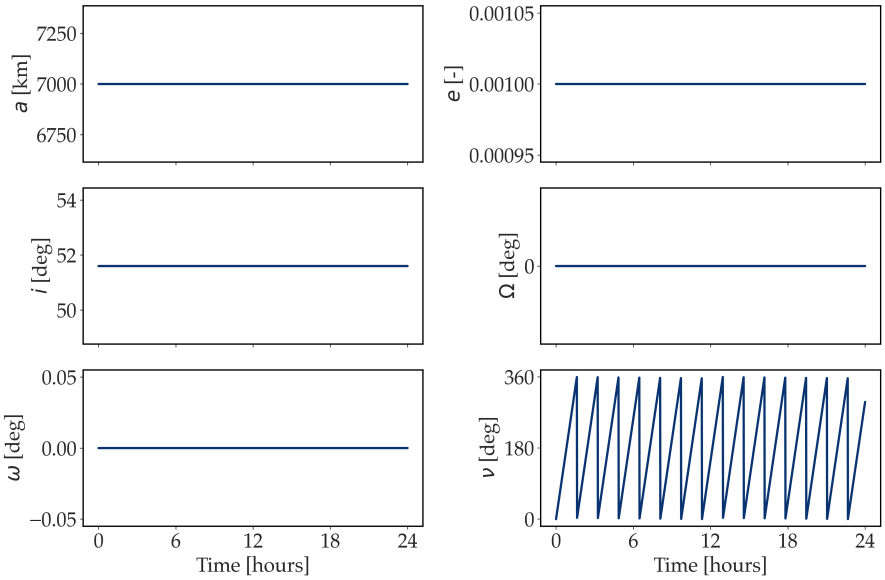

Figure A.1: Keplerian orbit propagation

Figure A.2a shows the evolution of RAAN over one-day propagation for a chosen SSO (Macdonald et al., 2010), showing a precession in RAAN of 0.9856 degrees per day, in agreement with literature (Wakker, 2015) The semi-major axis evolution is plotted in Figure A.2b using the same initial orbital conditions and satellite AMR as in Li and Lei (2021). The observed decay over a 24-hour period using matches with the results presented in Li and Lei (2021).

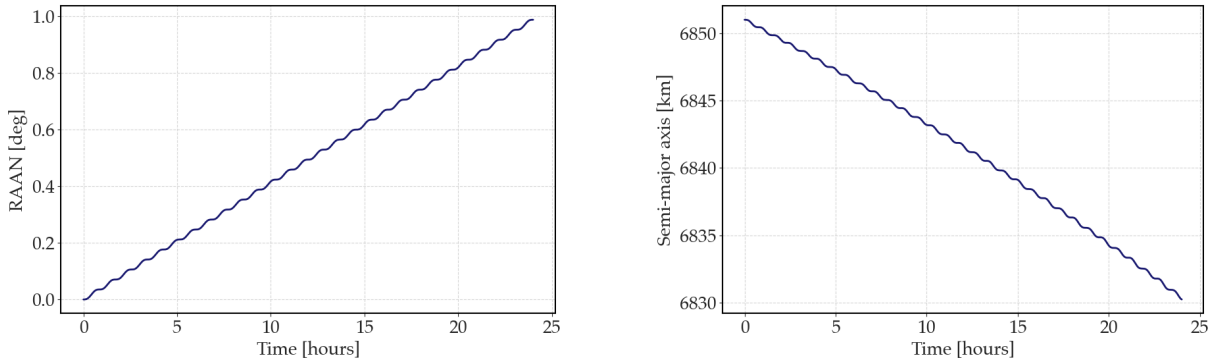

(a) **(b)**

Figure A.2: Propagations over 1 day using only (a) point-mass gravity and J_2 perturbation for an SSO, and (b) point-mass gravity and atmospheric drag.

To verify the implementation of the SRP model, the analytical locally optimal control law is applied to a scenario described in McInnes (2004). Figure A.3 presents the effect of applying a SMA maximization control law starting from a geostationary orbit on the SMA and eccentricity evolution. The results match the equivalent figures provided in McInnes (2004).

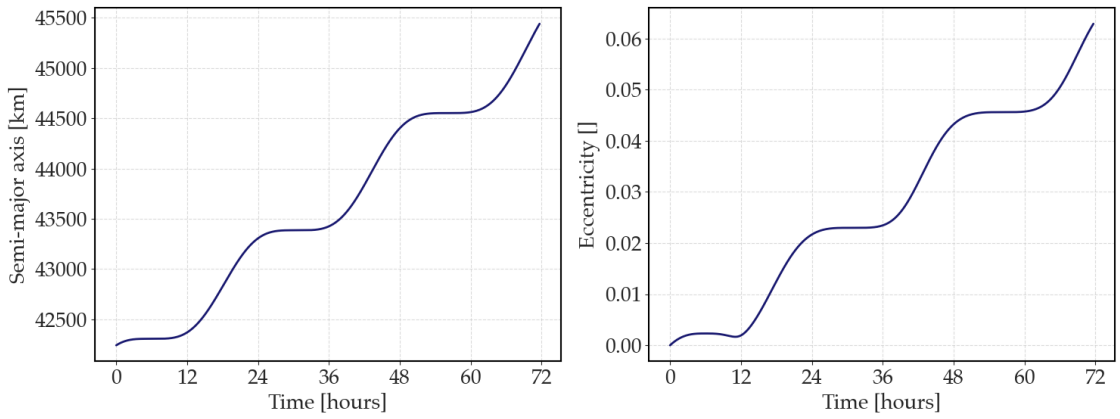

Figure A.3: Evolution of semi-major axis and eccentricity over 3 days for a geostationary orbit using an ideal solar sail with a characteristic acceleration of 1 mm/s^2, using a locally optimal control law for maximizing semi-major axis; the results are a reproduction of the figures in McInnes et al. (2001).

Eclipse Model

Figure A.4 shows the eclipse fractions across different RAANs and altitudes at the two equinoxes and solstices, with eclipse fraction values for altitude-RAAN combinations in agreement with literature (Sumanth, 2019). The eclipse fractions show consistent behaviour for different RAANs at the equinoxes and solstices, with an observed reduction in eclipse fractions for increasing altitude, as expected.

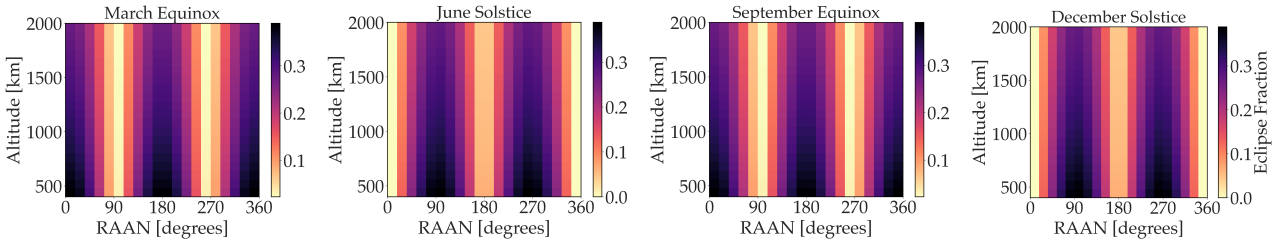

(a) March equinox **(b)** June solstice **(c)** September equinox **(d)** December solstice

Figure A.4: Eclipse fractions across different RAANs and altitudes at the two equinoxes and solstices.

Integrator Selection

To choose an appropriate integrator for this work, various integrators were tested for accuracy and computational efficiency, by analyzing their maximum position error during a one-day orbit in an environment with J_2, SRP, drag enabled for eight different combinations of relative and absolute tolerances. The benchmark used is the DOP853 integrator with a relative and absolute tolerance of 10^{-14}. The DOP853 is a variable-step explicit Runge-Kutta method of order 8, and is considered to provide the best combination of accuracy and computational performance for numerical propagation with *Scipy*[1], according to an online repository[2]. The DOP853 integrator is chosen based on the integrator comparison in Figure A.5a, showing the best trade-off between position accuracy and computational efficiency for this analysis. To choose a suitable tolerance, the position error evolution over a one-day orbit for the DOP853 integrator is plotted in Figure A.5b, for different tolerance combinations.

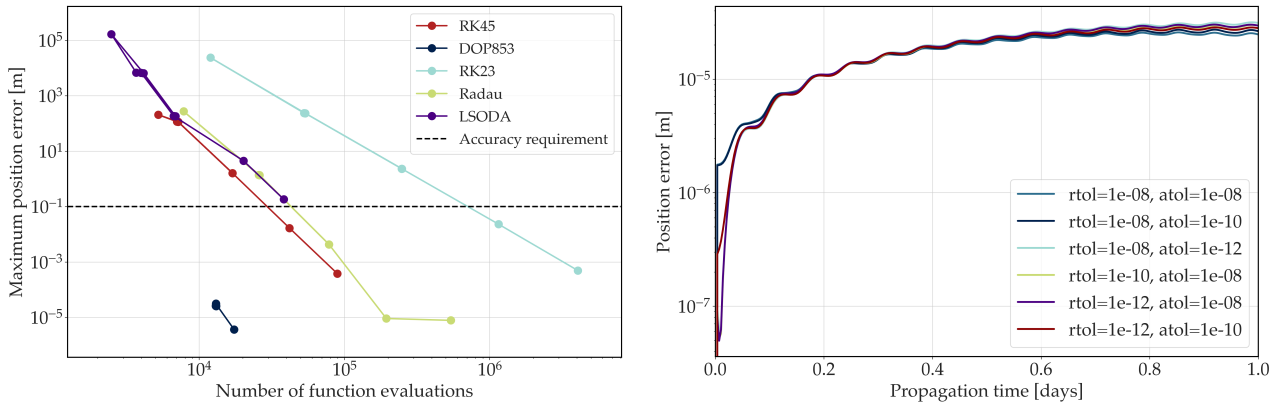

(a) Comparison of integrators for different relative and absolute tolerance combinations on their maximum position error over a one-day propagation and number of function evaluations.

(b) Evolution of position error over a one-day propagation using the DOP853 integrator for different relative and absolute tolerance combinations.

Figure A.5: Results of integrator comparison and tolerance analyses.

A.2. Control Law

Figure A.6 shows the comparison of the normal vector evolution between the computed and benchmarked values over one complete orbit for the SRP-only control law. The benchmarked values are obtained from a verified dataset, through the primary author of (Carzana et al., 2021). The small

[1] https://scipy.org/ (accessed on 4 September 2025)
[2] https://satmad.readthedocs.io/en/stable/propagation/numerical_propagation.html (accessed on 4 September 2025)

absolute error, in the order of 10^{-7}, throughout the orbit indicates that the implementation of the SRP-only control law is correct.

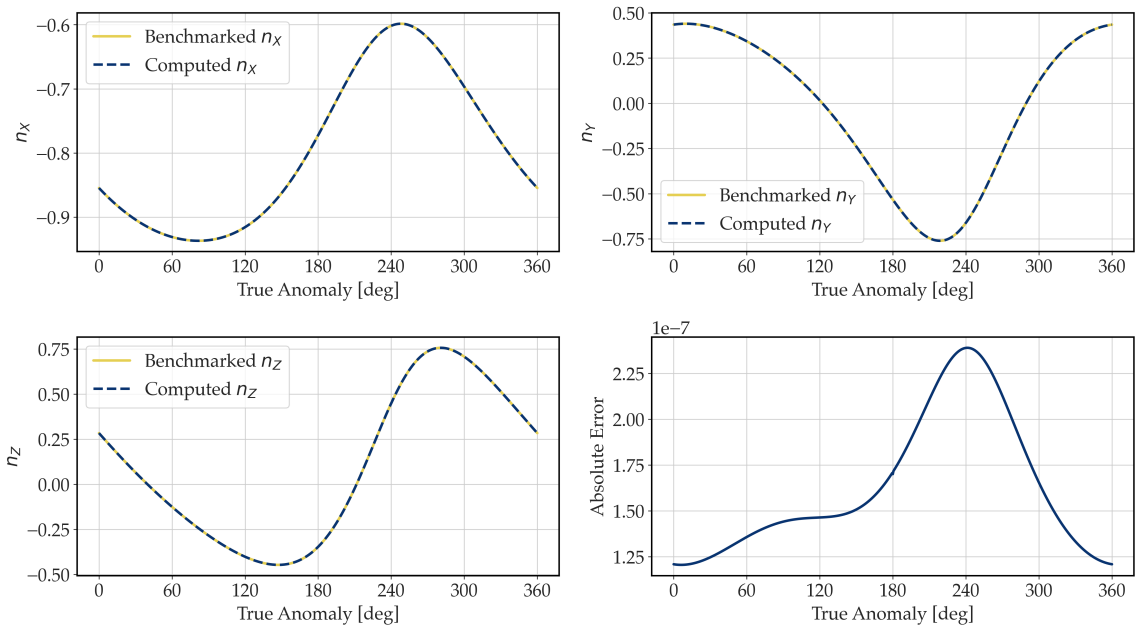

Figure A.6: Comparison of normal vector evolution between the computed and benchmarked values over one complete orbit for the SRP-only control law.

A.3. Synthetic Covariance Generation

The mean position RMS residual of 2649.15 m in Figure A.7 is similar to the equivalent value of 2540.47 m obtained using the fitting process reproduced for this work and applied to the utilized dataset from ESA.

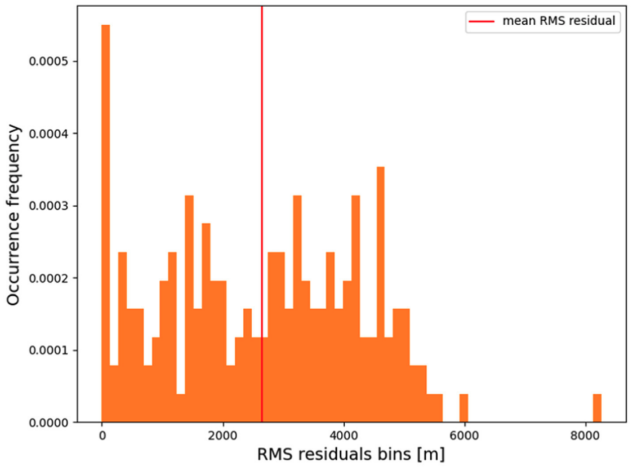

Figure A.7: Distribution of RMS residuals between the covariance coefficients generated through the fitting and the ones provided in the dataset; taken directly from Zollo et al. (2024).

The uncertainty-generation method used in this work is a reproduction of the classification and fitting methods used in Zollo et al. (2024). The dataset used in this work differs from the one used in Zollo et al. (2024), which uses an internal GSOC dataset. The orbital coverage is similar, with

a concentration of objects at high-inclination altitudes between 600 and 800 km, reflecting SSOs. However, the total number of CDMs in the dataset used in this work is 162,634, compared to 381,634 in Zollo et al. (2024). This suggests a lower overall confidence in the obtained fitting parameters, but given the similar position RMS residuals, the fitting process is considered to be correctly implemented. A significantly larger residual of 9128 m is observed when implementing the fitting process on a smaller dataset of 876 CCSDS CDMs of the Delfi satellites, obtained internally from TU Delft. The larger RMSE is expected given the significantly smaller size of the dataset, increasing the chances of bias in the fitting process (Smid et al., 2020).

A.4. Collision Probability

To verify the implementation of the collision probability calculation methods, a comparison is made with an analytical solution. For the special case of zero miss distance ($\boldsymbol{\mu} = \mathbf{0}$) and circular covariance ($\boldsymbol{\Sigma} = \sigma^2\mathbf{I}$), where σ represents the standard deviation in both tangential and normal directions, the collision probability integral results in a closed-form analytical solution:

$$P_c = 1 - \exp\left(-\frac{R_{\text{HBR}}^2}{2\sigma^2}\right) \tag{A.1}$$

The dimensionless parameter $\lambda = R_{\text{HBR}}/\sigma$ serves as an indicator of conjunction risk and determines the dominant physical regime of the encounter (Chan, 2008):

- **Small Object Regime** ($\lambda \ll 1$): When $R_{\text{HBR}} \ll \sigma$, the hard-body radius is much smaller than the position uncertainties. In this limit, Equation A.1 can be Taylor-expanded to yield:

$$P_c \approx \frac{R_{\text{HBR}}^2}{2\sigma^2} = \frac{\pi R_{\text{HBR}}^2}{2\pi\sigma^2} \tag{A.2}$$

  This represents the geometric collision cross-section divided by the area of the uncertainty ellipse, consistent with a dilute collision regime.

- **Intermediate Regime** ($\lambda \sim 1$): When $R_{\text{HBR}} \approx \sigma$, both geometric and probabilistic effects are significant. The collision probability exhibits maximum sensitivity to changes in either the hard-body radius or uncertainty level.

- **Large Object Regime** ($\lambda \gg 1$): When $R_{\text{HBR}} \gg \sigma$, the collision probability approaches unity ($P_c \to 1$), indicating near-certain collision given the small uncertainties relative to the collision cross-section.

The theoretical curve defined by Equation A.1 provides an exact benchmark for validating numerical collision probability algorithms. Key verification points include:

$$\lambda = \sqrt{2} \quad \Rightarrow \quad P_c = 1 - e^{-1} \approx 0.632 \tag{A.3}$$

$$\lambda = 1 \quad \Rightarrow \quad P_c = 1 - e^{-0.5} \approx 0.393 \tag{A.4}$$

$$\lambda = 2 \quad \Rightarrow \quad P_c = 1 - e^{-2} \approx 0.865 \tag{A.5}$$

Figure A.8 demonstrates the verification results for both methods across the full range of λ values. The close agreement with theoretical expectations of the Foster method verifies its correct implementation in this work. The Alfano method results in higher, more conservative values, in agreement with literature, and is computationally more efficient due to analytical approximations (Patera, 2000). In this work, the Foster method is utilized due to its superior accuracy.

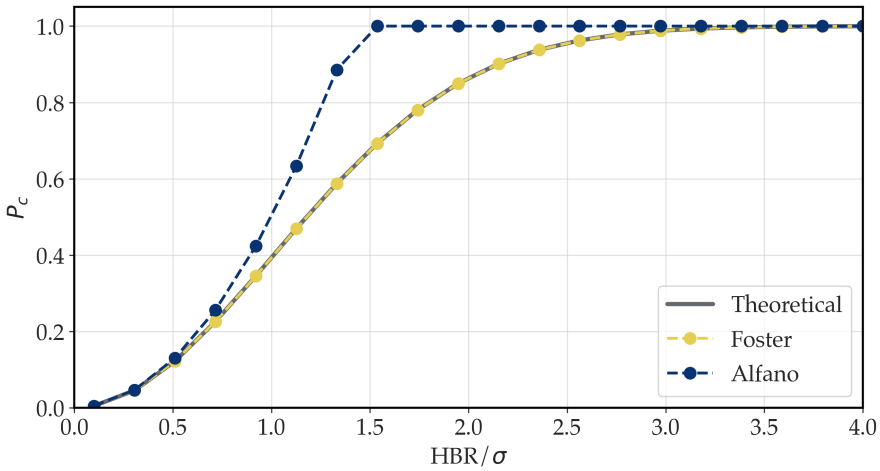

Figure A.8: Verification of Foster and Alfano collision probability methods against the analytical solution for a zero miss-distance scenario.

B Optimal Thrusting Vectors

This chapter provides the complete derivations of the four primer vectors used for each control law, as presented in 4.2. Gauss's planetary equations, which state the rate of change of orbital elements, are used as a starting point.

Gauss's Planetary Equations in RTN Coordinates

Consider a spacecraft subjected to a perturbative acceleration $\mathbf{a} = [a_R, a_T, a_N]^T$ expressed in the RTN coordinate frame, where $\hat{\mathbf{R}}$ points radially outward from the central body, $\hat{\mathbf{T}}$ is tangent to the velocity vector in the orbital plane, and $\hat{\mathbf{N}}$ completes the right-handed coordinate system normal to the orbital plane (Battin, 1999) (Vallado, 2001). The instantaneous rates of change of the classical orbital elements under this perturbative acceleration are governed by Gauss's planetary equations (Battin, 1999):

$$\frac{da}{dt} = \frac{2a^2}{h}\left[a_R e \sin f + a_T \frac{p}{r}\right] \tag{B.1}$$

$$\frac{de}{dt} = \frac{a}{h}\left[a_R \sin f + a_T(\cos f + \cos E)\right] \tag{B.2}$$

$$\frac{di}{dt} = \frac{a\cos u}{h} a_N \tag{B.3}$$

$$\frac{d\Omega}{dt} = \frac{a \sin u}{h \sin i} a_N \tag{B.4}$$

where the orbital parameters are defined as:

- a = semi-major axis
- e = eccentricity
- i = inclination
- Ω = right ascension of ascending node
- $h = \sqrt{\mu a(1-e^2)}$ = specific angular momentum
- $p = a(1-e^2)$ = semi-latus rectum
- r = instantaneous radius
- $f = \theta$ = true anomaly

- E = eccentric anomaly
- $u = \omega + f$ = argument of latitude
- ω = argument of perigee
- μ = gravitational parameter of central body

Fundamental Orbital Relations

Several key geometric relationships from orbital mechanics are utilized in the derivation (Curtis, 2005):

$$\frac{p}{r} = 1 + e\cos f = 1 + e\cos\theta \tag{B.5}$$

$$\cos E = \frac{e + \cos f}{1 + e\cos f} \tag{B.6}$$

$$u = \omega + \theta \tag{B.7}$$

Optimization Methodology

For each orbital element, the instantaneous rate of change can be expressed as a linear combination of the acceleration components:

$$\frac{d(\text{œ})}{dt} = C_R a_R + C_T a_T + C_N a_N \tag{B.8}$$

where œ represents an orbital element and C_R, C_T, and C_N are coefficients derived from Gauss's planetary equations. To maximize this rate for a given thrust magnitude $|\mathbf{a}|$, the optimal thrust direction $\boldsymbol{\lambda}$ must be aligned with the coefficient vector $\mathbf{C} = [C_R, C_T, C_N]^T$ (Kechichian, 1997).

The normalized optimal thrust direction is therefore:

$$\boldsymbol{\lambda}_{\text{opt}} = \frac{\mathbf{C}}{|\mathbf{C}|} \tag{B.9}$$

Derivation of Optimal Thrust Directions

Semi-major Axis Optimization

From Equation (B.1) and applying the radius relation (B.5):

$$\frac{da}{dt} = \frac{2a^2}{h}\left[a_R e\sin\theta + a_T(1 + e\cos\theta)\right] \tag{B.10}$$

The coefficient vector is:

$$\mathbf{C}_a = \frac{2a^2}{h}[e\sin\theta, 1 + e\cos\theta, 0]^T \tag{B.11}$$

Therefore, the optimal thrust direction for maximizing semi-major axis rate is:

$$\boldsymbol{\lambda}_{O,a} = \begin{bmatrix} e\sin\theta \\ 1 + e\cos\theta \\ 0 \end{bmatrix} \tag{B.12}$$

Eccentricity Optimization

From Equation (B.2), the coefficient vector is:

$$\mathbf{C}_e = \frac{a}{h}[\sin\theta, \cos\theta + \cos E, 0]^T \tag{B.13}$$

The optimal thrust direction for maximizing eccentricity rate is:

$$\boldsymbol{\lambda}_{O,e} = \begin{bmatrix} \sin\theta \\ \cos\theta + \cos E \\ 0 \end{bmatrix} \tag{B.14}$$

Inclination Optimization

From Equation (B.3):

$$\frac{di}{dt} = \frac{a\cos(\omega + \theta)}{h} a_N \tag{B.15}$$

Since inclination changes are achieved exclusively through normal thrust, and the magnitude of the rate depends on $\cos(\omega + \theta)$, the optimal direction is:

$$\boldsymbol{\lambda}_{O,i} = \begin{bmatrix} 0 \\ 0 \\ \text{sgn}(\cos(\omega + \theta)) \end{bmatrix} \tag{B.16}$$

where $\text{sgn}(\cdot)$ denotes the sign function.

Right Ascension of Ascending Node Optimization

From Equation (B.4):

$$\frac{d\Omega}{dt} = \frac{a\sin(\omega + \theta)}{h\sin i} a_N \tag{B.17}$$

The optimal thrust direction for maximizing RAAN rate is:

$$\boldsymbol{\lambda}_{O,\Omega} = \begin{bmatrix} 0 \\ 0 \\ \text{sgn}(\sin(\omega + \theta)) \end{bmatrix} \tag{B.18}$$

C Project Plan

This chapter presents the work breakdown structure (WBS) and division of work by tasks and time in the form of a Gantt chart for the thesis project. The WBS, shown in Figure C.1, provides a hierarchical decomposition of the project into smaller sections, while the Gantt chart, shown in Figure C.2, displays the timeline and scheduling of tasks over the course of the thesis project.

C.1. Work Breakdown Structure

The WBS in Figure C.1 outlines the main phases and tasks involved in the thesis project. The first phase includes a 7-week literature review to gather existing research on the status quo of collision-avoidance maneuvers for sailcraft, in which a research gap is identified, and a research objective is formulated, with specific research questions to address the research gap. The research phase, spanning approximately 5 months, is used to develop all methodologies required to generate the results to suitably answer the research questions. Throughout the work, verification activities are performed to test the developed code and results.

Documentation and project management work is performed throughout the thesis to write the research proposal, thesis report, and prepare for the thesis defense. All code is stored in a GitHub repository to ensure version control and backup of all project files.

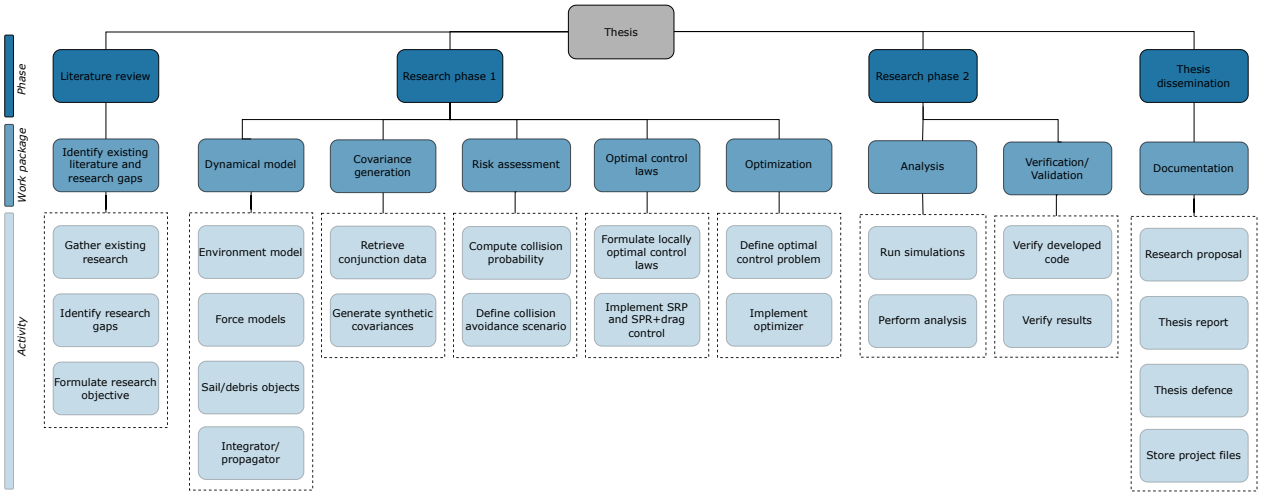

Figure C.1: Work Breakdown Structure, as of April 2025

C.2. Gantt Chart

Figure C.2 presents the Gantt chart used for planning the thesis project.

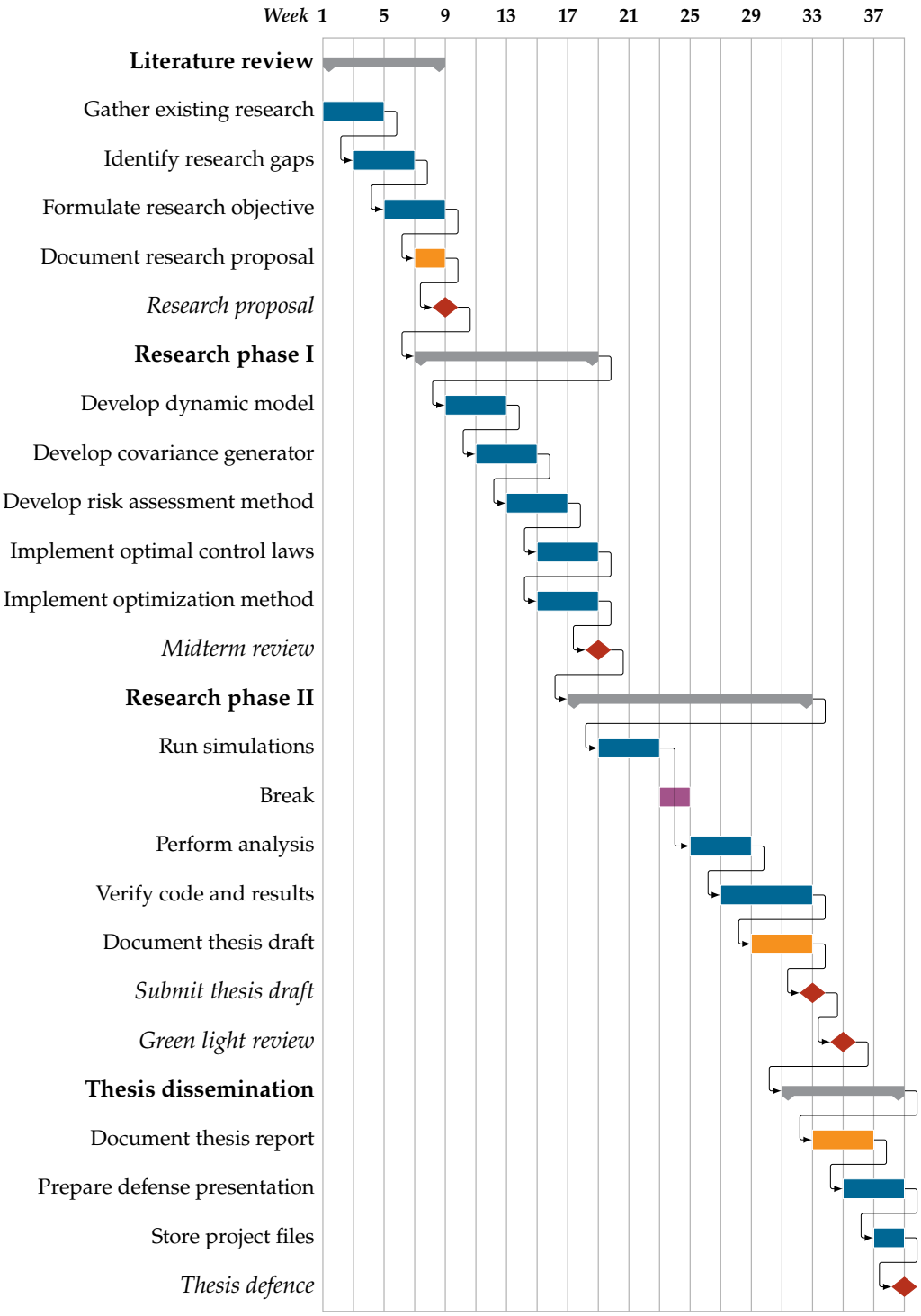

Figure C.2: Gantt chart showing the thesis schedule, as of April 2025.